NASA Technical Memorandum 78549

Supercritical Flow About a Thick Circular-Arc Airfoil

John B. McDevitt

January 1979

National Aeronautics and
Space Administration

NASA Technical Memorandum 78549

Supercritical Flow About a Thick Circular-Arc Airfoil

John B. McDevitt, Ames Research Center, Moffett Field, California

NASA
National Aeronautics and
Space Administration

Ames Research Center
Moffett Field, California 94035

SYMBOLS

a	speed of sound
C_p	pressure coefficient, $\frac{p-p_\infty}{q_\infty}$
c	airfoil chord
f	frequency
$\bar{f}$	reduced frequency, $2\pi f(c/2)$ divided by free-stream velocity
$L_{L.E.}$	length of splitter plate attached to airfoil leading edge
$L_{T.E.}$	length of splitter plate attached to airfoil trailing edge
M	Mach number
$\bar{M}_1$	local-flow Mach number ahead of shock in shock-fixed coordinates
P_o	total pressure
p	pressure
q	dynamic pressure, $\frac{1}{2}\rho u^2$
$Re_{c,\infty}$	Reynolds number based on airfoil chord and free-stream conditions
T	temperature
t	airfoil thickness or time
$\bar{t}$	fractional cyclic time
u_s	flow velocity along a streamline
x	streamwise coordinate measured from airfoil leading edge
x_{SH}	shock location
z	vertical coordinate measured from plane of airfoil
α	angle of attack
Δp	(instantaneous pressure) - (mean static pressure)
$\Delta( )$	incremental quantity
δ	flow-deflection angle
θ	shock-inclination angle

ρ density

Subscripts:

∞ free-stream conditions

peak peak value

1 conditions immediately ahead of shock

2 conditions immediately downstream of shock

SUPERCRITICAL FLOW ABOUT A THICK CIRCULAR-ARC AIRFOIL

John B. McDevitt

Ames Research Center

SUMMARY

The supercritical flow about a biconvex circular-arc airfoil is being thoroughly documented at Ames Research Center in order to provide experimental test cases suitable for guiding and evaluating current and future computer codes. This paper is a continuation of an earlier study and extends the original test program to include effects of angle of attack, effects of leading and trailing-edge splitter plates, additional unsteady pressure fluctuation (buffeting) measurements and flow-field shadowgraphs, and application of an oil-film technique to display separated-wake streamlines. Detailed comparisons of computed and measured pressure distributions for steady and unsteady flows, using a recent computer code representative of current methodology, are included. It was found that the numerical solutions are often fundamentally incorrect in that only "strong" (shock-polar terminology) shocks are captured, whereas experimentally, both strong and weak shock waves appear.

INTRODUCTION

Rapid advances in computer technology and numerical methods lend credence to the belief that the computer might, by complementing the wind tunnel, achieve significant time and cost reductions in the design of new aircraft (ref. 1). Appropriate methods, however, must be devised for modeling the turbulence of compressible flows. But progress in this area is extremely difficult and it is important that parallel experimental studies be undertaken to provide necessary guidance for the development and verification of newly proposed turbulence models and computer codes.

One phenomenon of particular interest and importance in fluid dynamics is the separation of boundary layers by shock waves. An experimental and numerical study of this phenomenon, as related to airfoils at supercritical speeds, is described in references 2 through 4; the present study is a continuation of this earlier work. The basic approach used involved the construction of a new facility (the Ames "High Reynolds Number Channel"), with emphasis on achieving as wide a range in test Reynolds numbers as possible. This approach included a design concept of interchangeable test sections that become an integral part of each experiment. For the first experiment, a two-dimensional, 18%-thick biconvex circular-arc airfoil was chosen and the test-channel walls were contoured to minimize wall-interference effects (see ref. 2 for details). The test program successfully achieved essentially two-dimensional flows over a wide range in test Reynolds numbers and three basic flows of interest for

airfoils at supercritical speeds were documented: (1) steady supercritical flow with boundary-layer separation at the trailing-edge region, (2) steady flow with shock-induced separation, and (3) strong buffeting involving periodic flowfield oscillations.

These early results, which appear to be ideally suited for guiding and evaluating the development of turbulence models and computer codes, prompted the additional studies of references 5 through 8, and gave rise to the new results presented here. An important modification to Deiwert's original airfoil code was made by Levy (ref. 6) who extended the code to include test-section solid-wall boundaries, thus facilitating comparisons of computation with experiment. Measurements of skin friction and flow-field velocities are presented in references 7 and 8.

The present paper extends the experimental investigations of reference 2 to include effects of angle of attack, effects of leading and trailing-edge splitter plates, additional unsteady pressure-fluctuation (buffeting) measurements and flow-field shadowgraphs, and application of an oil-film technique to display separated-wake streamlines. Also included here are detailed comparisons of numerical solutions with experiment which will show that two fundamental problems with numerical methods must be resolved before critical evaluations of turbulence models can proceed.

EXPERIMENT

The basic considerations underlying the choice of airfoil and nominal test Mach number are illustrated in figure 1 and the test section arrangement is shown in figure 2. In reference 2 a detailed discussion of the basic considerations involved in defining this experiment is presented. The airfoil model described in reference 2 was also used for the present tests except that additional fast-response pressure transducers were installed for better resolution of unsteady-flow phenomena. The upper and lower channel wall contours, listed in table 1 of reference 2, were also retained for the present tests. These contours approximate the airfoil streamlines in free air at a nominal Mach numnumber of 0.775. A brief summary of the steady-flow characteristics of the airfoil at slightly supercritical speeds will be presented before introducing new test results and analyses.

Steady Flows, $\alpha = 0°$

The shock-buffeting domains for the airfoil at $\alpha = 0°$, in both accelerating and decelerating flows, are shown in figure 3. At speeds below the unsteady domain, the boundary layer separates near the trailing edge; typical airfoil pressure distributions are shown in figure 4. A spark-illuminated shadowgraph (fig. 5), taken at a moderately high Reynolds number (boundary-layer transition well forward of the midchord), shows multiple-compression wavelets that, although crowded together, do not separate the boundary layer.

At speeds above the unsteady domains, shock-induced separation of the boundary layer prevails (figs. 6 and 7). The shadowgraph was taken for a

well-established turbulent boundary layer; a single, strong shock wave is clearly defined which interacts with the boundary layer to cause a large separation bubble with reattachment downstream of the airfoil.

Wake Streamlines, Shock-Induced Separation

An oil-film technique was used with thin vertical fences to display streamline patterns downstream of the airfoil trailing edge. Sample test results are shown in figure 8. The oil (a mixture of vacuum pump oil, titanium oxide, and a small amount of oleic acid) appears white against the black finish on the fences. The most effective display of streamlines occurred when the oil was applied in thin vertical lines, which served as reservoirs to continuously feed random filaments during the test run. It should be emphasized that this particular application is not meaningful ahead of the airfoil trailing edge because of flow distortion in the corner between fence and airfoil, but downstream of the trailing edge the results are useful (see fig. 9). From these observations, and by making use of the LDV measurements of reference 8, the mean-wake-streamline pattern for "steady" flow with shock-induced separation is approximately as that shown in figure 10. The wake is highly turbulent but the mean vertical height is approximately the same as the airfoil thickness and the wake closes downstream near $x/c = 1.26$.

Unsteady Flow, $\alpha = 0°$

The Reynolds-number, Mach-number domains where unsteady, periodic flows occur for the subject airfoil was shown previously in figure 3. This unsteady phenomenon was discussed in considerable detail in reference 2. Additional information will be provided here, primarily for a chord Reynolds number of 11×10^6, so as to document more fully a specific unsteady-flow test case suitable for evaluating new airfoil codes.

Typical instantaneous airfoil surface-pressure measurements, showing deviations from mean values, are presented in figures 11 through 13. The speed-control wedge shown in figure 2 was used to change the test Mach number slowly, at the approximate rate $dM_\infty/dt = 0.001$. (This rate was about the largest that could be used without introducing noticeable errors in mean pressure measurements due to system lag.) Note that the onset of buffeting is sudden, but once the unsteady flow has started, the motion persists at considerably lower Mach numbers when the free-stream Mach number is decreased. With increasing Mach number, the phenomenon weakens and eventually steady flow again prevails.

A close look at the instantaneous pressure measurements and at high-speed shadowgraph movies of the flow fields indicates that two distinct types of periodic flows occur for this airfoil at zero angle of attack. We will use the labels given by Tijdeman (refs. 9 and 10) for various shock motions: the shock oscillates on the airfoil (type A); the shock disappears during part of the cycle (type B); and the shock propagates upstream and leaves the airfoil (type C). In the present experiment, type C motion prevails throughout most of the domains shown in figure 3, the exception being near the right-hand (i.e., high speed) boundaries where the buffeting is weak and is approaching

the steady state with shock-induced separation of the boundary layer. Also, in this case, type C motion involves alternate trailing-edge and shock-induced separations of the boundary layer with the airfoil upper and lower flow fields 180° out of phase.

Typical shadowgraphs are presented in figure 14; this type of unsteady flow is characterized by the cyclic formation, first of a multiple-shock structure near the airfoil trailing edge, then emergence of a single strong wave, which progresses upstream and disappears forward of the airfoil. A dimensionless time parameter, $\bar{t}$, is used to indicate the fractional cyclic time where the start of each new cycle is coincident with the passage of the shock over the midchord of the airfoil. The chordwise location of the primary shock-wave interaction with the boundary layer for the case depicted in figure 14 is presented in the left-hand side of figure 15.

The second type of unsteady flow, type A, occurs near the high-speed edge of the unsteady flow domain and involves only shock-induced boundary-layer separation. The shock wave does not disappear and reappear in cyclic fashion as for the first type but merely moves back and forth on the airfoil as illustrated by the example presented in the right-hand side of figure 15.

As mentioned in reference 2, the frequency of the unsteady flow was approximately 188 ± 3 Hz throughout the test program. The slight frequency variation with Mach number for $Re_{c,\infty} = 11 \times 10^6$ is shown in figure 16. At this Reynolds number the unsteady phenomenon may be summarized as follows: at Mach numbers below $M_\infty = 0.733$ the flow is steady with trailing-edge separation; and above $M_\infty = 0.778$ the flow is again steady but with shock-induced boundary-layer separation fixed near $x/c \approx 0.65$. Between $M_\infty = 0.733$ and 0.776 unsteady flow of type C occurs with the buffeting intensity diminishing with increasing Mach number. Near $M_\infty = 0.776$, the flow is erratic and the transition to type A begins, but the chordwise excursions of type-A motion diminish rapidly with increasing Mach number and soon end at about $M_\infty \approx 0.778$.

We will now consider in detail the instantaneous pressure fluctuations for a test case involving strong, type-C buffeting at $Re_{c,\infty} = 11 \times 10^6$ and a free-stream Mach number of 0.76. The cyclic variations in shock location and shock motion are presented in figure 17; measurements (from shadowgraph movies) at the shear-layer edge of shock inclination angle, θ, and of shock-induced flow deflection angle, δ, are presented in figure 18. Both instantaneous and mean chordwise pressure variations are shown in figure 19. Pressure-fluctuation measurements (referenced to mean values) were made at stations $x/c = 0.25$, 0.50, and 0.78 and interpolation of the data to obtain values at intervening stations was made with the help of information gleaned from shadowgraph movies (see figs. 17 and 18). The presentation in this figure, incidentally, is arranged so that upper- and lower-surface measurements can be compared directly, since equivalent flow fields differ by $\Delta\bar{t} = 0.5$. An alternative presentation for fixed chordwise stations is made in figure 20. It is interesting to note (fig. 19) that, for stations ahead of the midchord (airfoil crest), the maximum instantaneous pressure occurs at passage of the shock wave, followed by a decrease in pressure until the next cyclic shock arrives. However, aft of the midchord (except very near the trailing edge) flow compression continues after passage of the wave and the maximum pressure

recovery is not reached until the end of the cycle. The local flow Mach number, M_1, at the base of the shock wave, and the relative Mach number (shock fixed coordinates),

$$\overline{M}_1 = M_1 - \frac{V_{shock}}{a_1}$$

are presented in figure 21.

The information presented in figure 14 and in figures 17 through 21 constitutes an unsteady-flow test case for evaluating numerical flow simulation codes. A comparison of these experimental results with a current airfoil computational method will be made later in this report.

Tests at Angle of Attack

A limited, and largely exploratory, study of the effects of angle of attack was made by rotation of the airfoil about the midchord. The channel-wall contours (fig. 2) were not changed and the angles of attack were limited to ±4°. The tests were conducted by slowly varying ($dM/dt \approx 0.001$) the Mach number from 0.750 to 0.785 and then back again to 0.750 (by using the speed-control wedge shown in fig. 2). The test Reynolds number was held constant at 11×10^6. From continuous recordings of instantaneous pressure measurements and from high-speed shadowgraph movies, the domains for unsteady flow were obtained and are shown in figure 22. Angle of attack serves to accelerate the leeward flow, enhancing the onset of shock-induced separation, but the windward flow is retarded making it more difficult to experience shock-induced separation. The result is a narrowing of the gap between left-hand boundaries of the unsteady flow domains (less hysteresis) as shown in figure 22.

Typical pressure fluctuations at midchord, upper surface are presented in figures 23 and 24 (separate test runs were made for positive and negative angles of attack). The magnitude of the pressure fluctuations on the windward side (negative α) decrease with angle of attack. Because an angle of attack of 4° is relatively small for such a thick airfoil it is probable that a considerably larger angle of attack would be required for communication between upper and lower flow fields to weaken to where shock oscillations of type C could no longer be sustained. The measured frequencies of the unsteady flow are shown in figure 25.

Measurements of mean pressure distributions are presented in figure 26 for steady flow with trailing-edge separation; in figures 27 and 28 for unsteady flow; and in figure 29 for steady flow with shock-induced separation. The peak Mach number at the onset of unsteady flow remained approximately equal to 1.25 as the angle of attack increased but the ability to sustain oscillations at lower Mach numbers, once the phenomenon started, diminished with angle of attack.

A composite shadowgraph (photos taken at $\alpha = 3°$ and $-3°$) is presented in figure 30, together with the variation of shock-wave position at the shear layer edge with angle of attack.

Splitter Plates

The cyclic unsteady flow (type C) for the subject airfoil involves alternate trailing-edge and shock-induced separations of the boundary layer, with upper and lower flow fields 180° out of phase; it depends on communication between upper and lower flow fields. An experimental study of the importance of flow-field communication was made by attaching thin "splitter" plates (0.02 chords thick) mounted in the plane of the wing, extending upstream and/or downstream of the airfoil.

The first tests were made with plates of length c/2 and typical measurements of pressure fluctuations ($p_{instantaneous} - p_{mean}$) at midchord are presented in figures 31 through 33. Mounting the plate ahead of the wing leading edge had little effect on the unsteady phenomenon, including flow-oscillation frequency ($f \approx 190$ Hz), except that the onset of unsteady flow was delayed to a slightly higher free-stream Mach number. As an example, for $Re_{c,\infty} = 8 \times 10^6$ and $dM_\infty/dt \approx 0.001$, the onset occurs at about $M_\infty = 0.760$ for the wing alone but is delayed to about $M_\infty = 0.765$ when the splitter plate is mounted ahead of the wing. However, once the periodic flow oscillation starts, the motion persists at considerably lower Mach numbers, as in the wing-alone case.

Attaching the plate downstream (fig. 32) virtually eliminated the unsteady phenomenon; the only noticeable periodic pressure fluctuations were detected by the most rearward sensor and this type-A motion occurred only in a very narrow Mach number range - from $M_\infty = 0.771$ to 0.773. When both forward and rearward plates were attached, continuous monitoring of the pressure sensors in the test range from $M_\infty = 0.745$ to 0.785 failed to uncover an unsteady phenomenon (sample data records are shown in fig. 33).

Since a relatively long plate in the forward location was found to have only a small effect on the unsteady flow, it was felt that a continuation of the study should be confined to downstream plate positions. Typical results with short trailing-edge plates are presented in figures 34 and 35 and the unsteady-flow domains for $Re_{c,\infty} = 8 \times 10^6$ are shown in figure 36. Type-C motion, which is easily detected by the pressure signature at $x/c = 0.5$ (compare figs. 35 and 36), occurs only for very short plates. The effects of plate length on pressure-fluctuation amplitude and frequency of motion are summarized in figure 37. Also included in this figure is an indication of the downstream extent of the separation bubble for steady shock-induced separation at a slightly higher Mach number (from fig. 10). The wake closes about a quarter chord downstream of the airfoil trailing edge and a splitter plate of this length is very effective in suppressing communication across the wake, although a high-frequency shock instability of type A persists at low amplitude.

The effects of various splitter plates on mean pressure measurements are shown in figure 38. Detailed measurements at the most rearward station (C_p at $x/c = 0.975$) for both increasing and decreasing speeds are presented in figure 39. Note that the large hysteresis effect in the wing-alone aft pressure measurements is greatly reduced by even the smallest splitter plate tested ($L_{T.E.} = c/8$).

Typical spark-illuminated shadowgraphs, taken with a trailing-edge splitter plate of length $c/2$ attached, are presented in figure 40. With the plate, unsteady flow is avoided, except in the very narrow Mach-number range of $M_\infty = 0.771$ to 0.773 (see fig. 36). At the lower supercritical Mach numbers, multiple wavelets appear and the boundary layer is believed to separate only near the trailing edge. As the Mach number increases, the waves coalesce, first near the body, and eventually an oblique shock emerges and separates the flow.

COMPARISONS OF NUMERICAL SOLUTIONS WITH EXPERIMENT

Three supercritical flow fields will be examined in detail: (1) the supersonic zone terminated by diffuse pressure recovery with attached boundary layer; (2) shock-induced separation of the boundary layer; and (3) unsteady asymmetric flow involving periodic switching between trailing-edge and shock-induced separations. Experimental measurements will be compared with numerical solutions from an airfoil computational method developed by Deiwert (ref. 3), which includes MacCormack's modifications (ref. 11) to improve efficiency, and Levy's modification (ref. 6) to include test-section solid-wall boundaries. Basically the method solves the time-dependent, two-dimensional, Reynolds-averaged Navier-Stokes equations with simple algebraic eddy viscosity models (see refs. 2 through 6 and 11 for further details).

Trailing-Edge Separation

In the Mach-number range from critical (first appearance of sonic flow on the airfoil) to the onset of buffeting, the airfoil supersonic zones, with adjacent turbulent boundary layers, terminate by diffuse pressure recovery and the boundary layer separation is delayed to near the trailing edge. When a trailing-edge splitter plate is used, the unsteady flow is suppressed and the shadowgraphs presented in figure 40, all for steady flow, show the transition from multiple shocks to a single oblique shock as the Mach number increases.

A comparison between experimental and computed pressure distributions for the case where multiple wavelets appear, but do not separate the boundary layer, is presented in figure 41. The comparison is made for the wing with trailing-edge plate included because Deiwert's code indicated unsteady flow for the wing alone at this Mach number (experimentally, either steady or unsteady flow can occur; see fig. 3). The measurements indicate a steep pressure recovery between about $x/c = 0.6$ and 0.68 where the wavelets are most concentrated and the pressure recovery is matched remarkably well by computation. Although the computational grid is closely spaced vertically near the airfoil surface to resolve the boundary layer, the horizontal spacing is relatively large ($\Delta x/c = 0.02$ near the "captured shock" and larger elsewhere) - this tends to smear the pressure recovery but there was good agreement between experiment and computation except very near the trailing edge where the

boundary layer had separated. The poor agreement near the trailing edge suggests inadequate turbulence modeling.

The complex flow phenomenon indicated by the shadowgraph rules out "shock-fitting" techniques. The "shock-capturing" technique (included in the Deiwert code) probably is sensitive to grid geometry in many cases and a definitive study of this aspect would be particularly informative using the complex flows displayed in the photographs of figure 40 as examples.

The computed Mach contours in the flow field are shown in figure 42. The contours stand more or less normal to the surface near the downstream edge of the supersonic zone ($x/c \approx 0.65$) but the rapid pressure recovery is not representative of a single normal shock. Specifically, the maximum flow Mach number, both the computational number and the experimental number, is about 1.26 and the pressure jumps from about $C_p = -1.1$ to -0.4; the pressure jump for normal shock recovery, however, would be from -1.1 to -0.2.

Shock-Induced Separation

A comparison of measured and computed pressure distributions for steady flow at $M_\infty = 0.785$ with shock-induced separation is presented in figure 43. The numerical method accurately predicts the pressure distribution over the forward portion of the airfoil but is grossly inaccurate in predicting shock location and strength. The fundamental differences between the numerical and experimental shock waves will be discussed next.

Computed Mach contours at $M_\infty = 0.783$ are shown in figure 44(c) (reproduced from ref. 6). In figure 44(c), "chords traveled" is a measure of elapsed computational time after convergence of solutions and corresponds to chord lengths traveled by the mean flow during one cycle of the oscillatory flow - figure 44(b) - to be discussed later. The numerical solutions at $M_\infty = 0.783$ behaved erratically, but a periodic unsteady flow was not indicated, and in the following analysis mean values of computed solutions at this Mach number will be used. (The reason for this erratic behavior in the solutions at this Mach number will be discussed subsequently.) In this flow example an oblique, clearly defined shock wave appears and the pressure recovery near the foot of the wave is compatible, both experimentally and computationally, with theoretical oblique shock relationships, as shown in figure 45. In figure 45, computed and measured values of shock wave angle, pressure jump, and local flow Mach number ahead of the shock have been superimposed on the theoretical inviscid relationships. The experimental measurements locate a point in the "weak" shock-polar domain and the flow downstream of the wave is supersonic. The computed values were taken to be the mean values of the somewhat erratic solutions shown in figure 44(c) and define a location in the "strong" shock-polar domain for which the downstream flow is subsonic.

The more conventional ways to display shock-polar relationships involve the flow deflection angle, as shown in figures 46 and 47. The points nearest the airfoil, "A" (experiment) and "E" (computation), were transcribed from the previous figure and imply approximately the same flow deflection angle in both

cases ($\delta \approx 7°$). Sketches of the computed and experimental flow fields, drawn to scale, are included in figure 46. In the computation, the shock wave is always of the "strong type," supersonic to subsonic, and numerical irregularities in the subsonic downstream region can directly affect the shock wave. This is the probable explanation for the quasi-steady behavior mentioned previously of the computations shown in figure 44(c). Experimentally, the shock is "strong" only in the outer region, (C) to (D), while inboard the shock is "weak" with the so-called "supersonic tongue" attached from (A) to (B). This "tongue" acts as a buffer region between the turbulent wake and shock wave which explains why the shock position appears to be very stable in the high-speed shadowgraph movies at this test condition.

Shock-polar variations between downstream Mach number and flow-deflection angle, for various values of upstream Mach number, are shown in figure 47 (the flow-field points (A) through (E) correspond to those shown in the previous figure). Measurements by a laser Doppler velocimeter technique (ref. 8) of local Mach number at the shear-layer edge are presented in figure 48. These measurements indicate that the "supersonic tongue" extends nearly to the airfoil trailing edge.

The poor agreement between experiment and computation shown in figure 43 is a consequence of the numerical method choosing a "strong" (shock-polar terminology) shock wave whereas the experimental wave is primarily "weak." It is well known from shock-polar relationships that two different shock waves and flow patterns are theoretically possible for given δ and M_1. However, it is believed that only the weaker shock wave (larger M_2 and smaller θ) will occur experimentally (see discussions of flows past wedges in ref. 12, p. 12, and ref. 13, p. 317). It is doubtful that computational grid size or orientation could account for the fact that the numerical method captures the shock on the wrong side of the shock polar.

Unsteady Flow

Comparisons of measured and computed pressure distributions at a Mach number where strong buffeting occurs are presented in figure 49. (See figs. 17 through 21 for additional experimental results at this Mach number.) Deiwert's numerical method (ref. 3) has been shown by Levy (ref. 6) to be capable of qualitatively predicting the essential features of this unsteady flow but significant differences between experiment and computation are evident, particularly with regard to the aft surface pressure recovery. The frequency of pressure oscillations was also noticeably different — in the experiment the reduced frequency was $\bar{f} = 0.49$ ($f \approx 190$) but numerically the reduced frequency was about 20% less ($f \approx 150$). In both the experiment and in the numerical solutions a clearly defined shock wave emerges after an elapsed cyclic fractional time of about $\bar{t} = 0.25$. Detailed comparisons of shock positions at the shear-layer edge and of corresponding effective upstream Mach numbers and shock pressure jumps are presented in figures 50 and 51. In both the experiment and computations the cyclic-shock formation occurs near $x/c = 0.85$, but in the experiment the shock wave immediately after formation moves upstream rapidly, whereas the computed shock wave remains stationary near $x/c = 0.85$

for about 20% of the cycle. This difference in shock-position behavior probably is related to the fact (to be shown subsequently) that the shock wave near the shear-layer edge experimentally is "weak" (shock-polar terminology), with trailing flow supersonic, whereas the computed shock is "strong," with trailing flow subsonic. Consequently, the stream momentum external to the separated region is much higher experimentally; this supports a stronger cyclic-induced upwash/downwash phenomenon and the experimental flow oscillation does not hesitate as in the numerical solutions.

Experimental measurements at or near the airfoil surface of $(p_2 - p_1)/q_1$, M_1, and θ at the shear-layer edge are superimposed on shock polar diagrams in figure 52 and these three measurements are, within the accuracy of the tests and for the cyclic times considered, mutually compatible with pressure recovery through oblique shock waves. The results are summarized in figure 53 and compared with numerical solutions. In the computations, only "strong shocks" appear, but in the experiment the first cyclic appearance of a clearly defined wave is in the "weak-shock" domain of the shock polar. With increasing cyclic time, the strong-shock domain is entered as the wave approaches the airfoil crest and eventually disappears ahead of the airfoil as a weakening sound wave. The failure of the numerical method to capture anything but strong shocks is the probable explanation for the inaccurate pressure recoveries shown in figure 52.

The unsteady flow analyzed here has not introduced new computational problems. The failure of the numerical code in the unsteady case is related to the failure discussed previously for steady flow with shock-induced separation in that only "strong" shocks are found in the computations. If a suitable computing code and adequate turbulence modeling are found for the static case, the dynamic case should, in principle, follow, as time-accurate solutions are now routinely obtained with advanced computers.

CONCLUDING REMARKS

The present study of the supercritical flow about a thick circular-arc airfoil is a continuation of the investigation reported on in reference 2. The primary purpose of this undertaking is to provide well-documented experimental test cases suitable for guiding the development of and evaluating airfoil numerical flow-simulation codes. This paper extends the original test program to include effects of angle of attack, effects of leading and trailing-edge splitter plates, additional unsteady-flow pressure measurements and flow-field shadowgraphs, and application of an oil-film technique to display separated-wake streamlines.

Included in this paper are detailed comparisons of computed and measured airfoil surface pressures for three specific test cases, all involving supercritical flows. The numerical method used in the comparisons represents current methodology and solves the Reynolds-averaged, two-dimensional, compressible Navier-Stokes equations. The first test case studied involved steady flow with diffuse pressure recovery terminating the supersonic zone and with

boundary layer separation delayed to near the trailing edge. With the exception of the trailing-edge region, the agreement between computed and measured pressures was good. The poor agreement for the separated trailing-edge region indicates inadequate turbulence modeling.

The next test case analyzed involved shock-induced separation of the boundary layer. Here, the numerical simulation was found to be fundamentally incorrect in that the method captured a "strong shock" (shock-polar terminology) whereas the experiment showed a "weak shock," with trailing "supersonic tongue" near the body, and the shock wave is "strong" only near the outer extent of the supersonic zone. Consequently, the computed aft surface pressure recovery was much larger than that measured.

The third case involved strong buffeting with separation alternately switching from trailing-edge separation to shock-induced separation. Again, it was found that the numerical method captures only strong shocks and that the experiment displays strong and weak waves in the cyclic-flow oscillation.

The detailed comparisons of computed and measured results point out the need for two fundamental studies in addition to the general problem of finding proper turbulence models: first, the influence of computational mesh geometry on the numerical solutions must be determined. Second, the preference of numerical methods for strong shocks, in contrast to the appearance experimentally of both weak and strong shocks, must be corrected. Unsteady flow phenomena, such as the buffeting included in the present study, do not introduce additional computational problems. If the numerical method and the turbulence modeling are adequate in the static case, then time-dependent solutions would easily follow.

REFERENCES

1. Chapman, Dean R.; Mark, Hans; and Pirtle, Melvin W.: Computers vs Wind Tunnels for Aerodynamic Flow Simulation. Astronaut. & Aeronaut., vol. 13, no. 4, April 1975, pp. 22-30.

2. McDevitt, John B.; Levy, Lionel L., Jr.; and Deiwert, George S.: Transonic Flow About a Thick Circular-Arc Airfoil. AIAA J., vol. 14, no. 5, May 1976, pp. 606-613.

3. Deiwert, George S.: Numerical Simulation of High Reynolds Number Transonic Flows. AIAA J., vol. 13, no. 10, Oct. 1975, pp. 1354-1359.

4. Deiwert, George S.: Computation of Separated Transonic Turbulent Flows. AIAA J., vol. 14, no. 6, June 1976, pp. 735-740.

5. Deiwert, George S.: High Reynolds Number Transonic Flow Simulation. Lecture Notes in Physics, vol. 35, Springer-Verlag, Berlin, Germany, 1975, p. 132.

6. Levy, Lionel L., Jr.: Experimental and Computational Steady and Unsteady Transonic Flows About a Thick Airfoil. AIAA J., vol. 16, no. 6, June 1978, pp. 564-572.

7. Rubesin, M. W.; Okuno, A. F.; Levy, L. L., Jr.; McDevitt, J. B.; and Seegmiller, H. L.: An Experimental and Computational Investigation of the Flow Field About a Transonic Airfoil in Supercritical Flow with Turbulent Boundary-Layer Separation. NASA TM X-62,465, July 1976.

8. Seegmiller, H. L.; Marvin, J. G.; and Levy, L. L., Jr.: Steady and Unsteady Transonic Flow. AIAA J., vol. 16, no. 12, Dec. 1978, pp. 1260-1270.

9. Tijdeman, H.: On the Motion of Shock Waves on an Airfoil with Oscillation Flap in Two-Dimensional Transonic Flow. NLR TR 75038U, 1975.

10. Tijdeman, H.: On the Motion of Shock Waves on an Airfoil with Oscillating Flap. IUTAM Symposium Transsonicum II, K. Oswatitsch and D. Rues, eds., Göttingen, Germany, 1975, pp. 49-56.

11. MacCormack, R. W.: An Efficient Numerical Method for Solving the Time Dependent Compressible Navier-Stokes Equations at High Reynolds Number. NASA TM X-73,129, July 1976.

12. Ames Research Staff: Equations, Tables, and Charts for Compressible Flow. NACA TR-1135, 1953.

13. Courant, R.; and Friedrichs, K. O.: Supersonic Flow and Shock Waves. Interscience Publishers, Inc., New York, 1948.

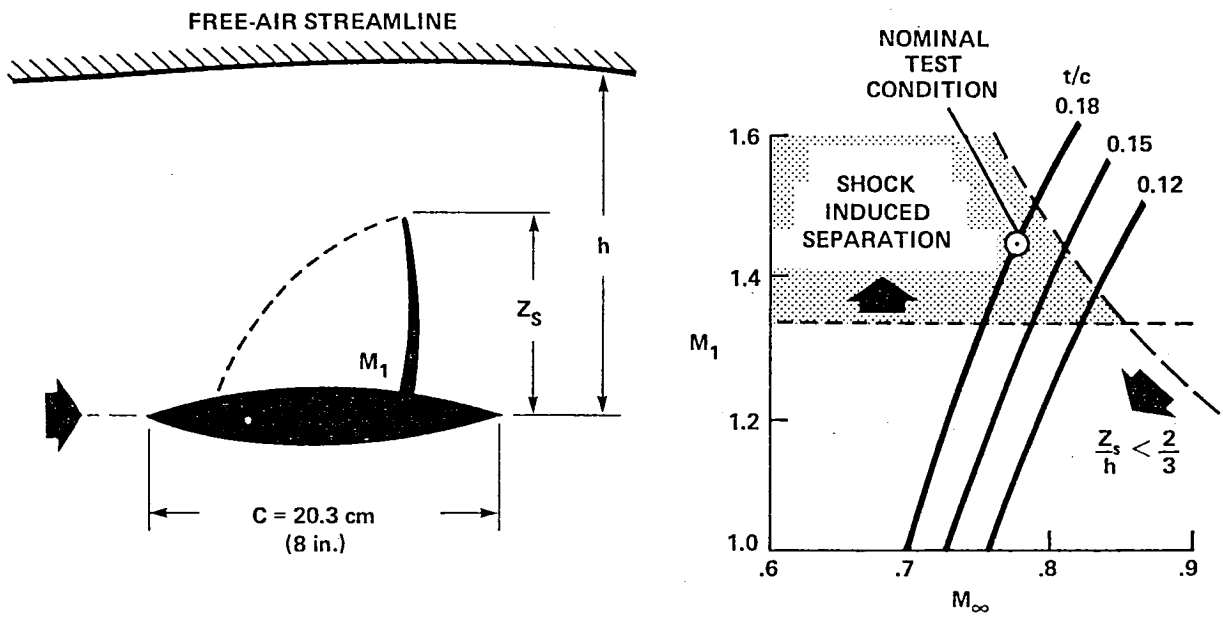

Figure 1.- Biconvex circular-arc airfoil experiment.

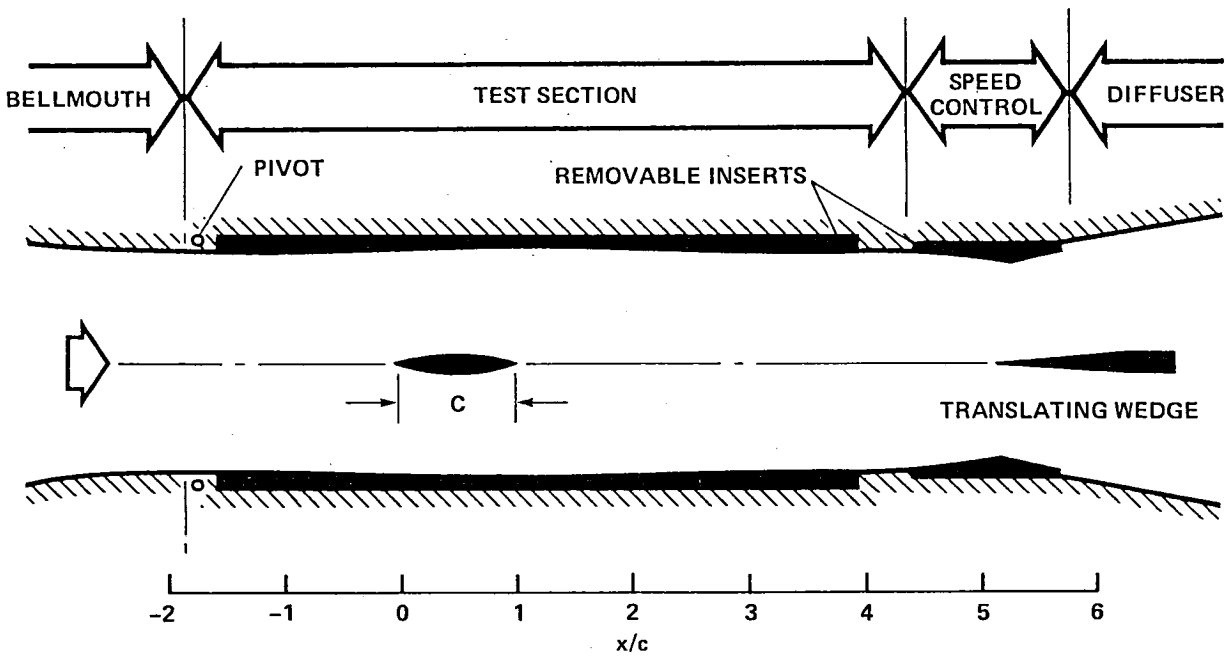

Figure 2.- Test-section schematic.

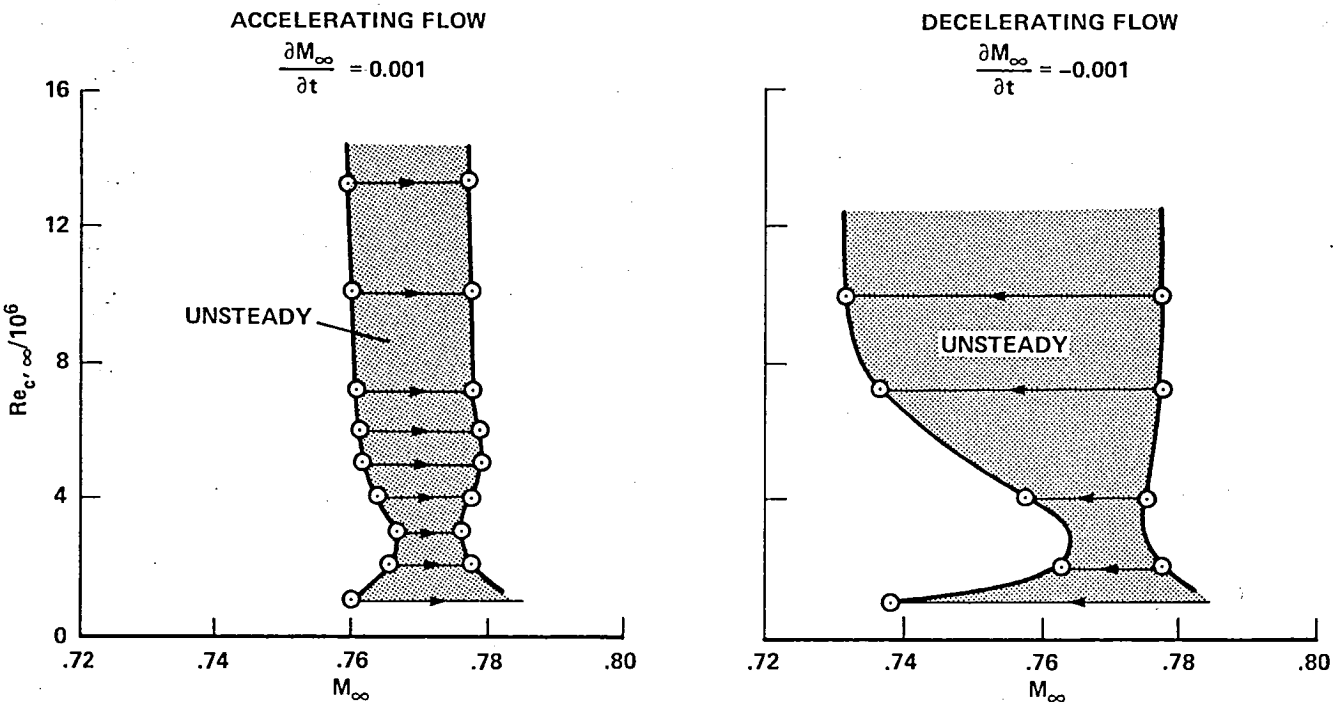

Figure 3.- Unsteady flow domains (from ref. 2).

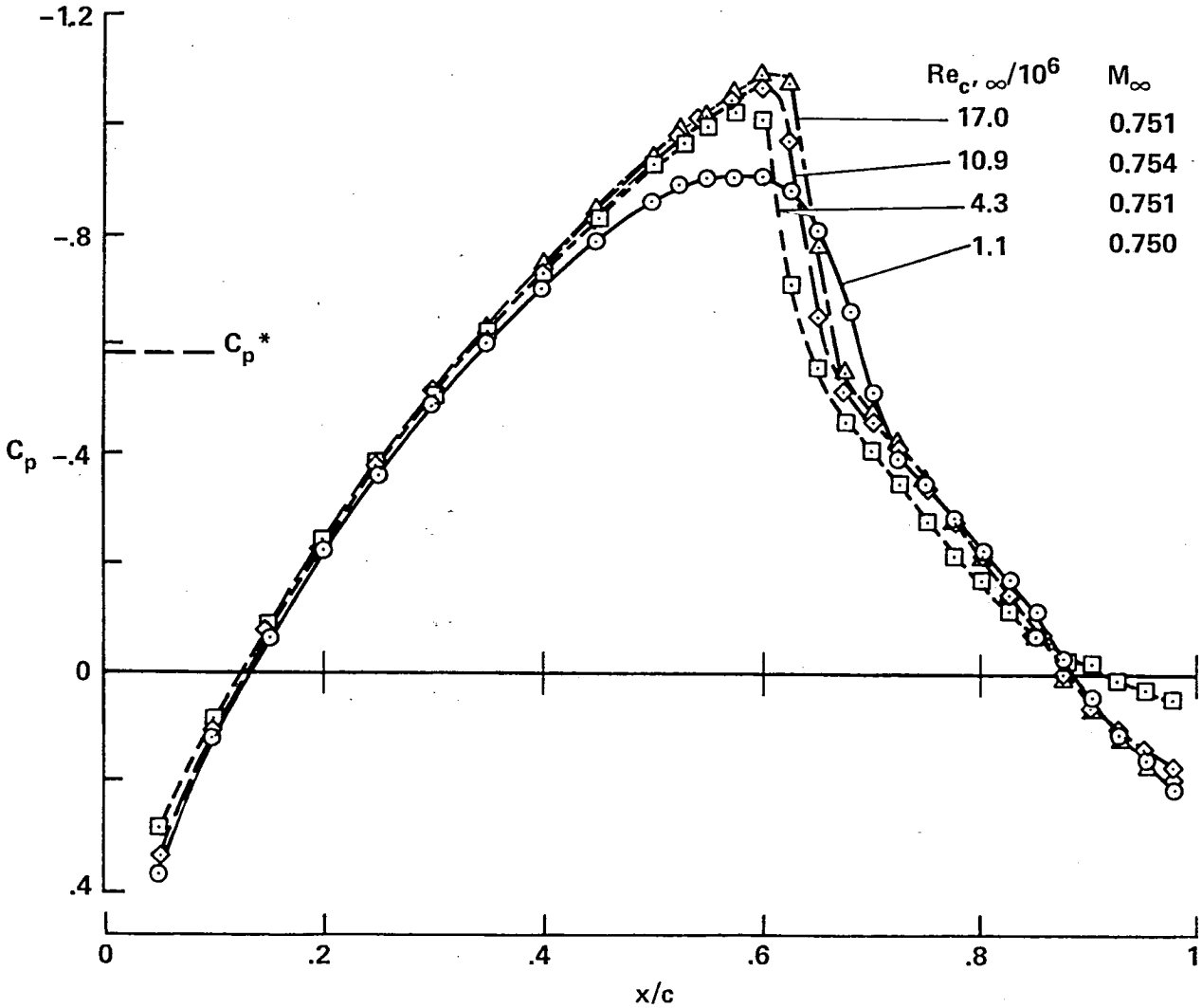

Figure 4.- Pressure distributions at speeds below the buffeting region (from ref. 2).

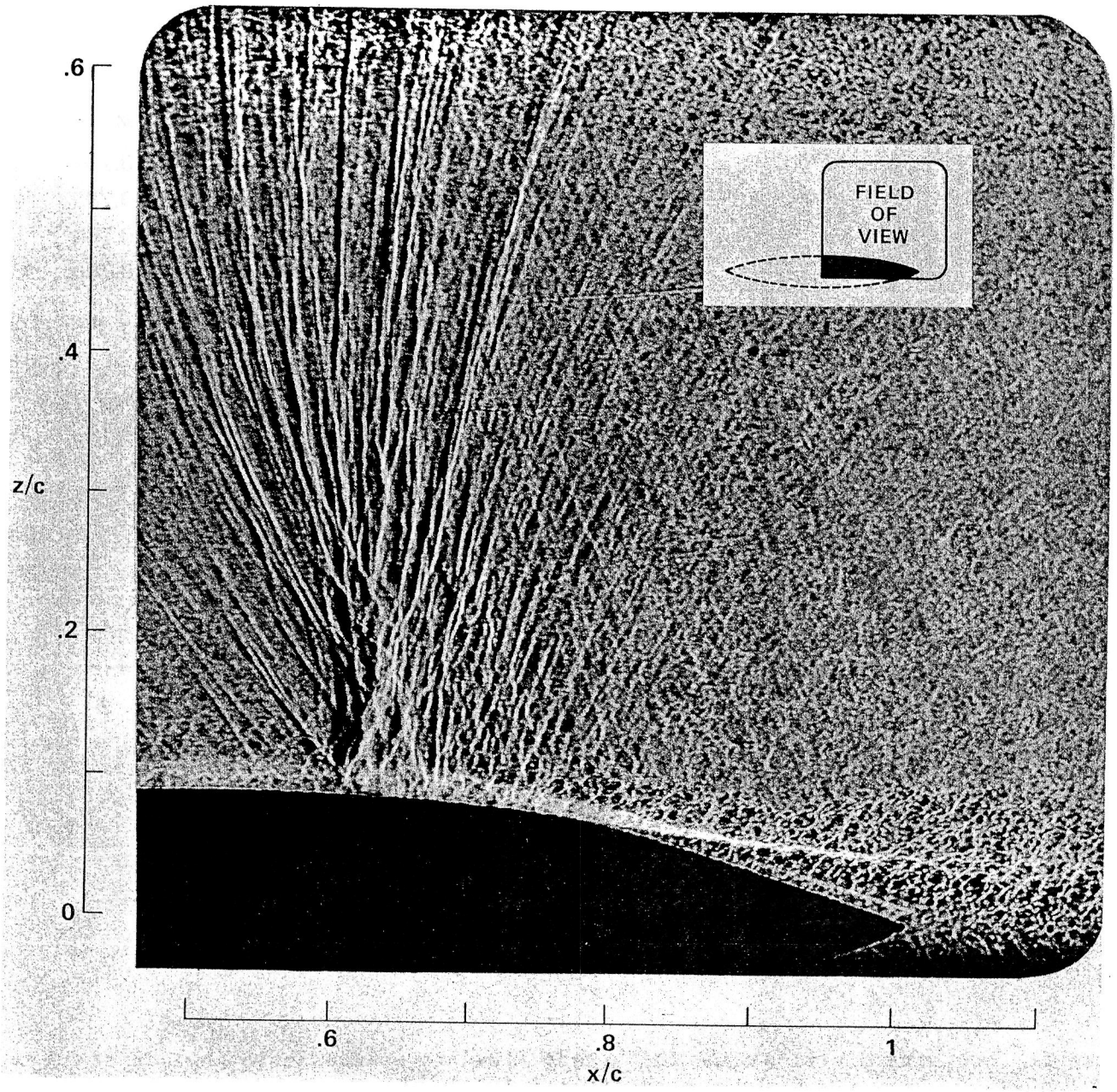

Figure 5.- Flow-field shadowgraph, $M_\infty = 0.76$, $Re_{c,\infty} = 11 \times 10^6$.

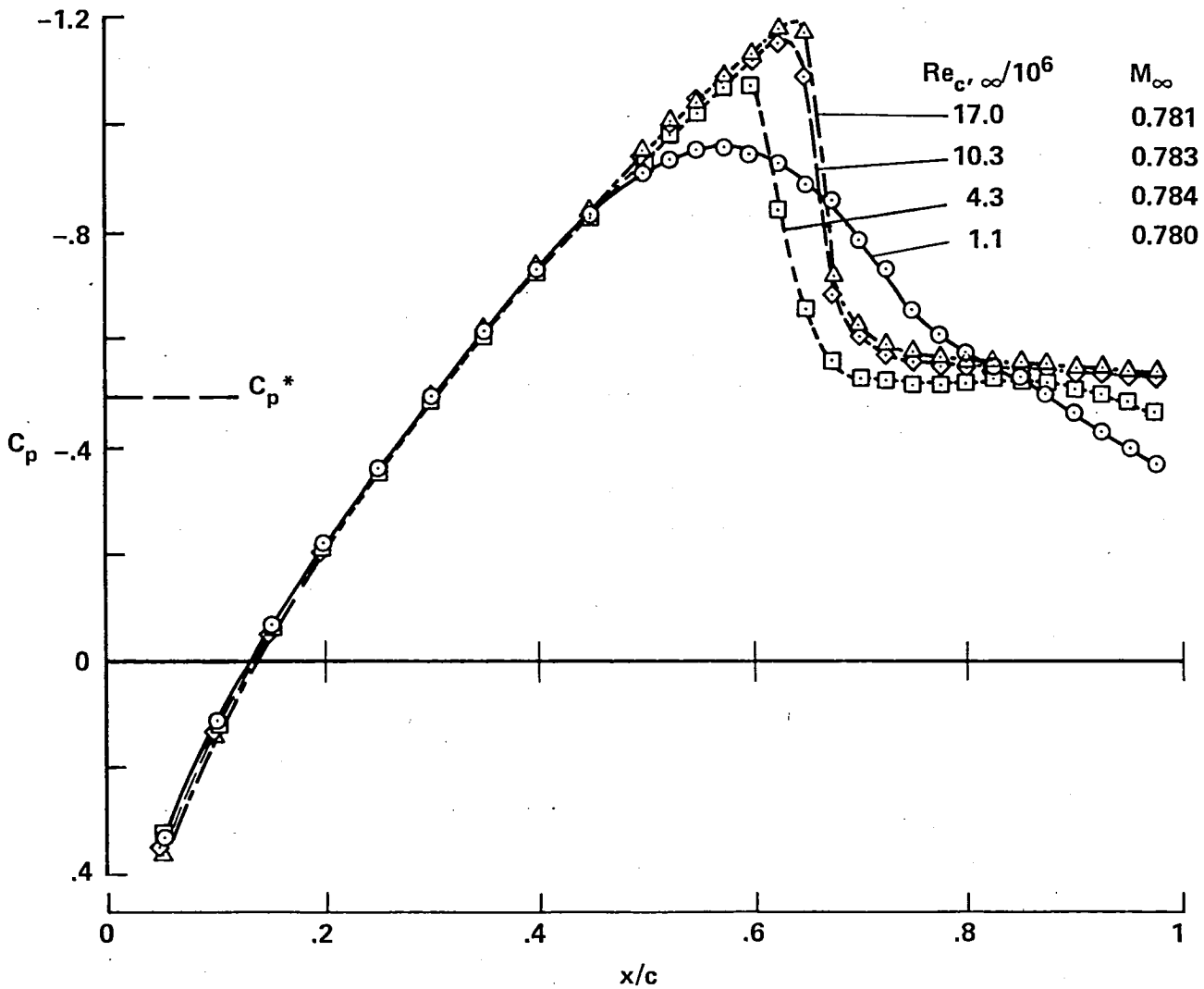

Figure 6.- Pressure distributions for steady flows at speeds above the buffeting region (from ref. 2).

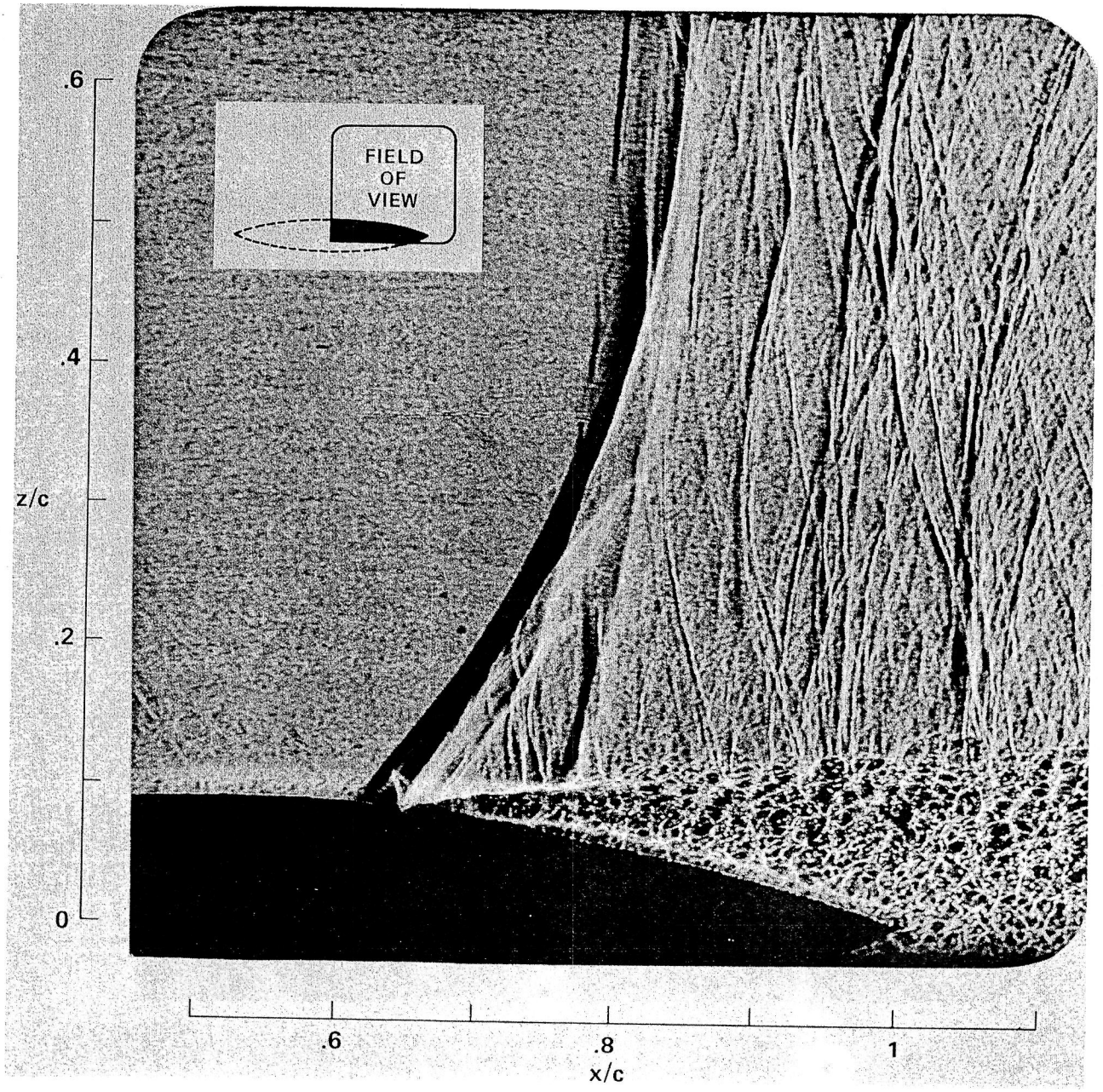

Figure 7.- Flow-field shadowgraph, $M_\infty = 0.785$, $Re_{c,\infty} = 11 \times 10^6$.

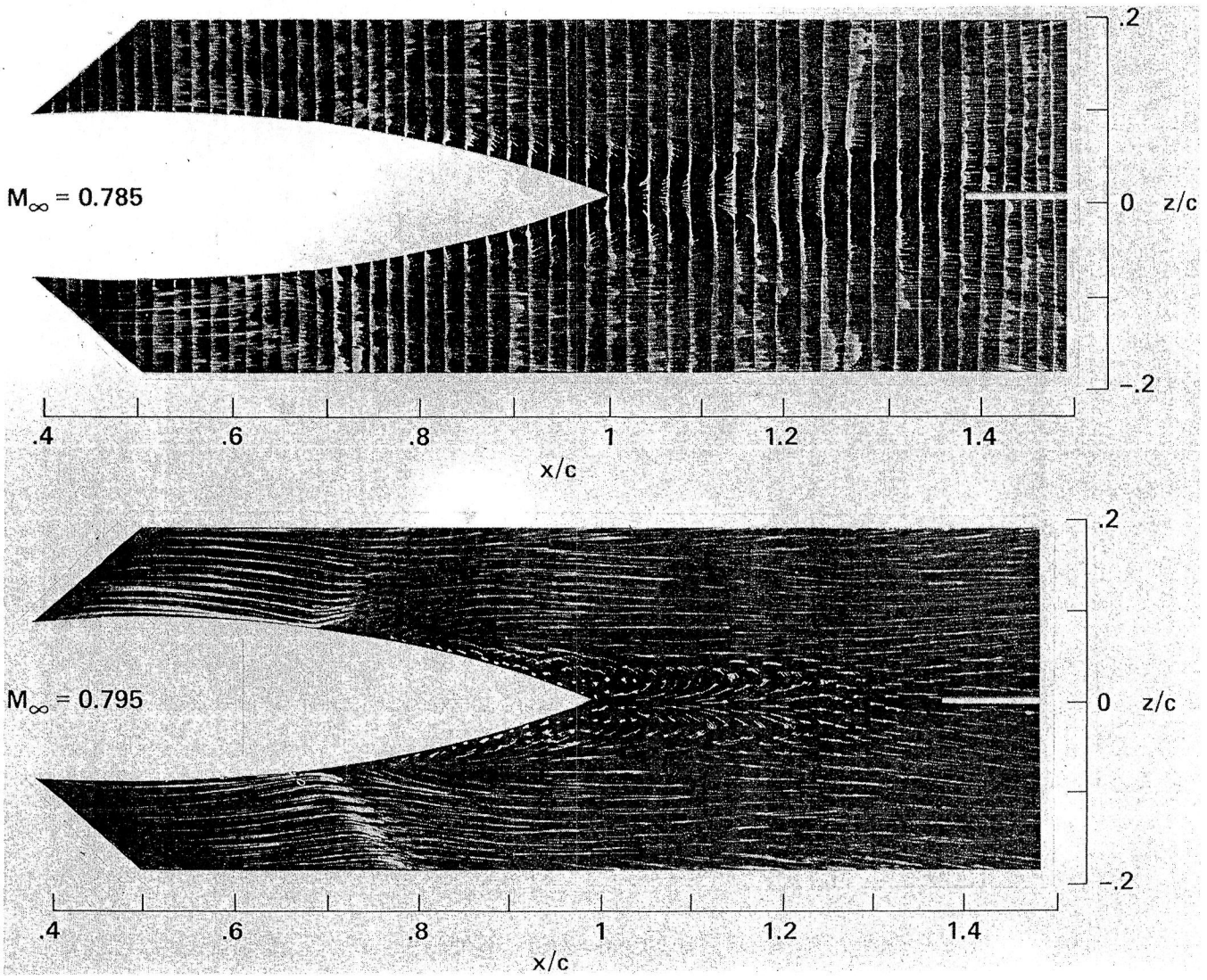

Figure 8.- Oil-flow patterns on vertical fences.

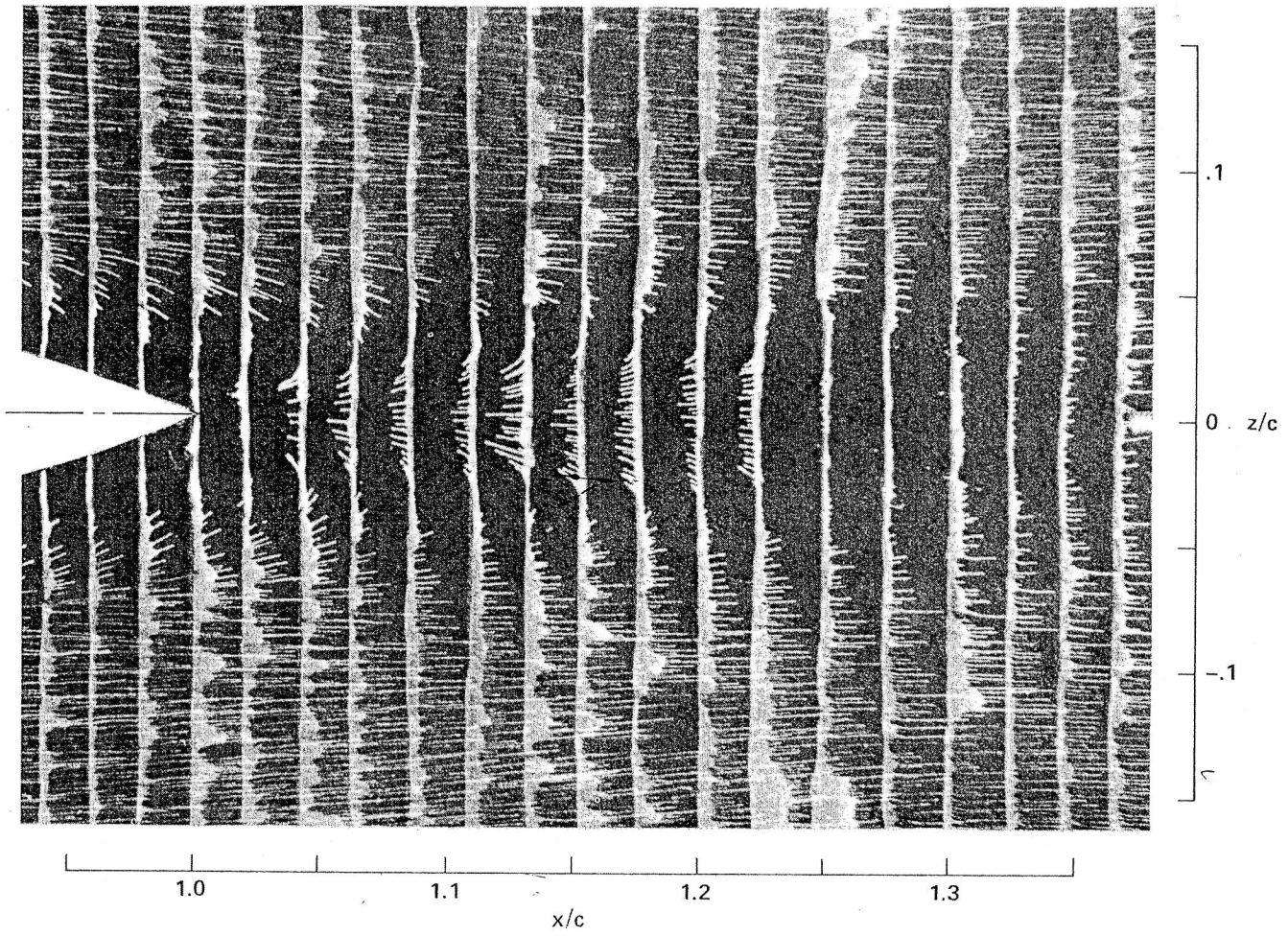

Figure 9.- Oil-flow details downstream of airfoil trailing edge, $M_\infty = 0.785$, $Re_{c,\infty} = 11 \times 10^6$.

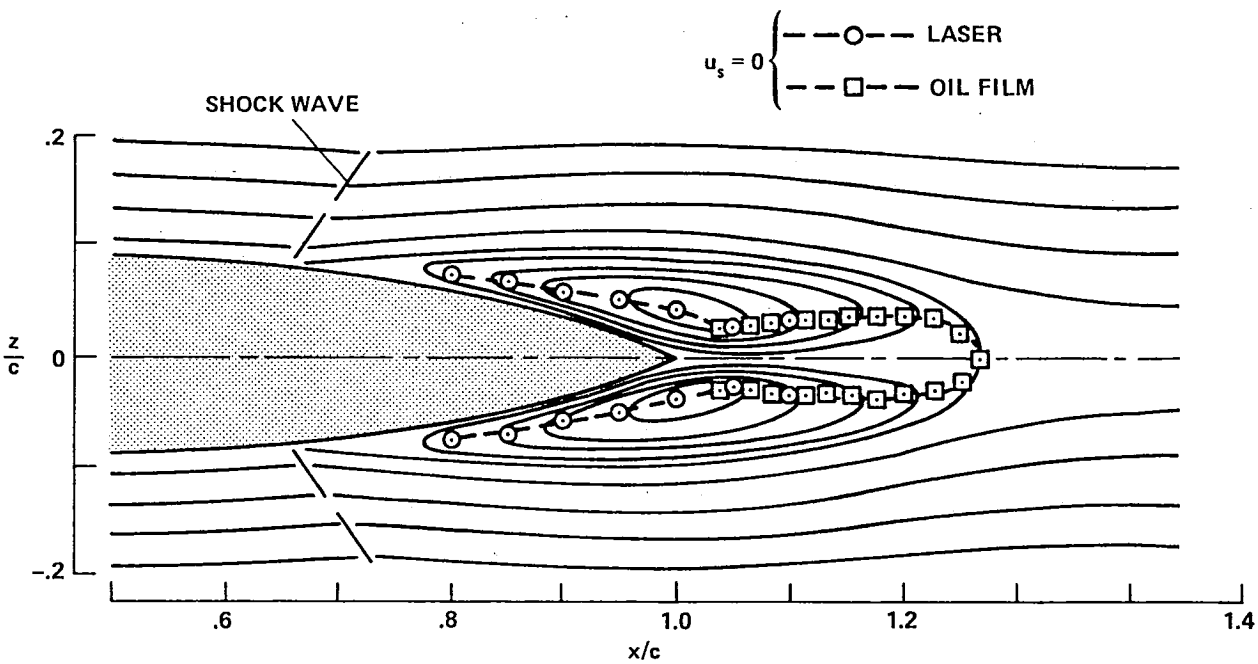

Figure 10.- Wake streamlines, shock-induced separation; $M_\infty = 0.785$, $Re_{c,\infty} = 11 \times 10^6$.

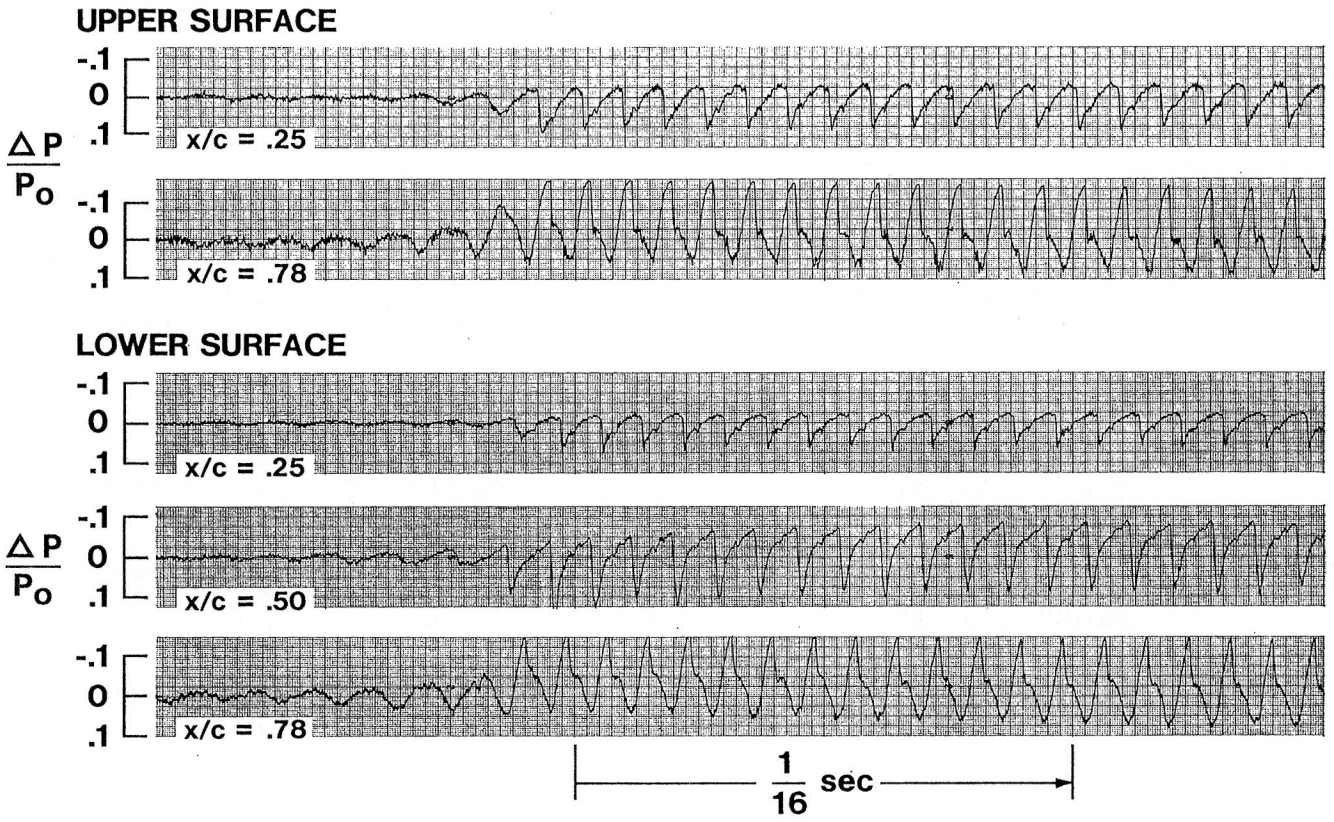

Figure 11.- Oscillograph traces of pressure fluctuations at onset of buffeting; $M_\infty = 0.76$, $\partial M_\infty/\partial t = 0.001$, $Re_{c,\infty} = 11\times10^6$.

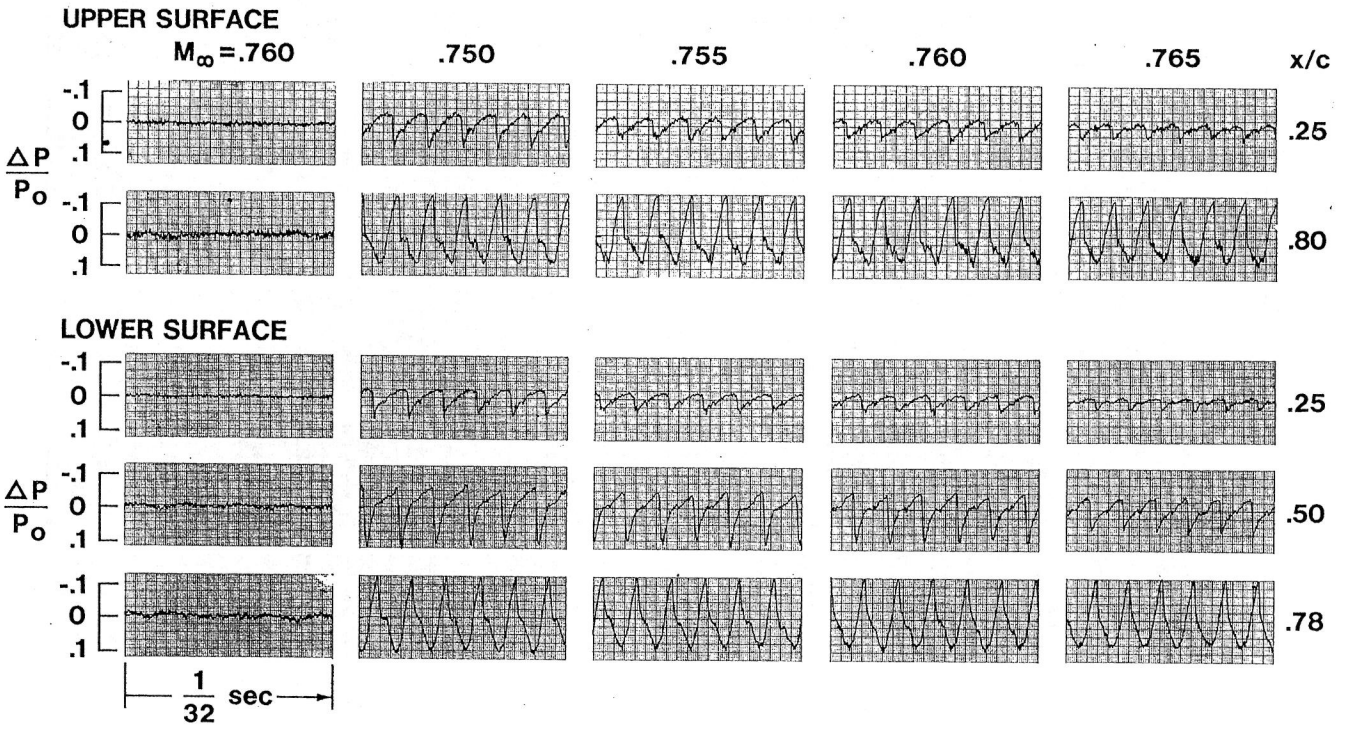

(a) M_∞ = 0.760 (steady flow) and unsteady flows from M_∞ = 0.750 to 0.765.

Figure 12.- Pressure fluctuations, $Re_{c,\infty} = 11\times10^6$, $\partial M_\infty/\partial t = 0.001$.

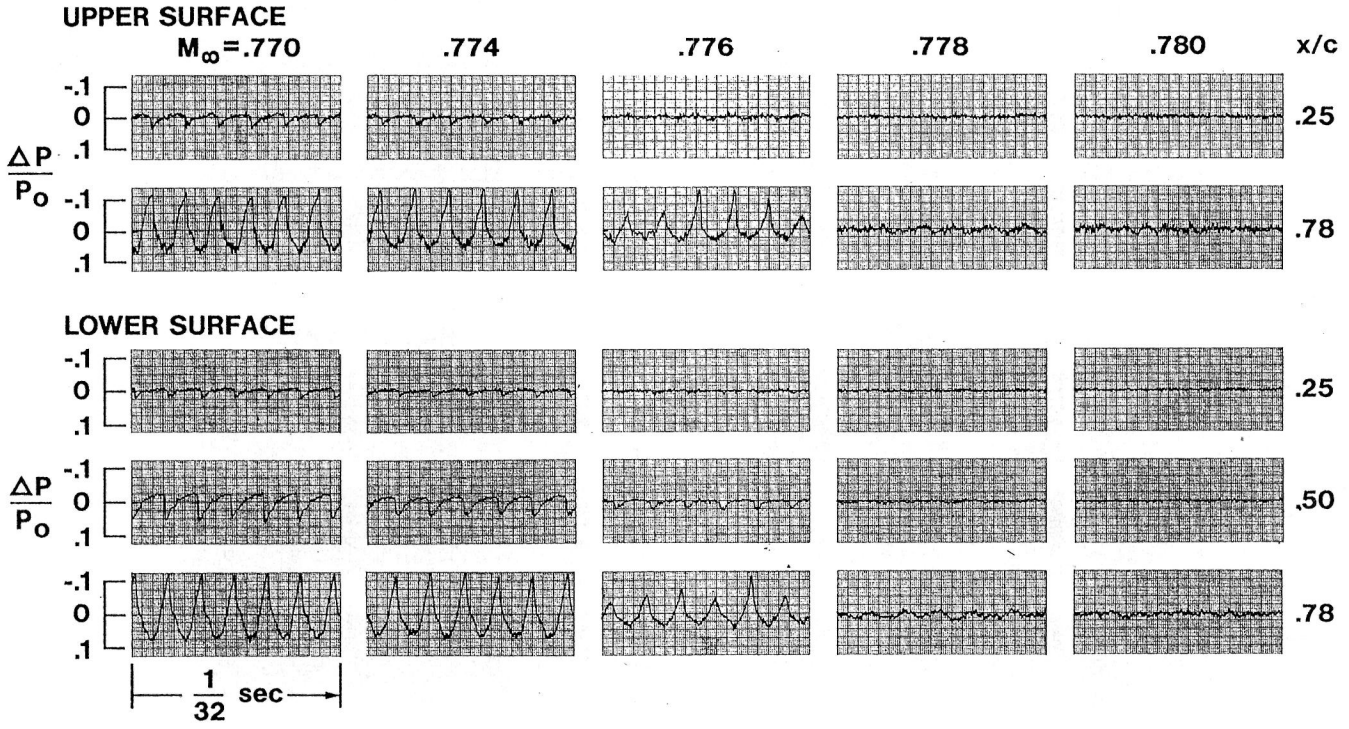

(b) M_∞ = 0.770 to 0.780.

Figure 12.- Concluded.

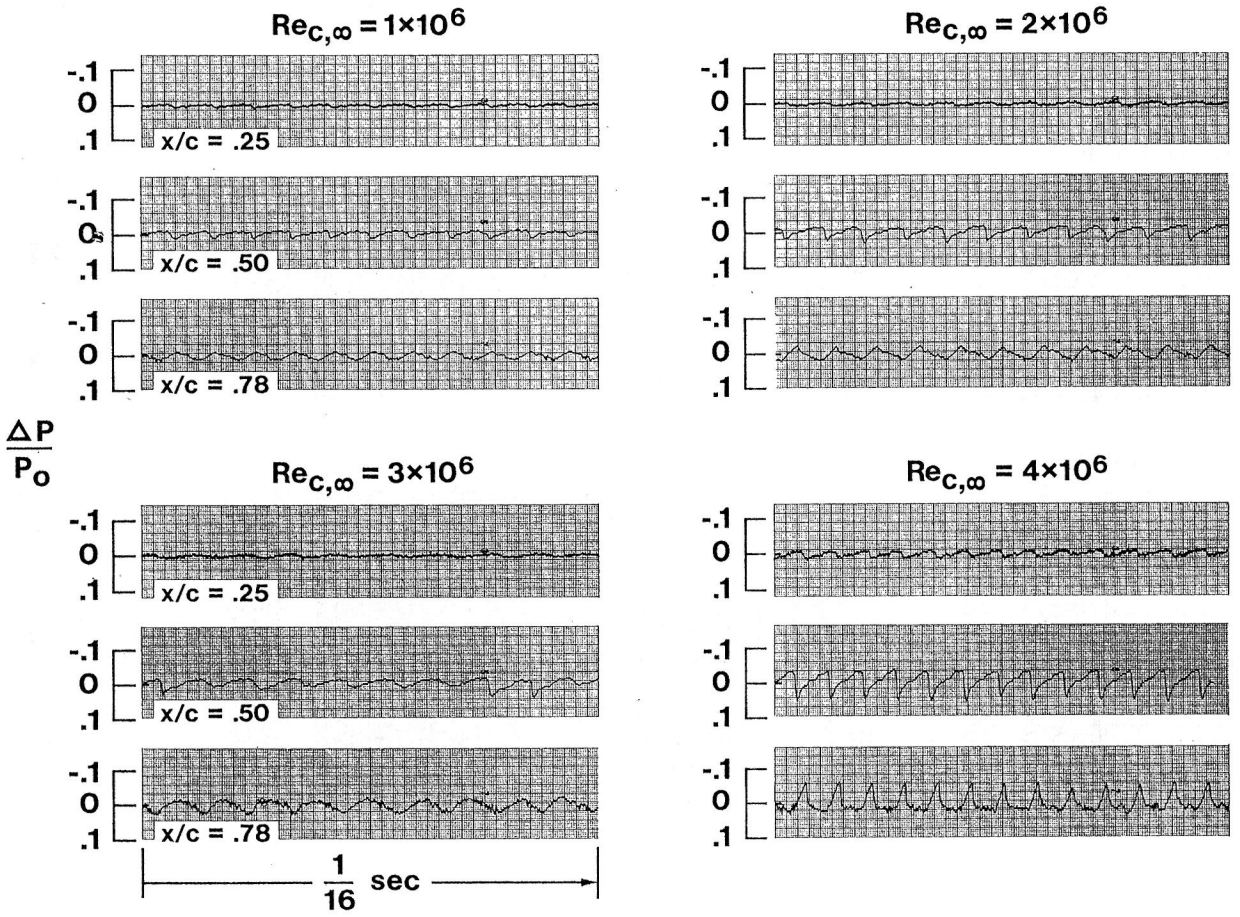

(a) $Re_{c,\infty} = 1\times10^6$ to 4×10^6.

Figure 13.- Effect of Reynolds number on pressure fluctuations, $M_\infty = 0.770$.

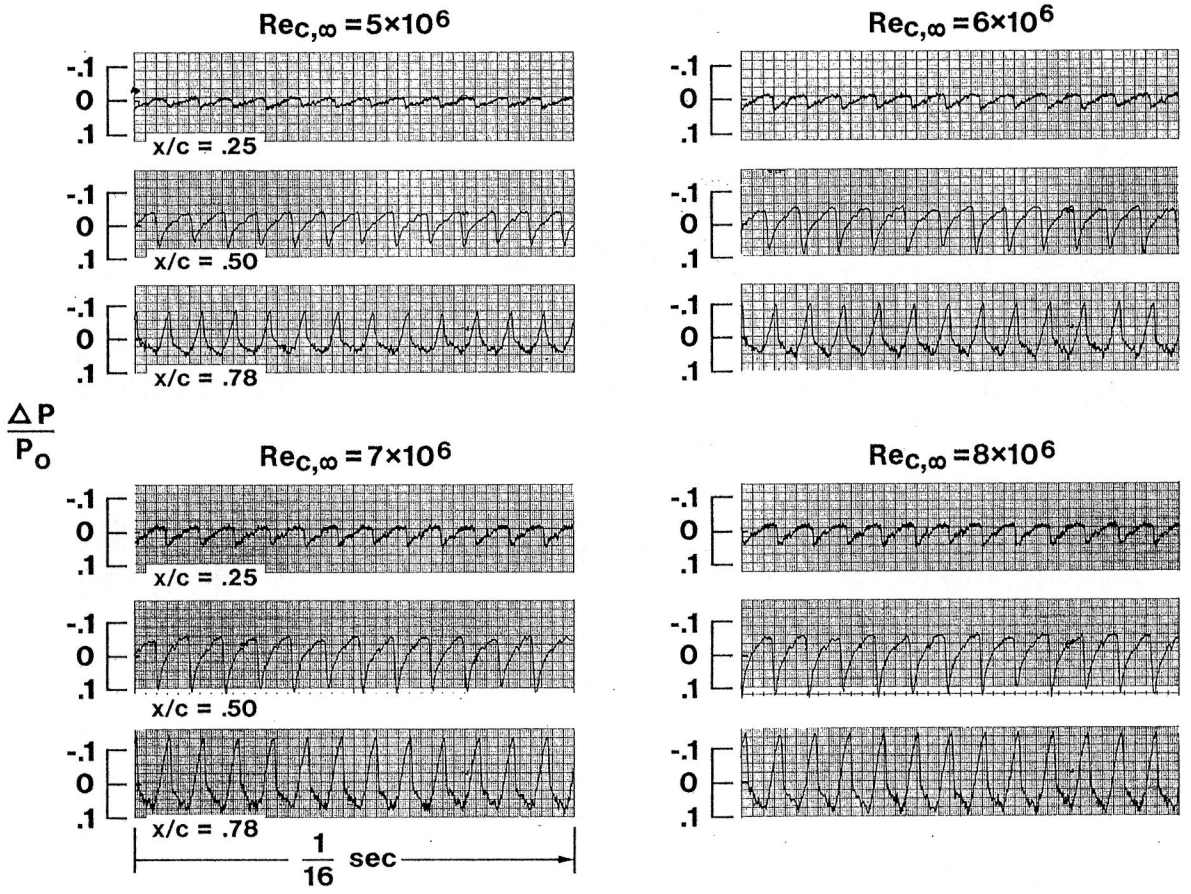

(b) $Re_{c,\infty} = 5\times10^6$ to 8×10^6.

Figure 13.- Concluded.

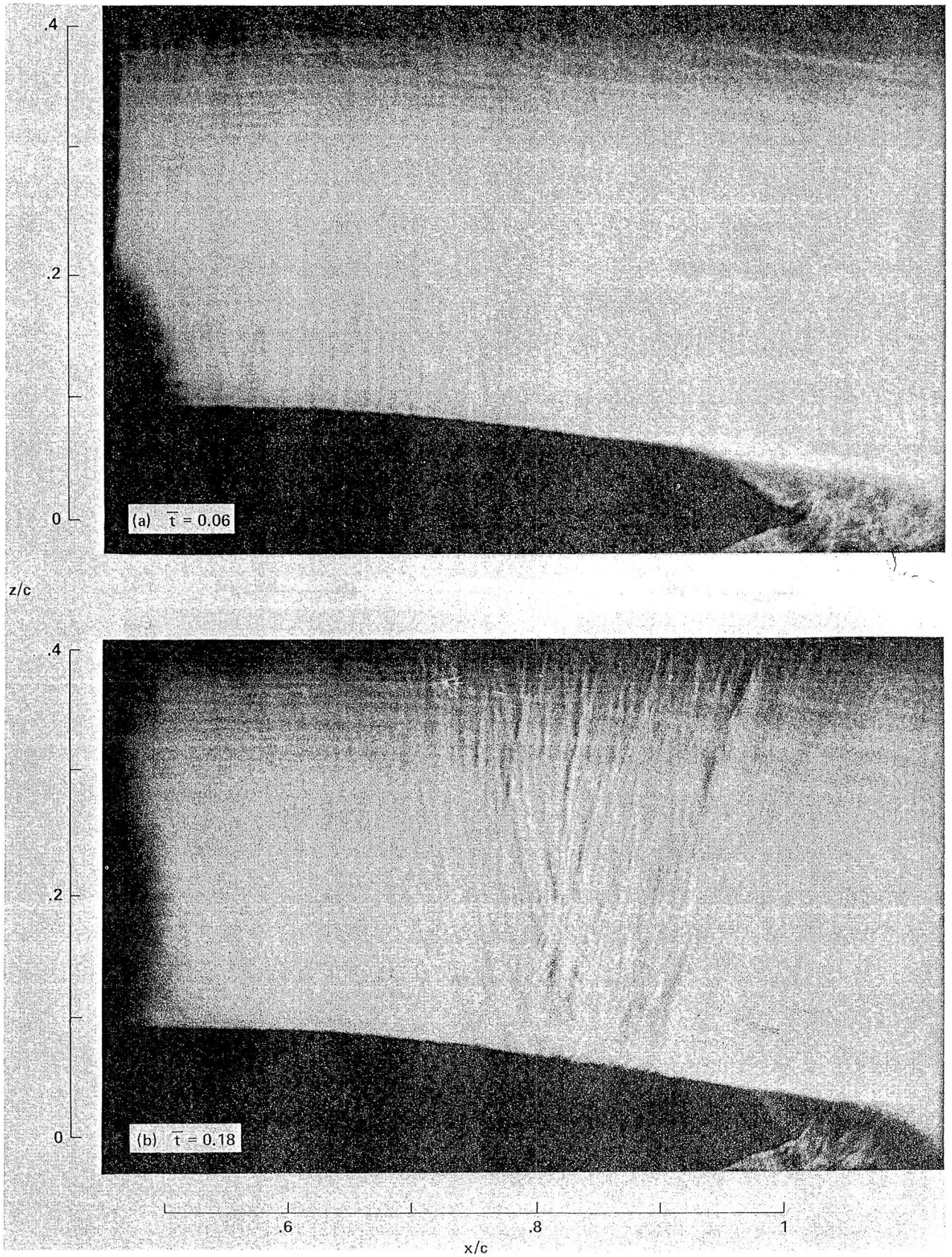

Figure 14.- Unsteady flow-field shadowgraphs; $M_\infty = 0.76$, $Re_{c,\infty} = 11 \times 10^6$.

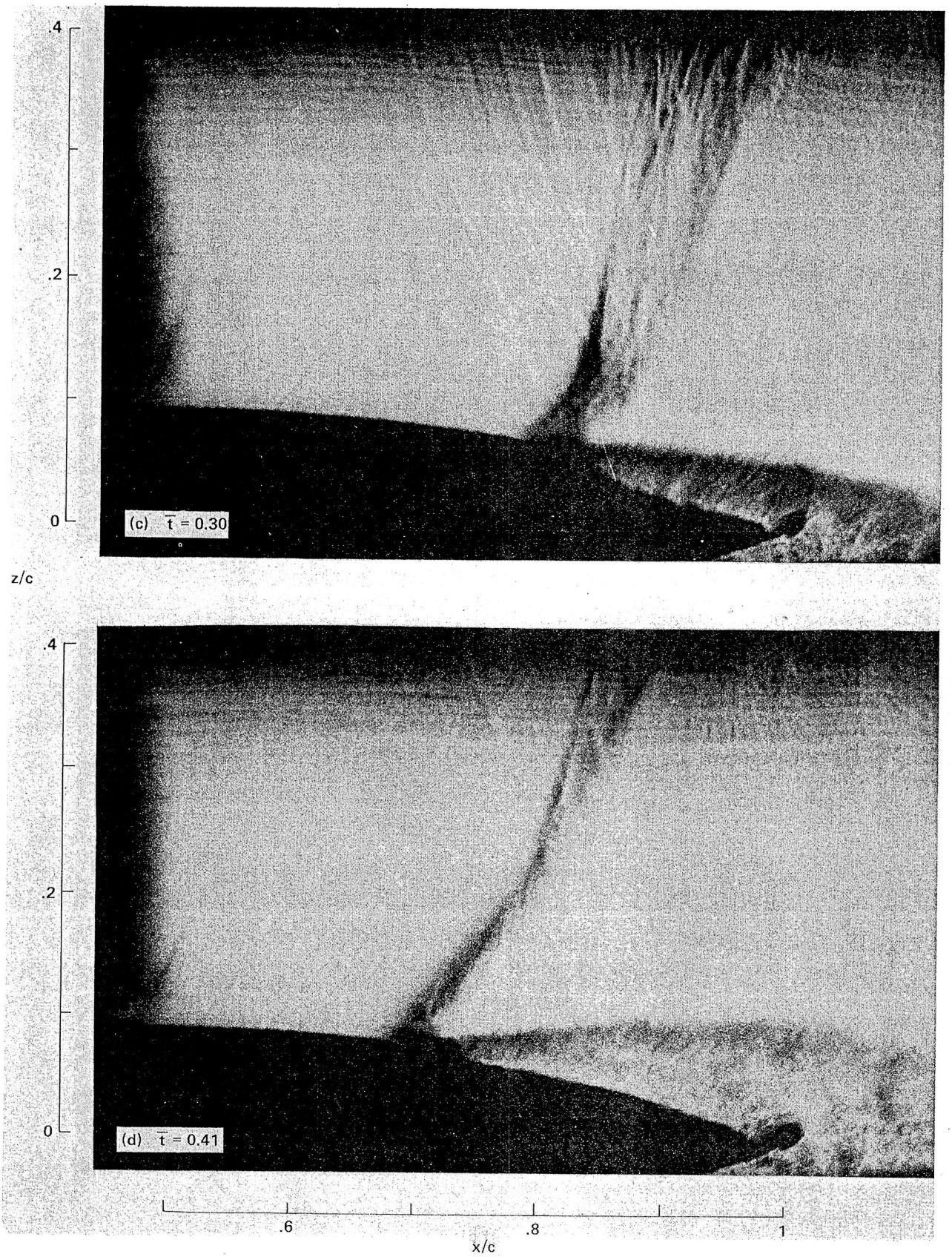

Figure 14.- Continued.

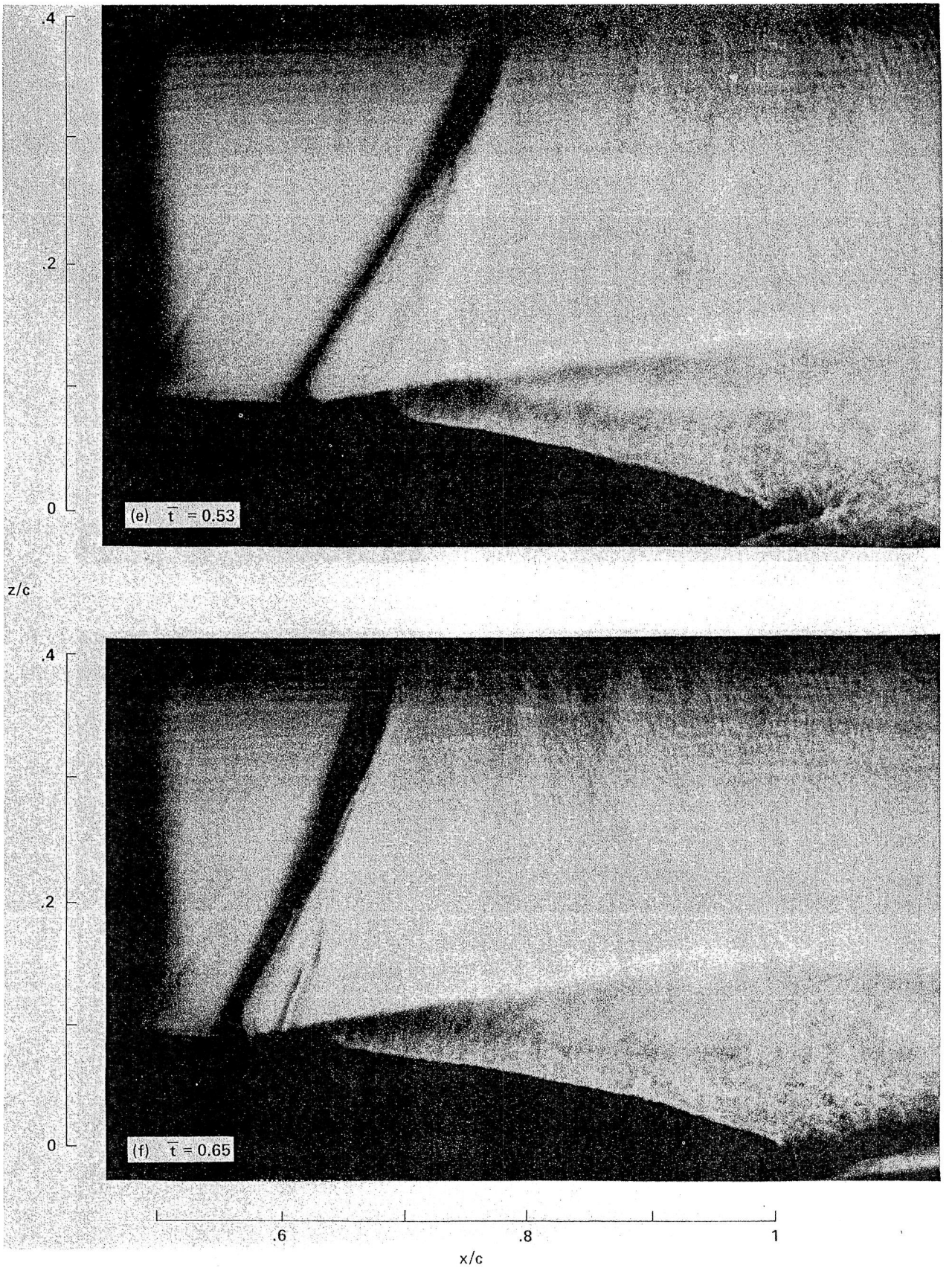

Figure 14.- Continued.

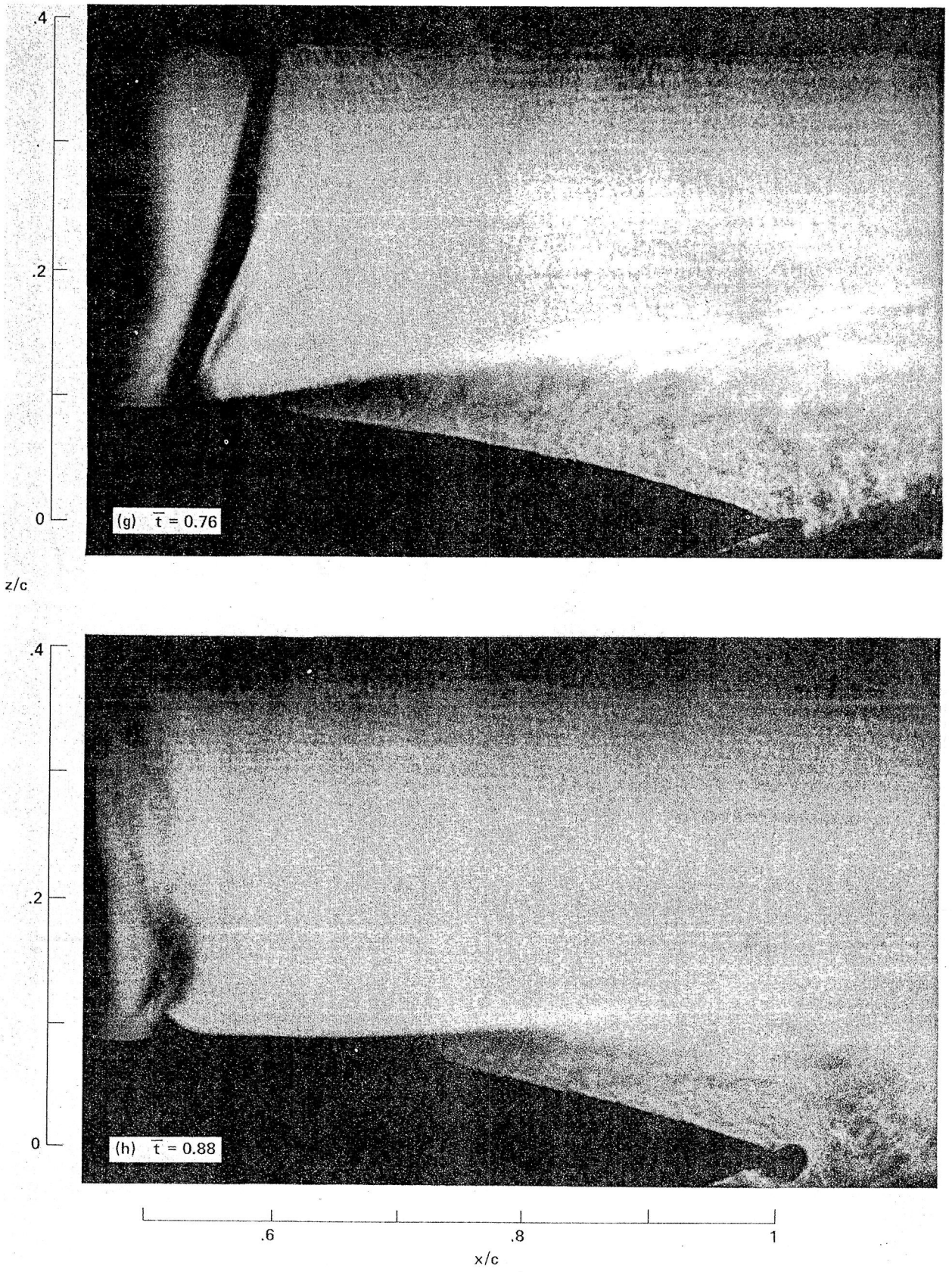

Figure 14.- Concluded.

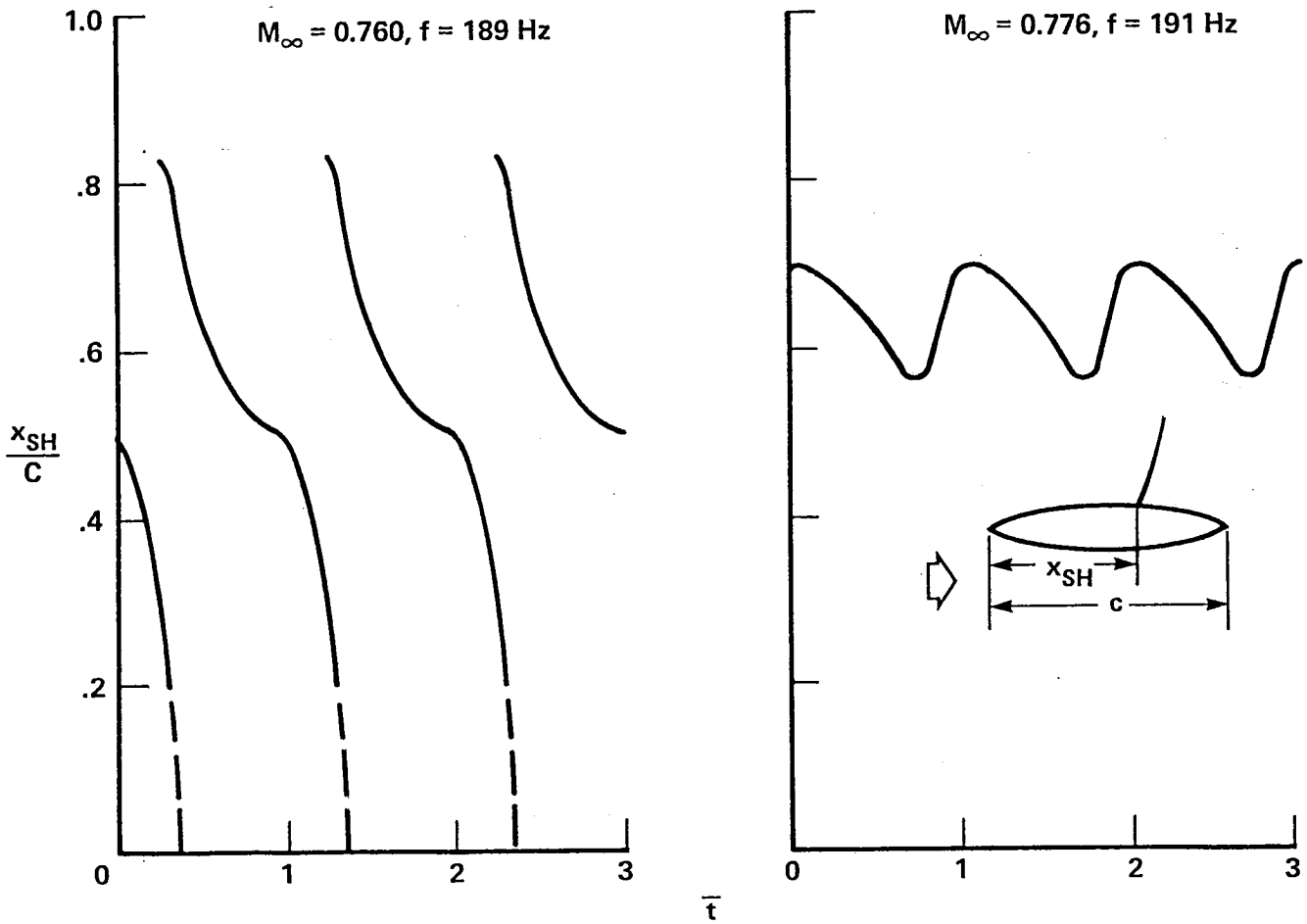

Figure 15.- Shock motions in unsteady flow, $Re_{c,\infty} = 11 \times 10^6$.

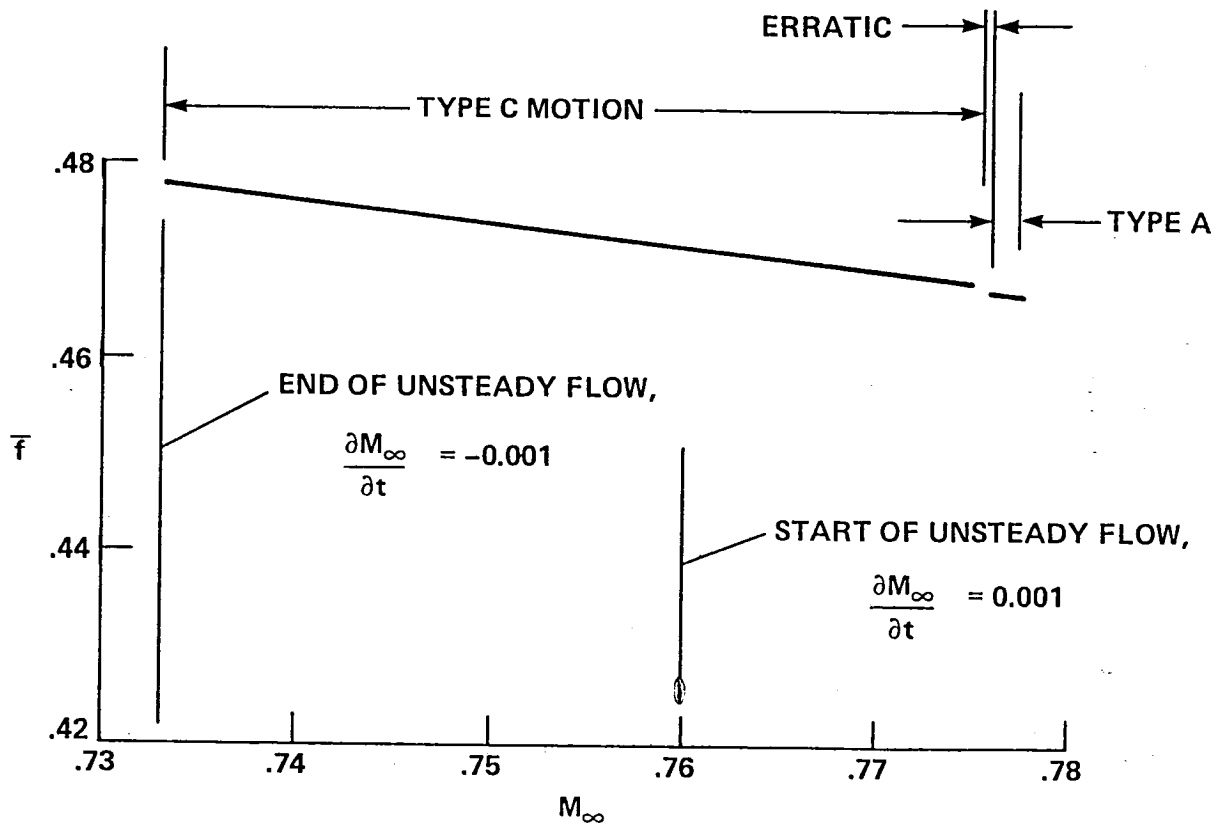

Figure 16.- Frequency of unsteady flow oscillation; $\alpha = 0°$, $Re_{c,\infty} = 11 \times 10^6$, $T_\infty \approx 270$ K.

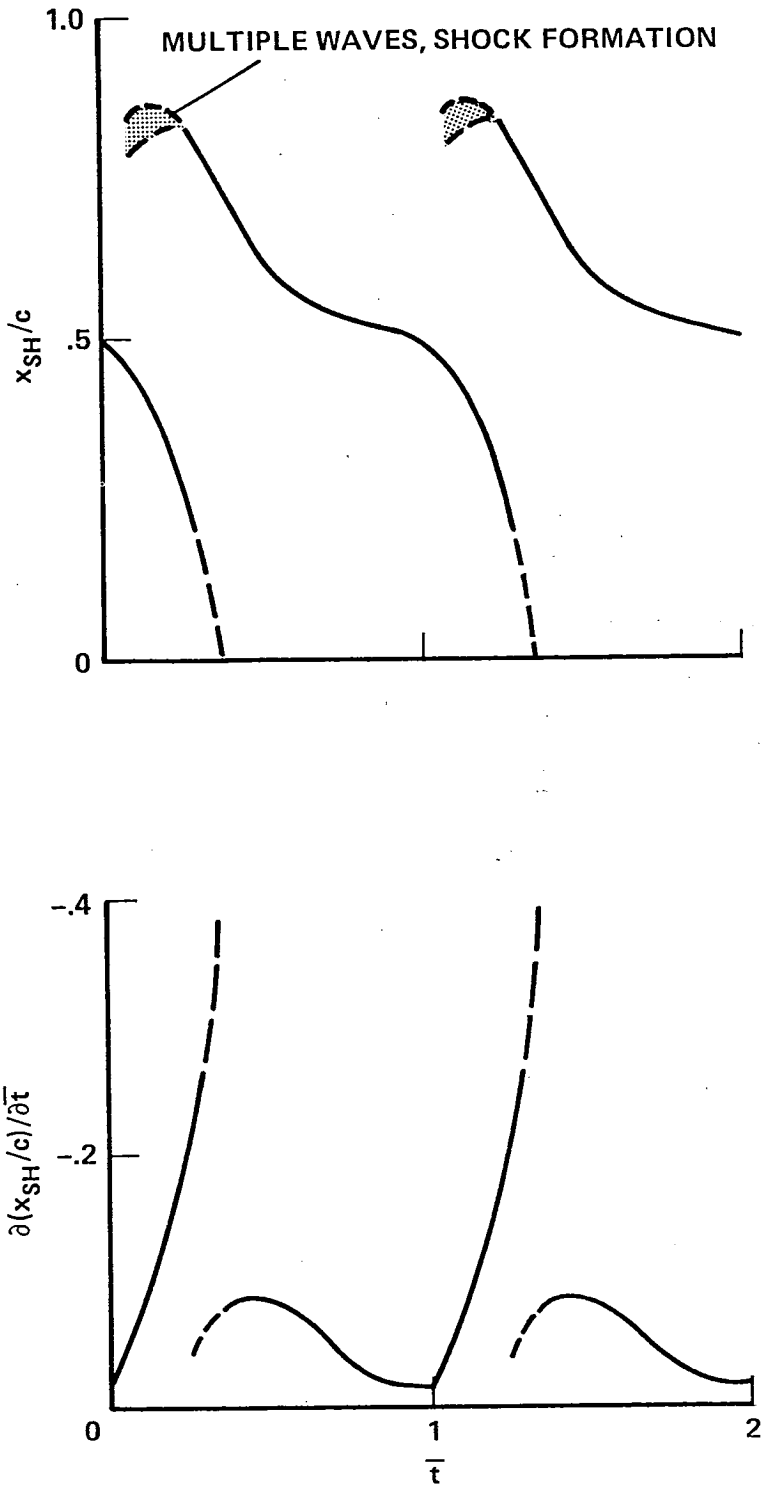

Figure 17.- Cyclic shock motion; $M_\infty = 0.76$, $Re_{c,\infty} = 11\times10^6$.

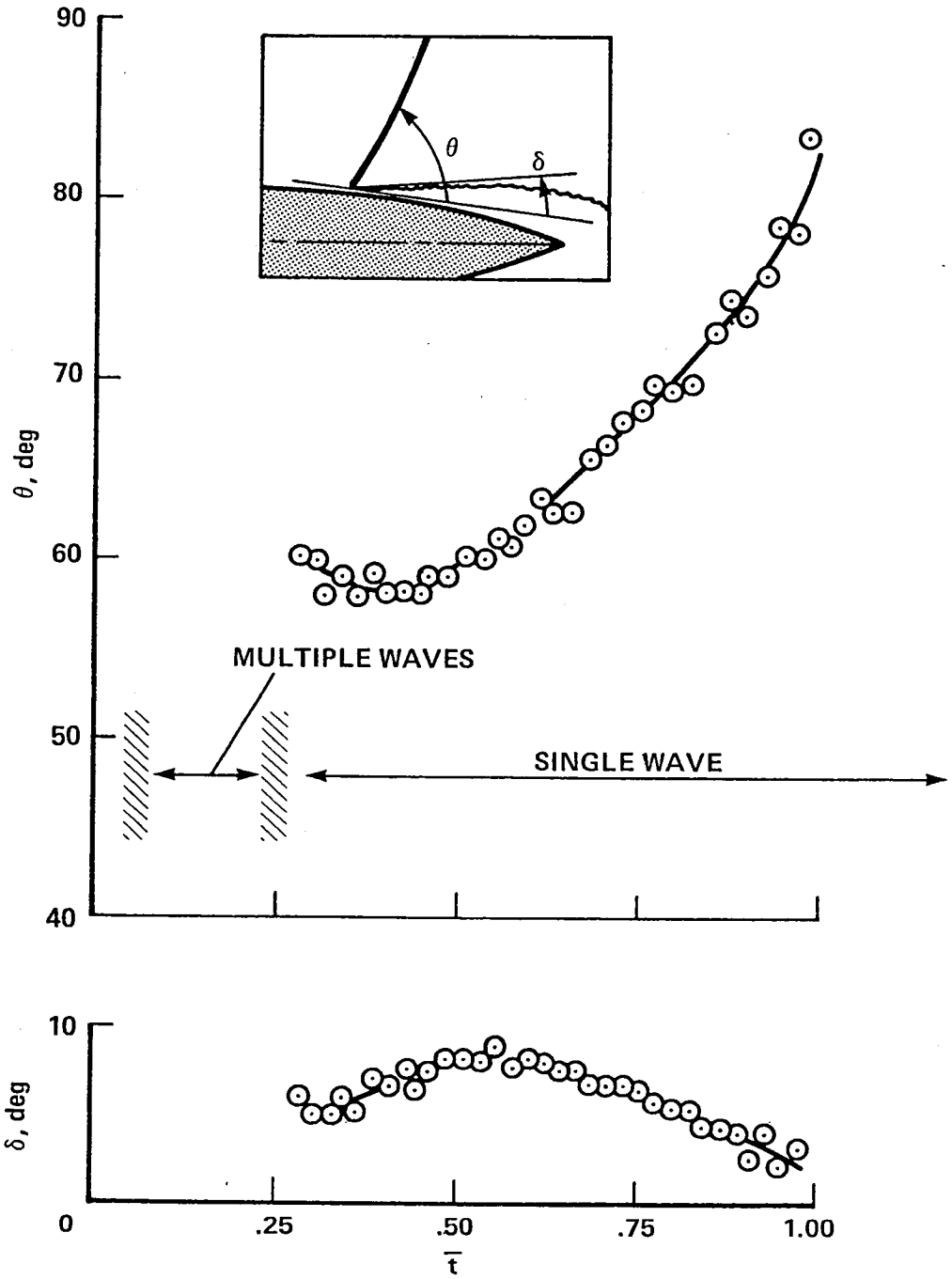

Figure 18.- Cyclic shock wave and flow deflection angles; $M_\infty = 0.76$, $Re_{c,\infty} = 11 \times 10^6$.

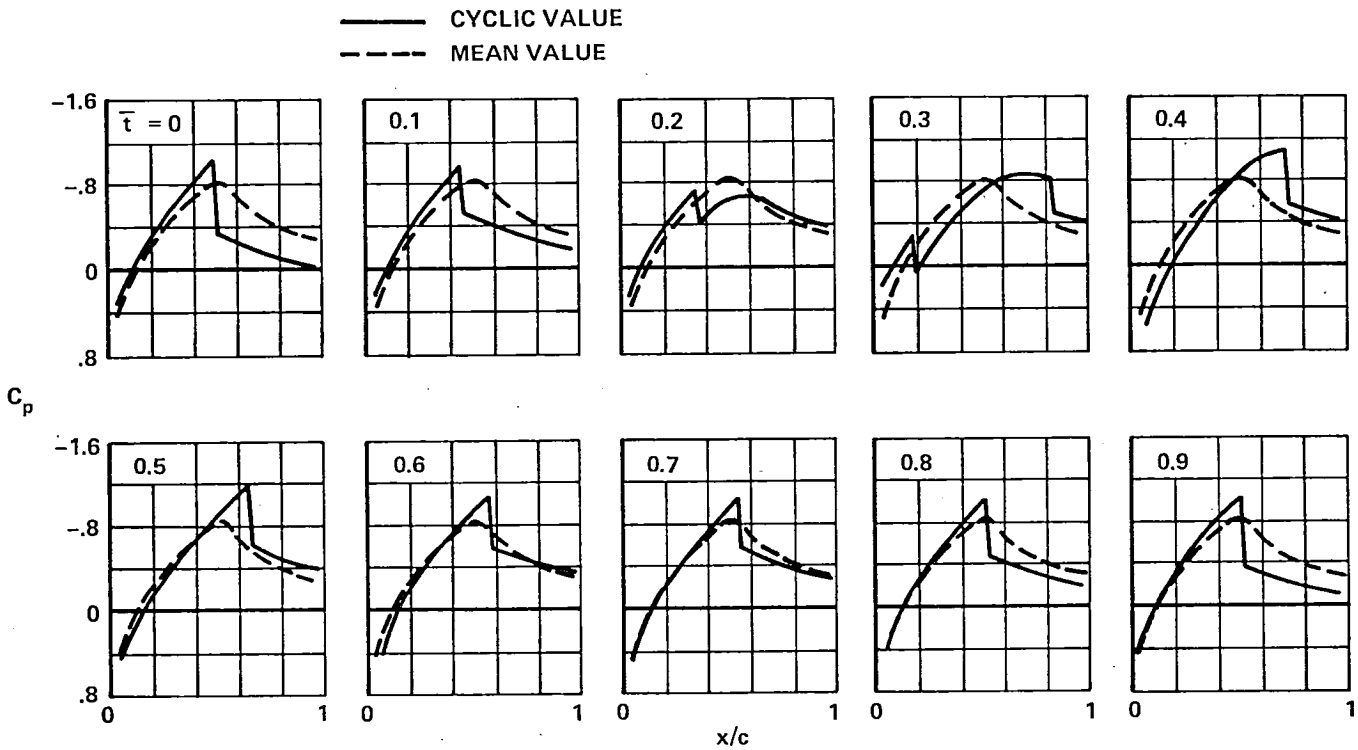

Figure 19.- Mean and instantaneous airfoil chordwise pressure distributions in unsteady flow; $M_\infty = 0.76$, $Re_{c,\infty} = 11 \times 10^6$, f = 189 Hz ($T_\infty \approx 270$ K).

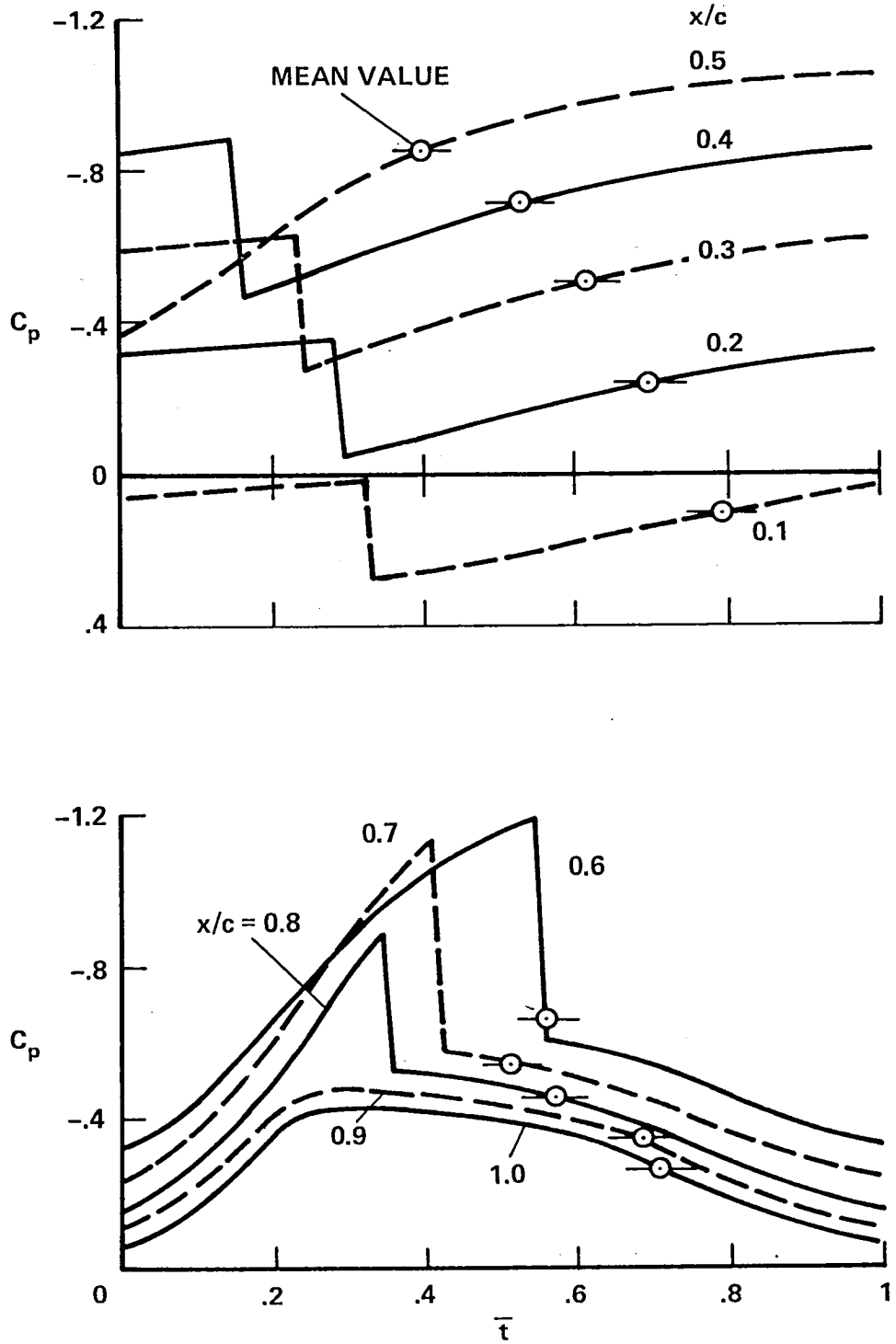

Figure 20.- Time histories of airfoil pressures; $M_\infty = 0.76$, $Re_{c,\infty} = 11 \times 10^6$, f = 189 Hz.

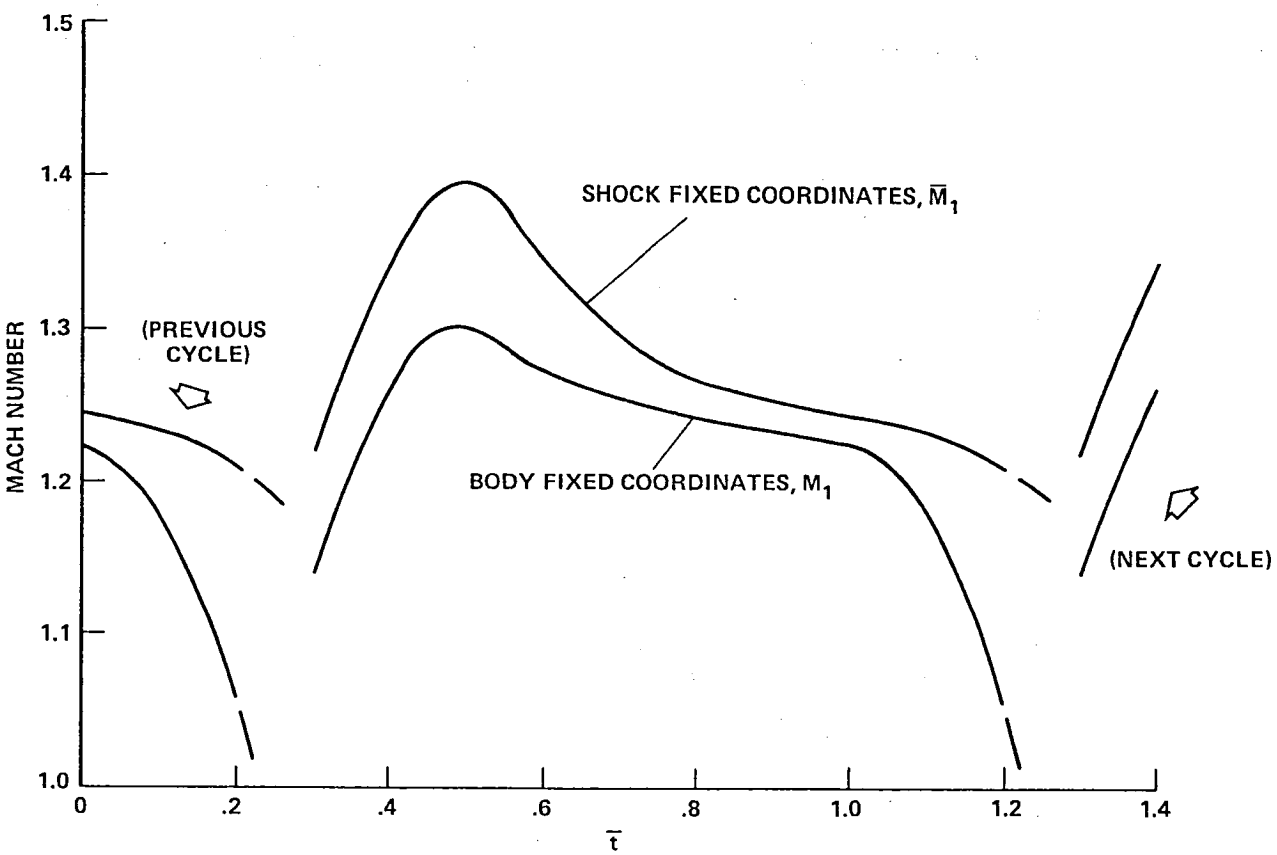

Figure 21.- Mach number ahead of shock wave at shear-layer edge; $M_\infty = 0.76$, $Re_{c,\infty} = 11 \times 10^6$.

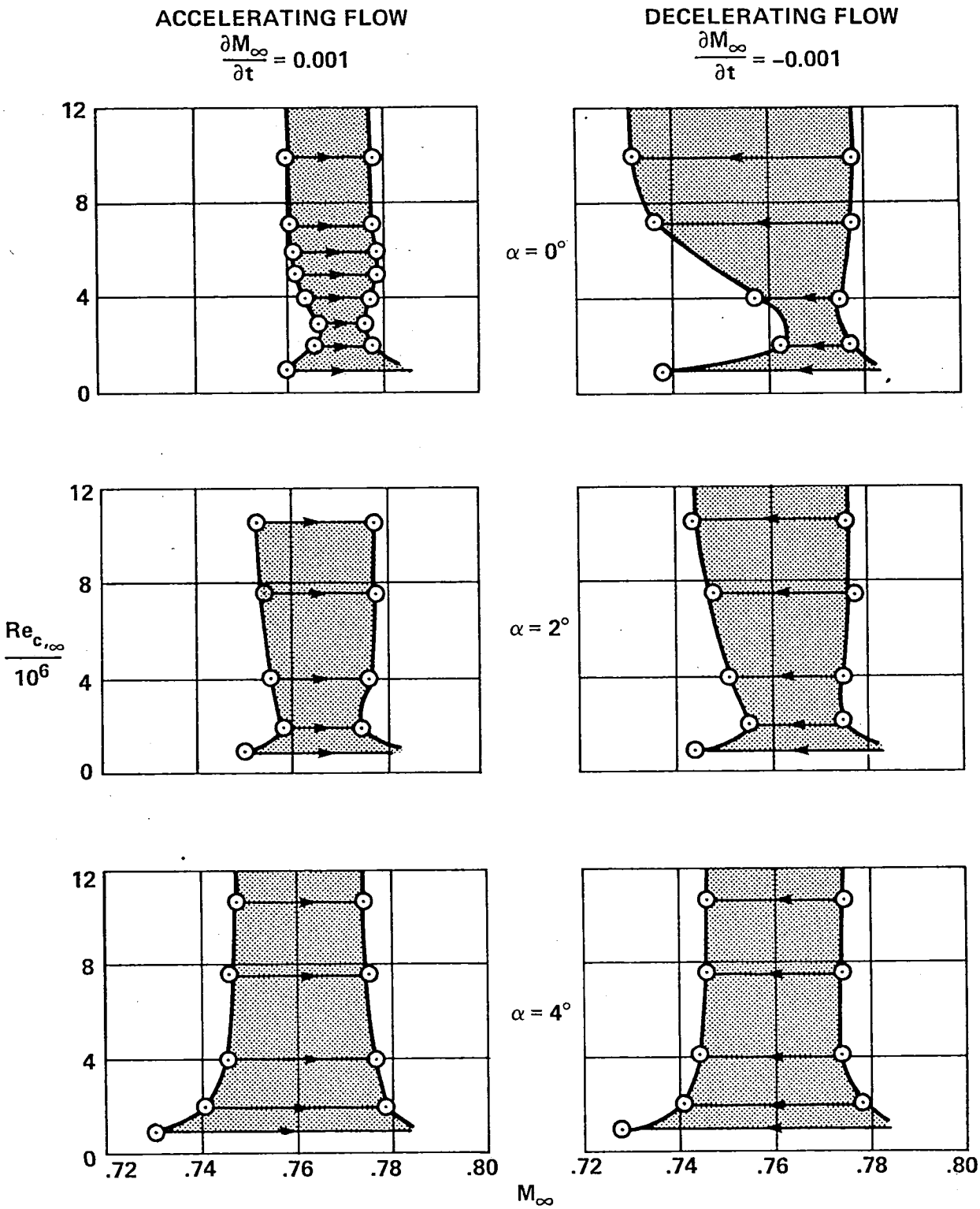

Figure 22.- Unsteady flow domains for $\alpha = 0°$, $2°$, and $4°$.

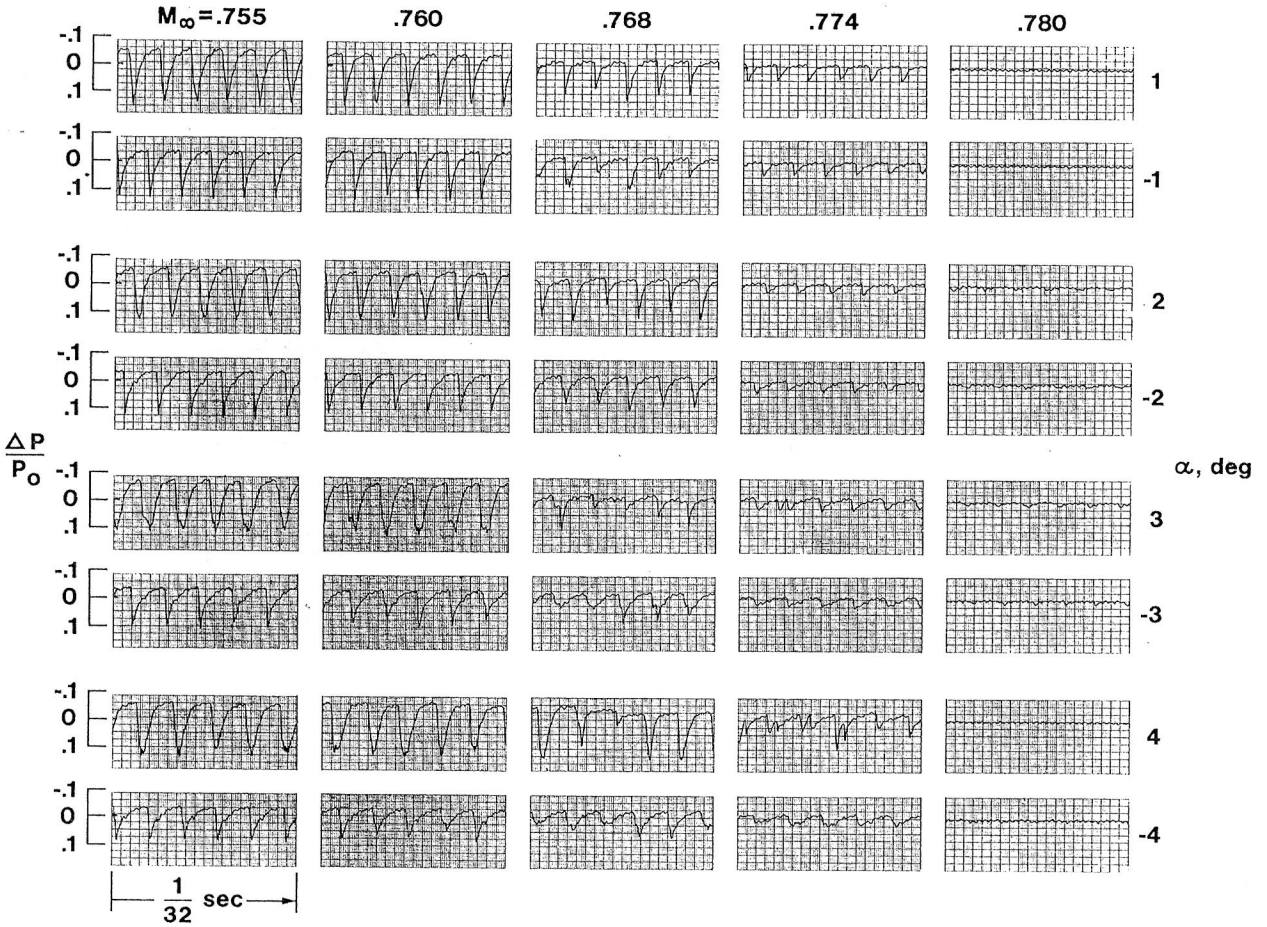

Figure 23.- Effect of Mach number on pressure fluctuations at angle of attack, $Re_{c,\infty} = 11 \times 10^6$.

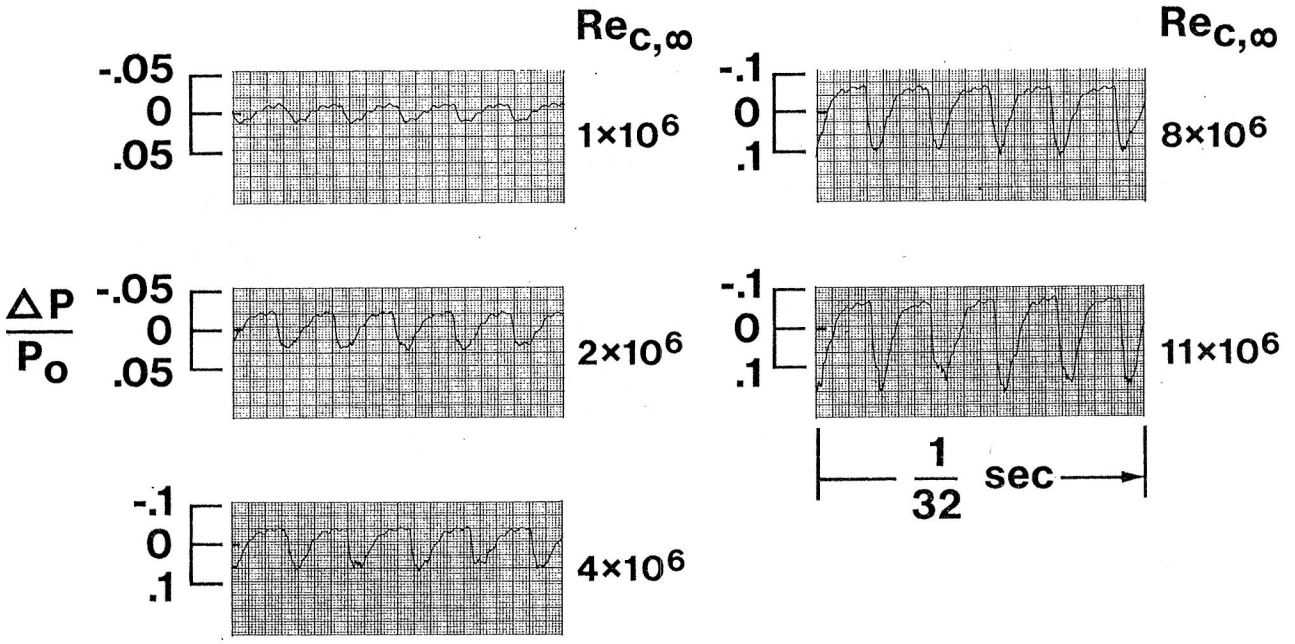

Figure 24.- Effect of Reynolds number on pressure fluctuations at $\alpha = 4°$, $M_\infty = 0.76$.

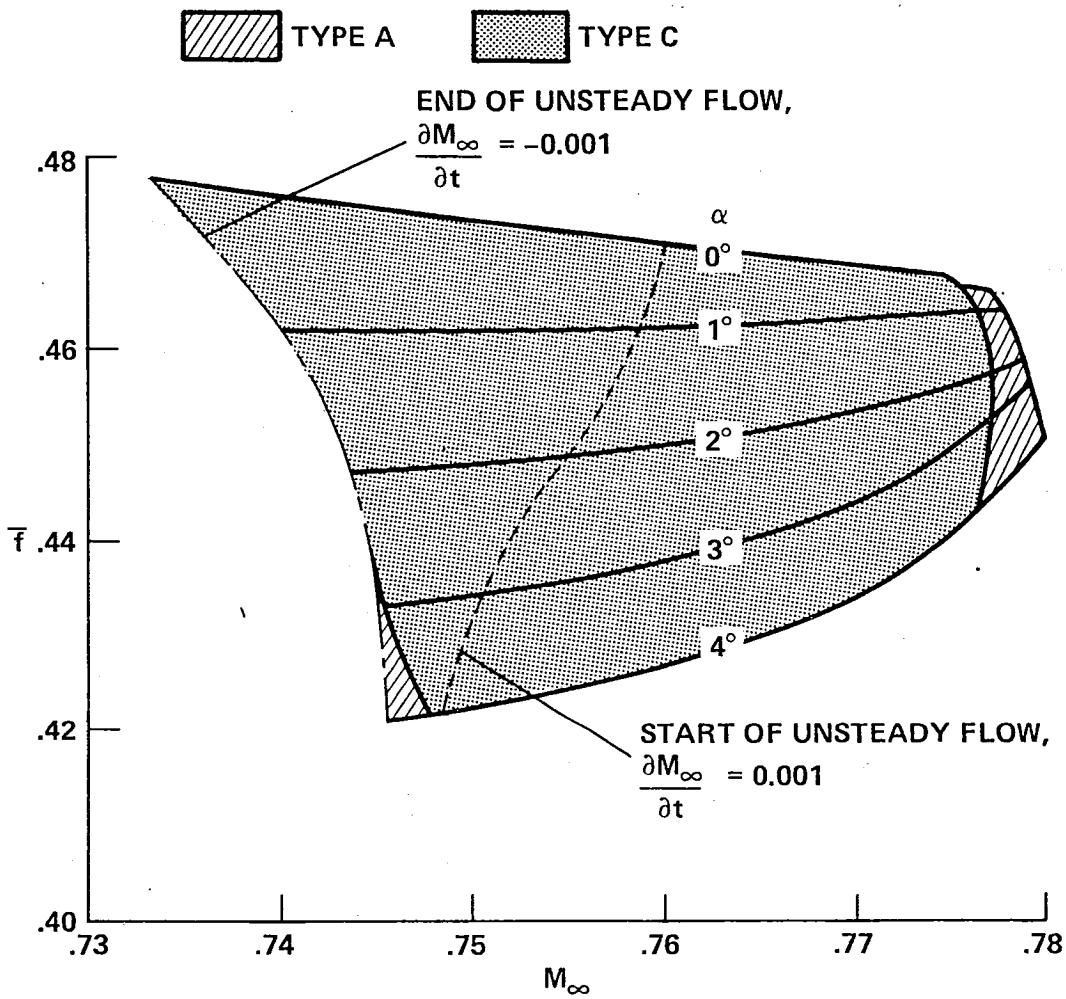

Figure 25.- Frequency of pressure fluctuations at angles of attack; $Re_{c,\infty} = 11 \times 10^6$, $T_\infty \approx 270$ K.

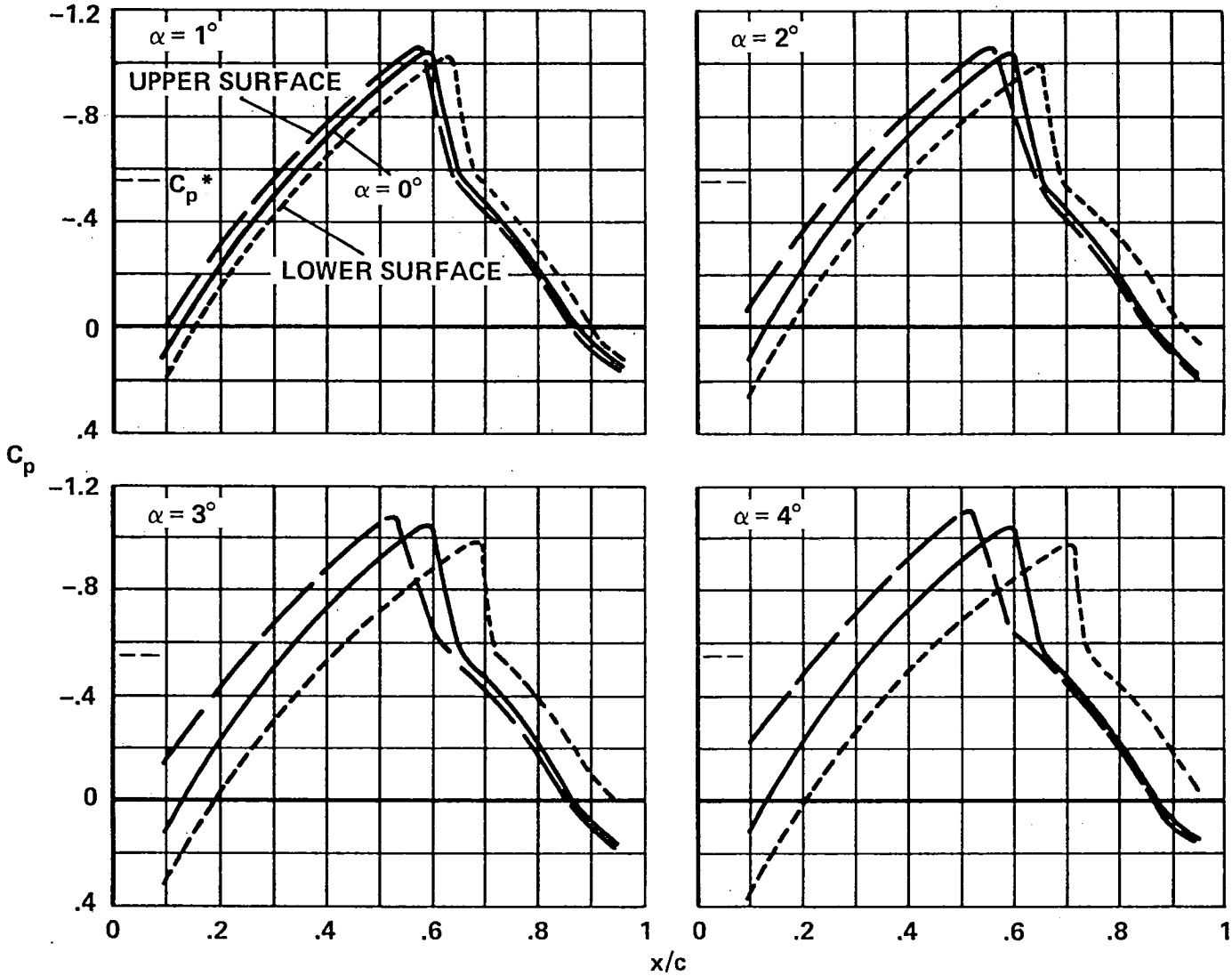

Figure 26.- Airfoil pressure distributions at angle of attack for steady flow with trailing-edge separation; $M_\infty = 0.745$, $Re_{c,\infty} = 11 \times 10^6$.

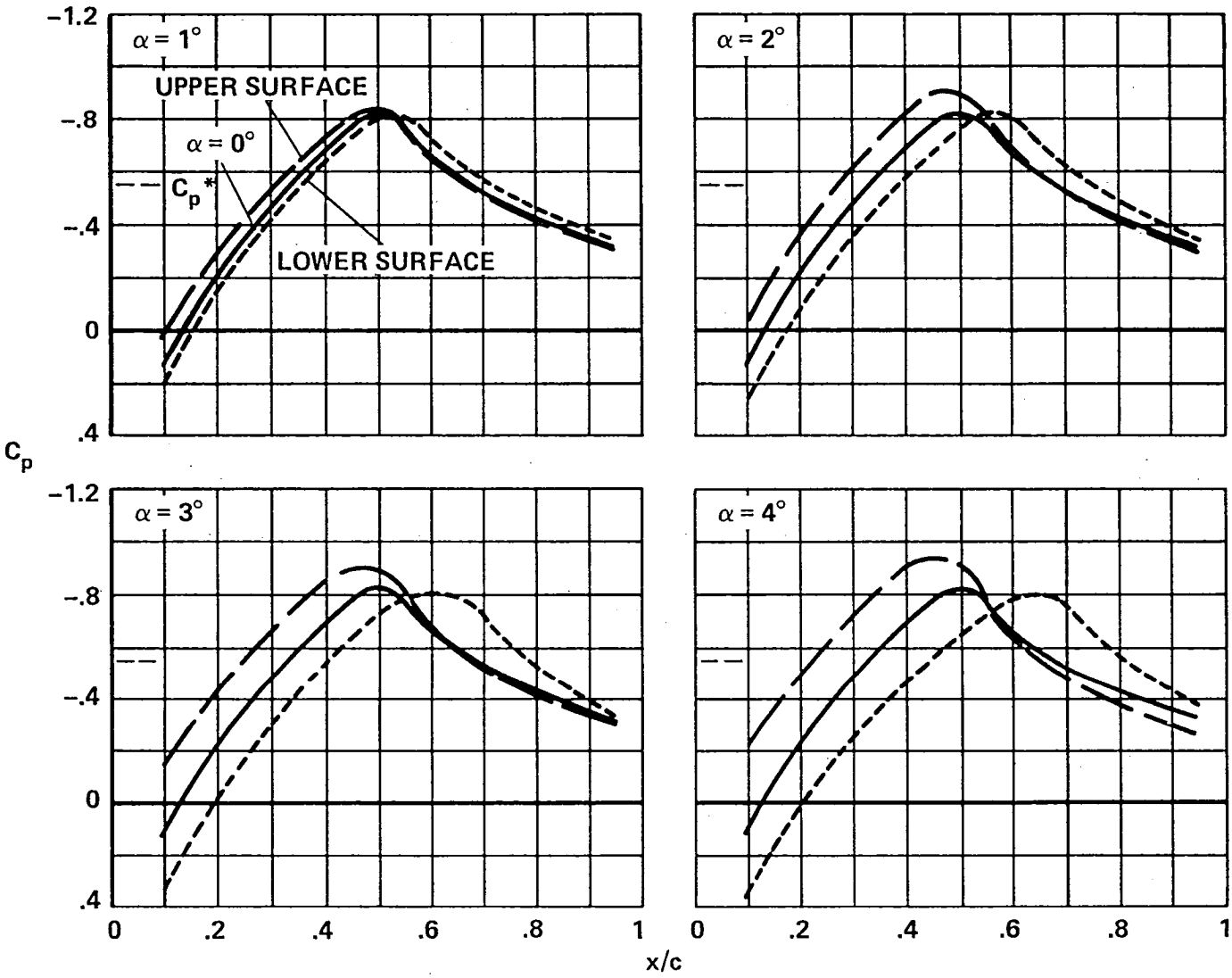

Figure 27.- Mean pressure measurements at angle of attack in unsteady flow; $M_\infty = 0.76$, $Re_{c,\infty} = 11 \times 10^6$.

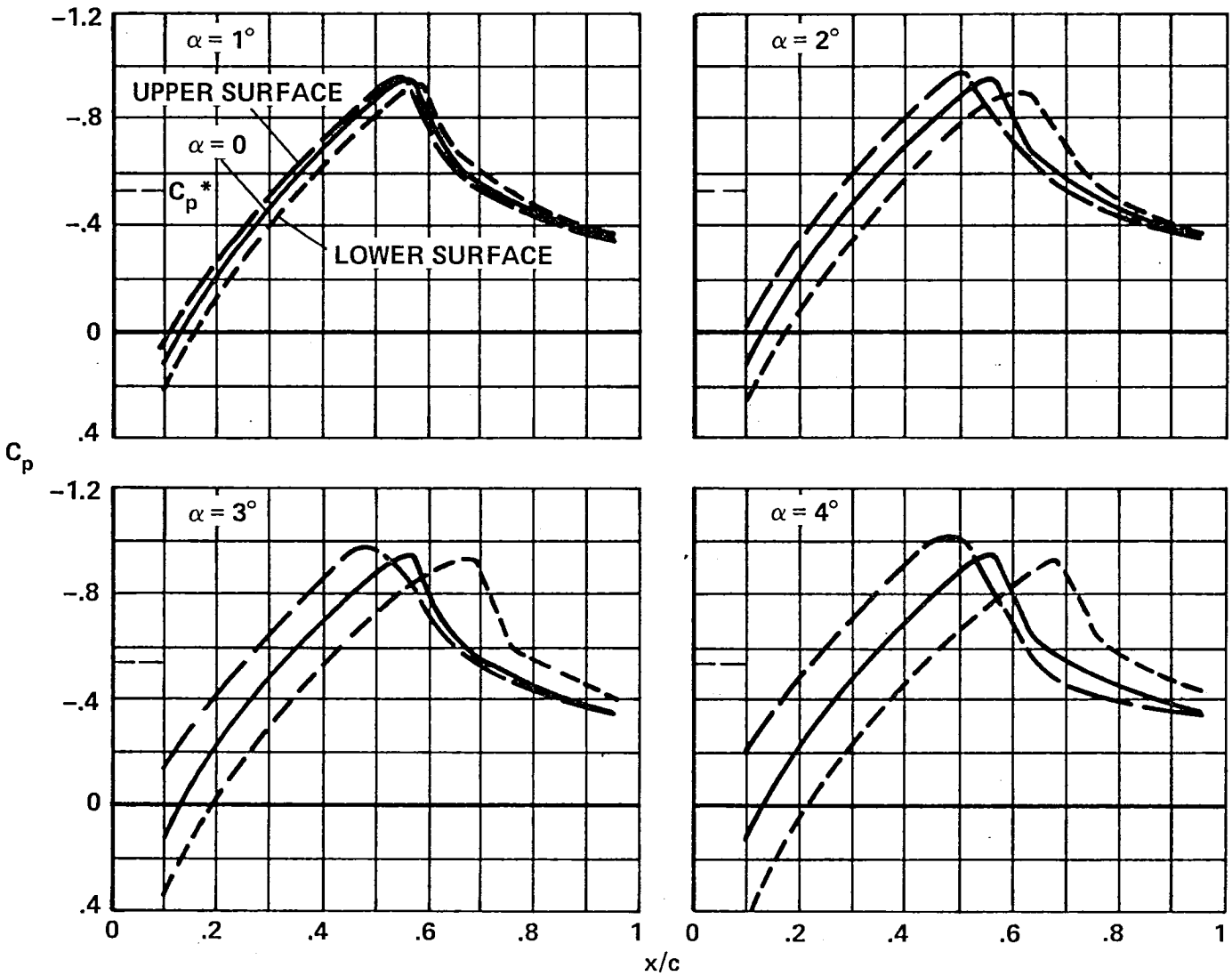

Figure 28.- Mean pressure measurements at angle of attack in unsteady flow; $M_\infty = 0.77$, $Re_{c,\infty} = 11 \times 10^6$.

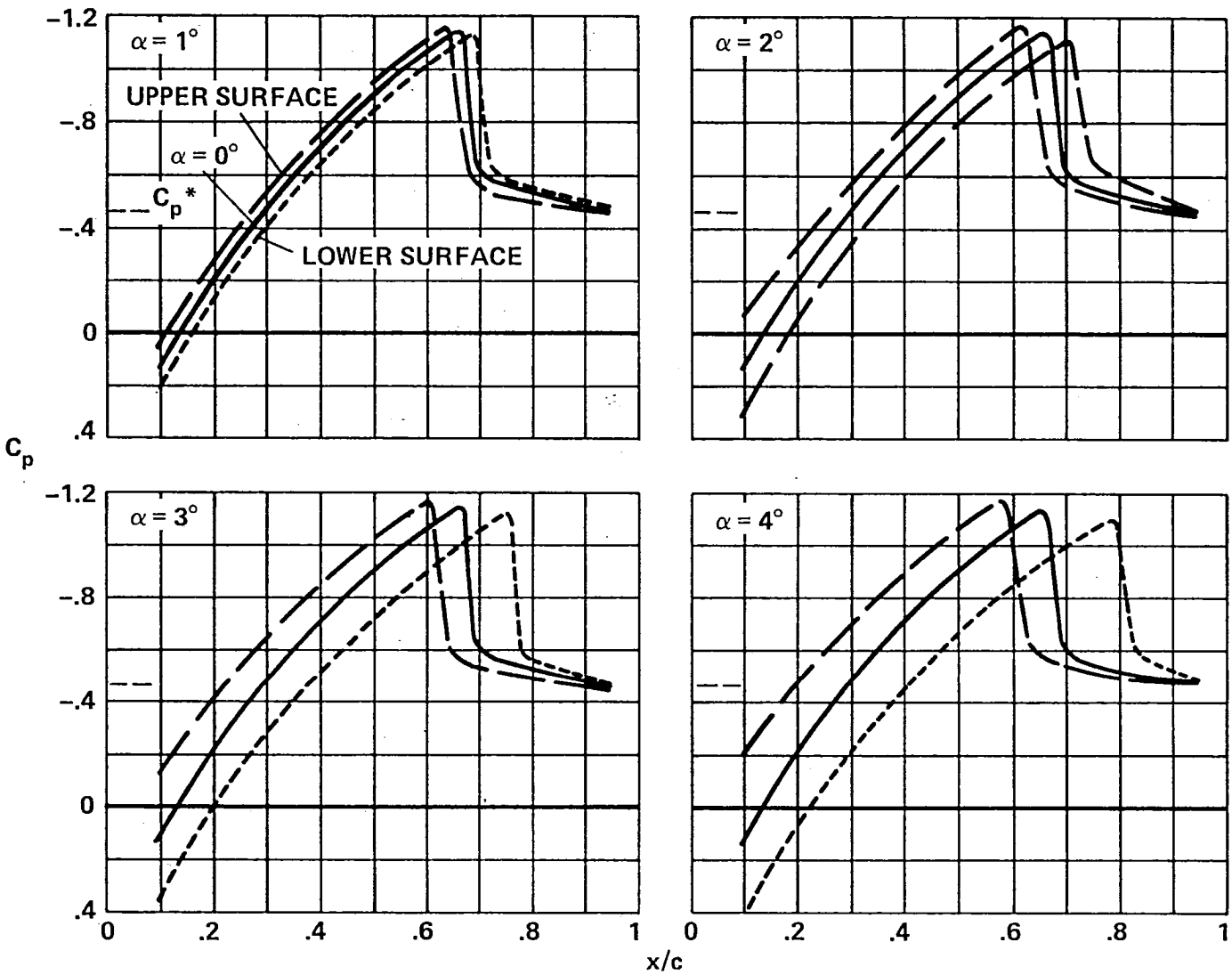

Figure 29.- Pressure distributions at angle of attack for steady flow with shock-induced separation; $M_\infty = 0.785$, $Re_{c,\infty} = 11 \times 10^6$.

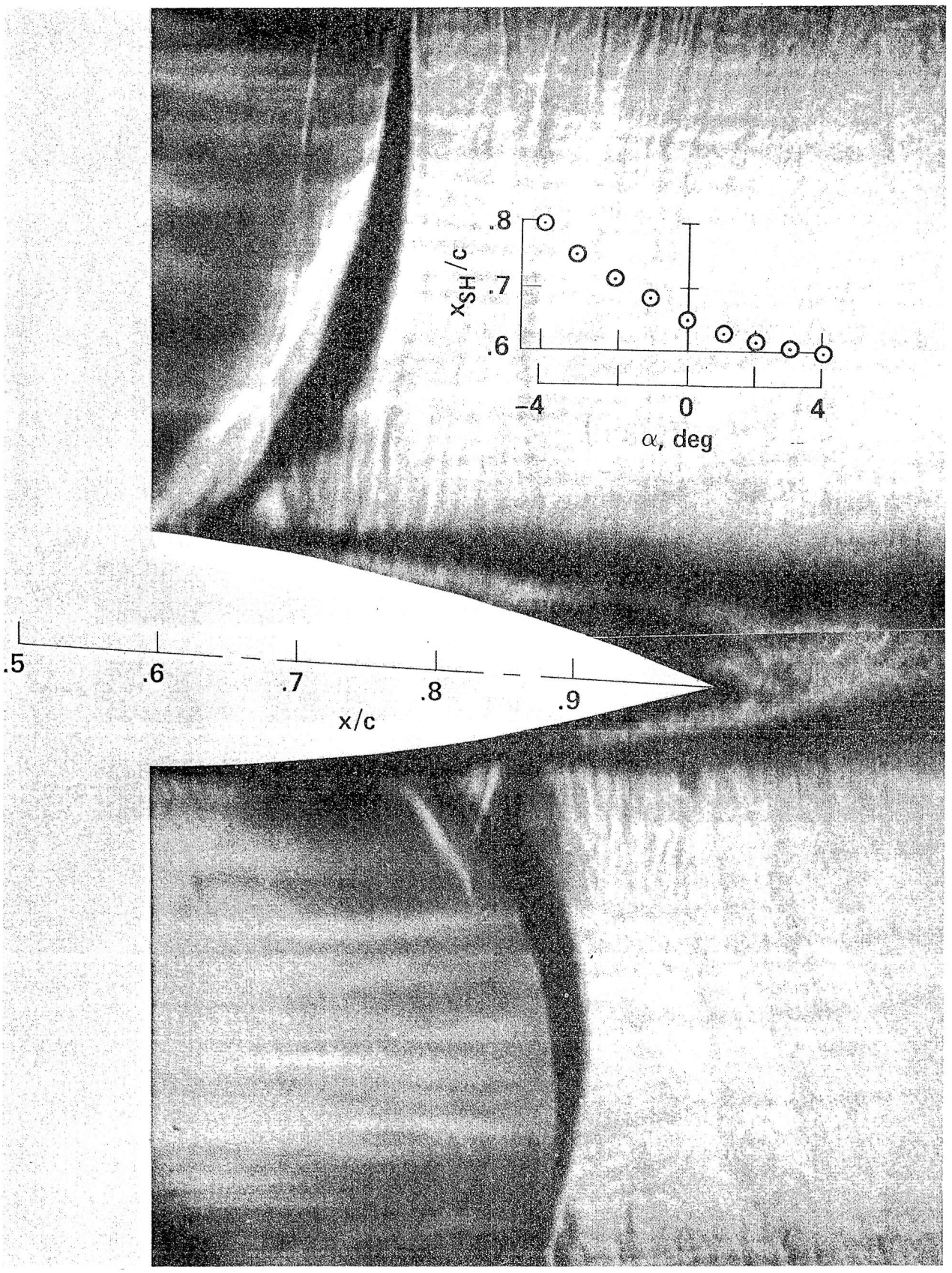

Figure 30.- Composite shadowgraph of flow field at $\alpha = 3°$ and variation of shock location with angle of attack; $M_\infty = 0.785$, $Re_{c,\infty} = 11 \times 10^6$.

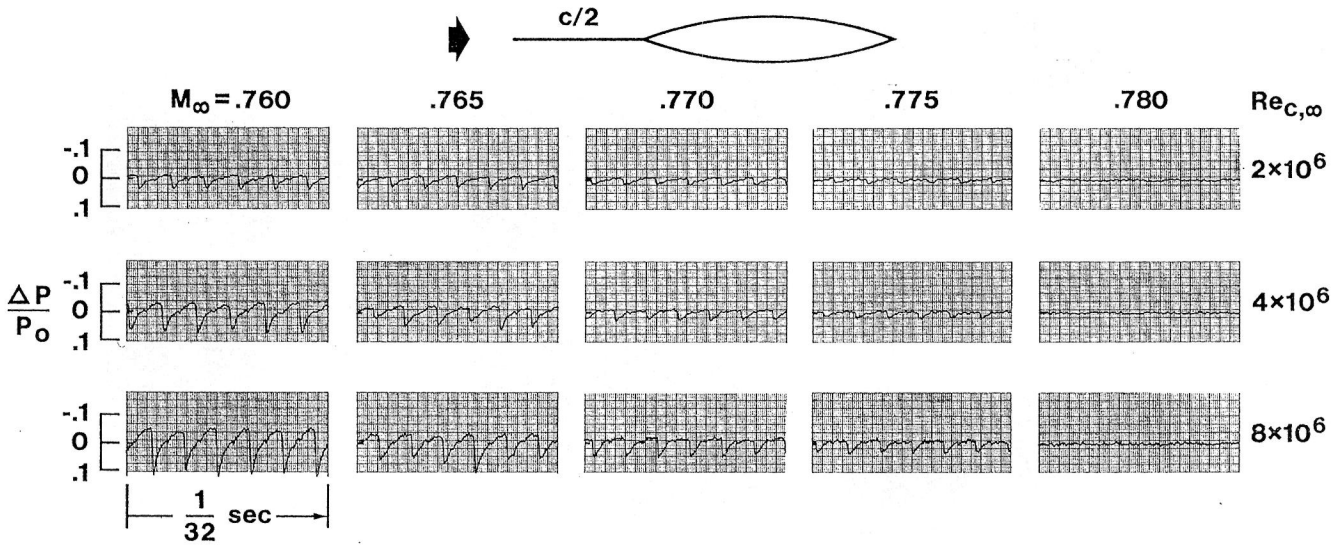

Figure 31.- Effect of leading-edge splitter plate on pressure fluctuations.

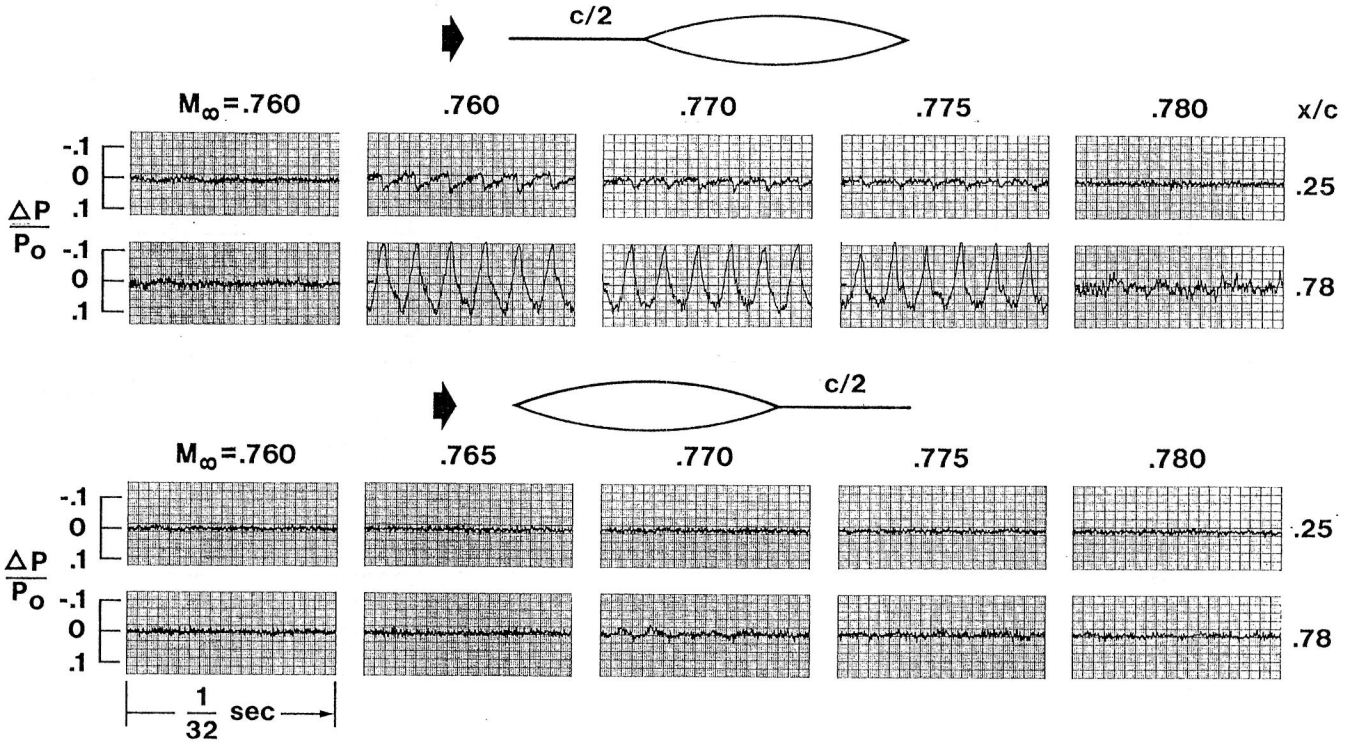

Figure 32.- Comparison of pressure-fluctuation measurements for leading-edge and trailing-edge splitter plates, $Re_{c,\infty} = 8\times10^6$.

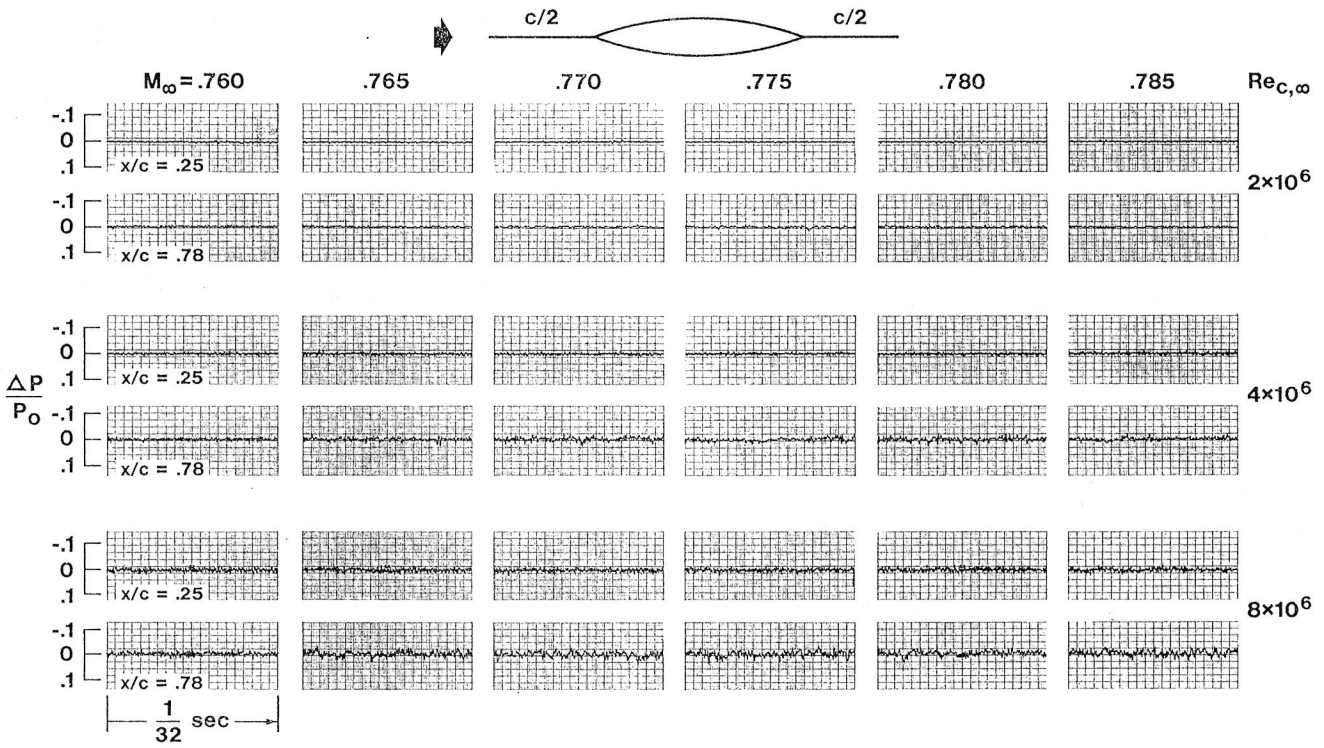

Figure 33.- Pressure-fluctuation measurements with both leading-edge and trailing-edge splitter plates.

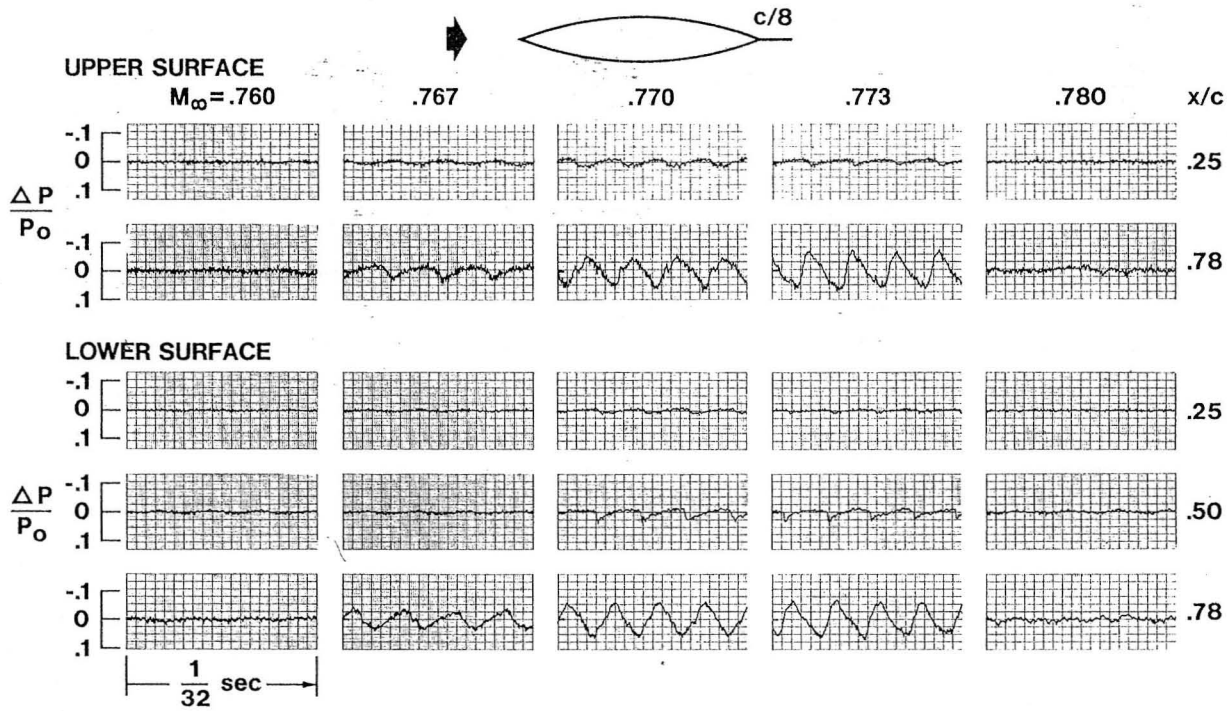

Figure 34.- Pressure-fluctuation measurements with trailing-edge plate of length c/8, $Re_{c,\infty} = 8\times10^6$.

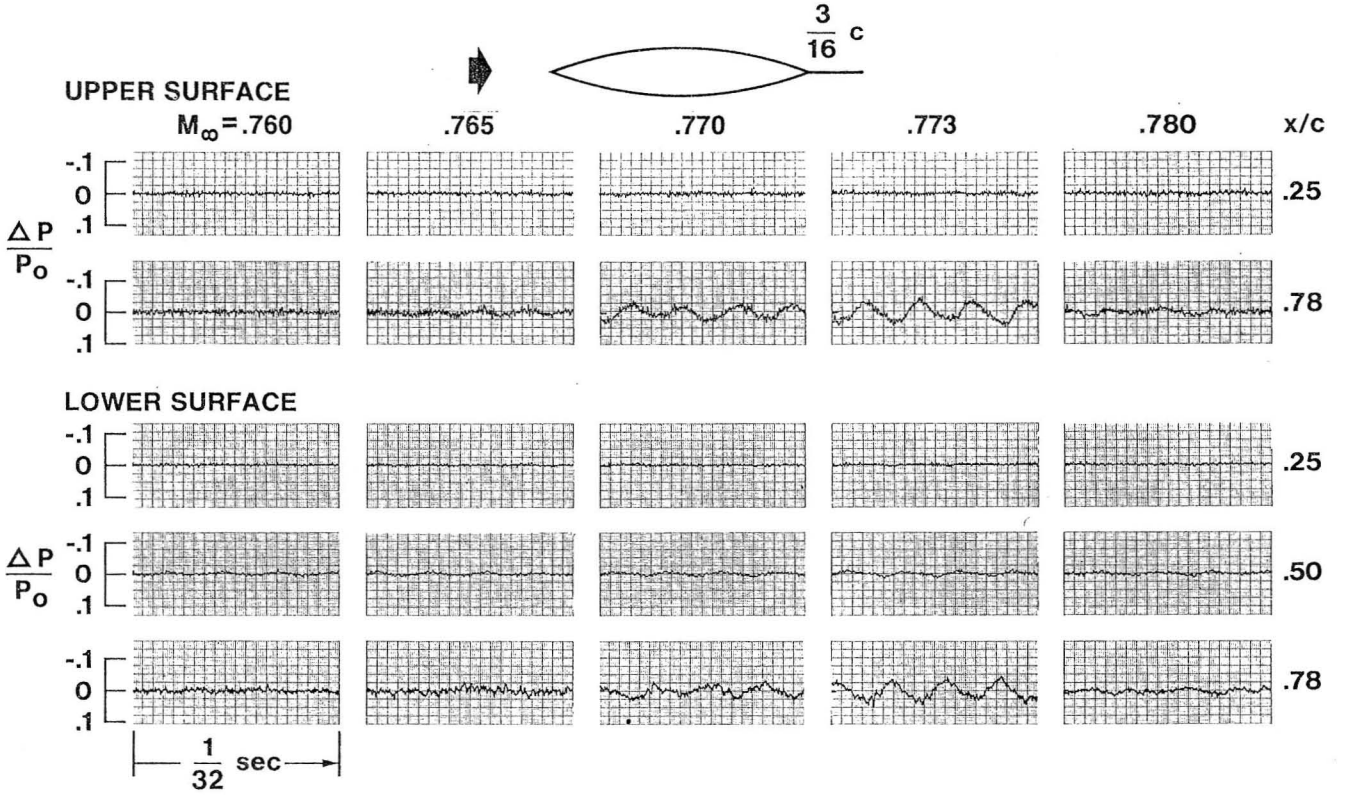

Figure 35.- Pressure fluctuations with trailing-edge plate of length 3/16c, $Re_{c,\infty} = 8 \times 10^6$.

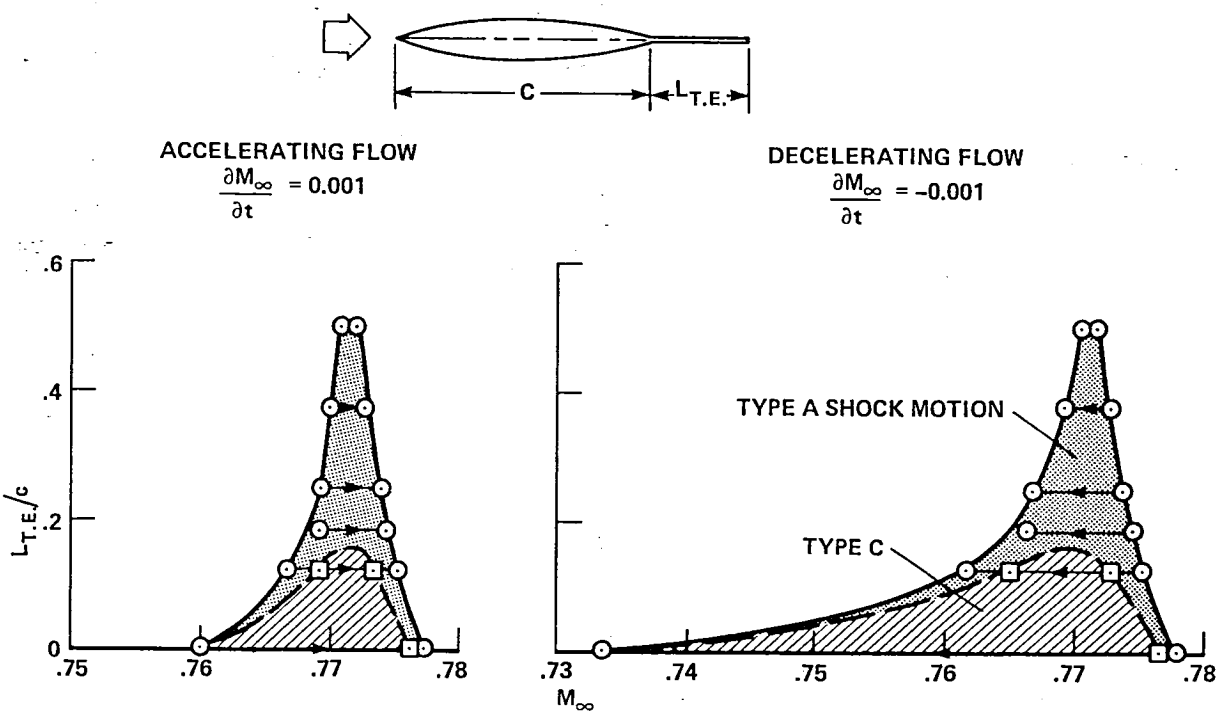

Figure 36.- Unsteady flow domains with trailing-edge splitter plates, $Re_{c,\infty} = 8 \times 10^6$.

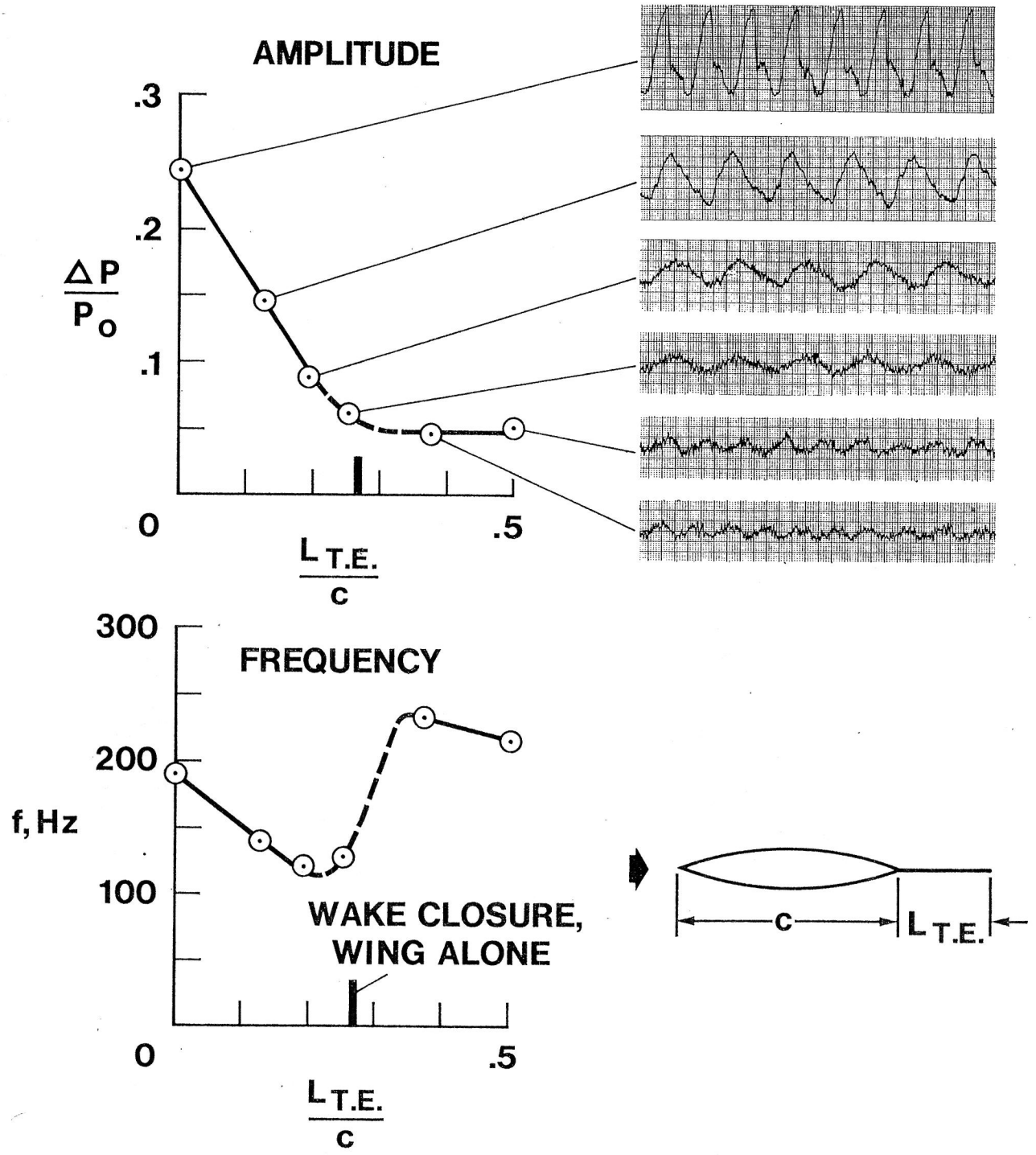

Figure 37.- Effect of trailing-edge splitter plates on amplitude and frequency of pressure fluctuations at $x/c = 0.78$; $M_\infty = 0.772$, $Re_{c,\infty} = 8\times10^6$.

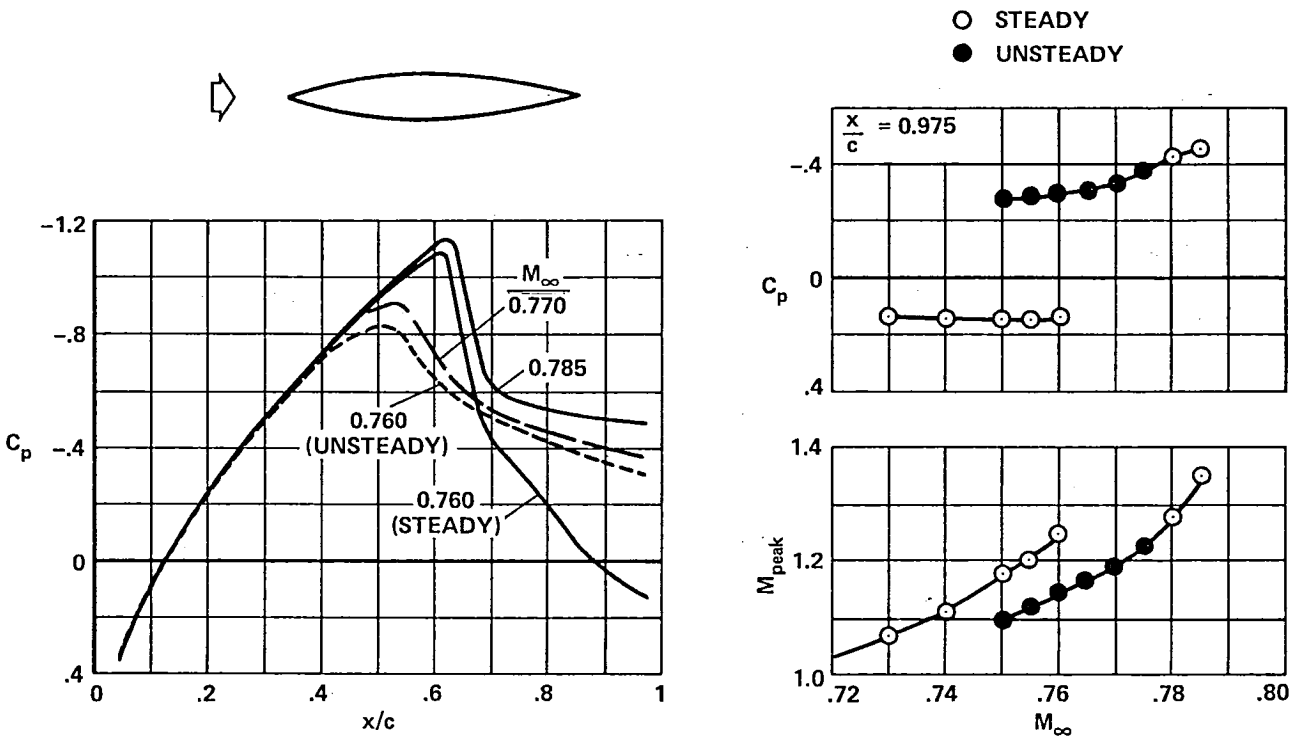

(a) Wing alone.

Figure 38.- Mean pressure distributions with various splitter plates, $Re_{c,\infty} = 8 \times 10^6$.

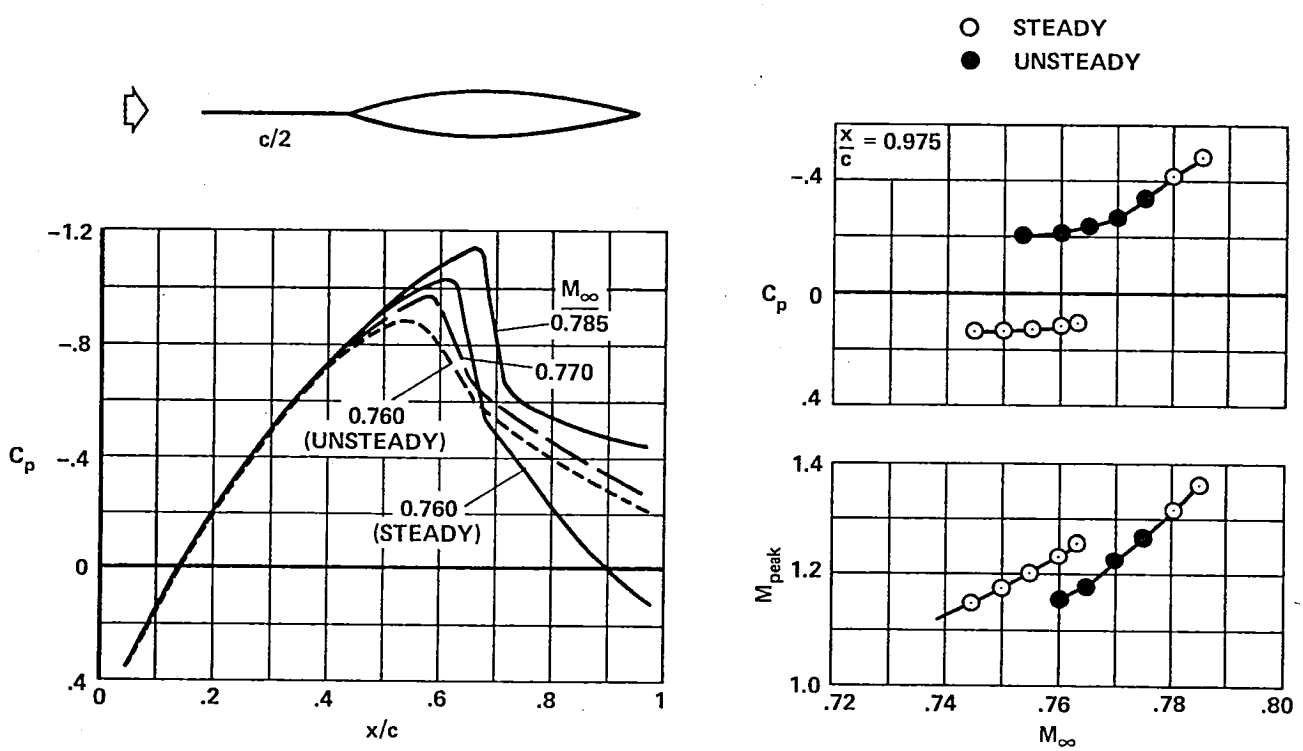

(b) Leading-edge plate.

Figure 38.- Continued.

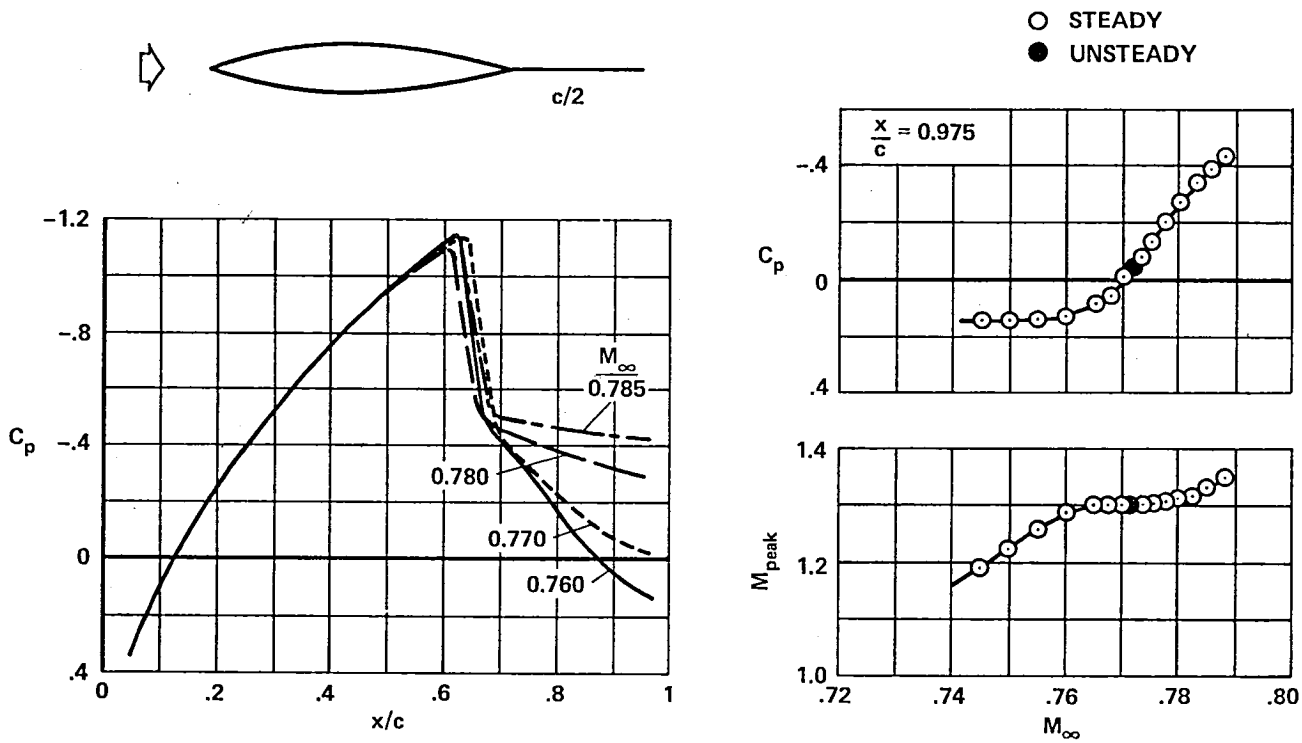

(c) Trailing-edge plate.

Figure 38.- Continued.

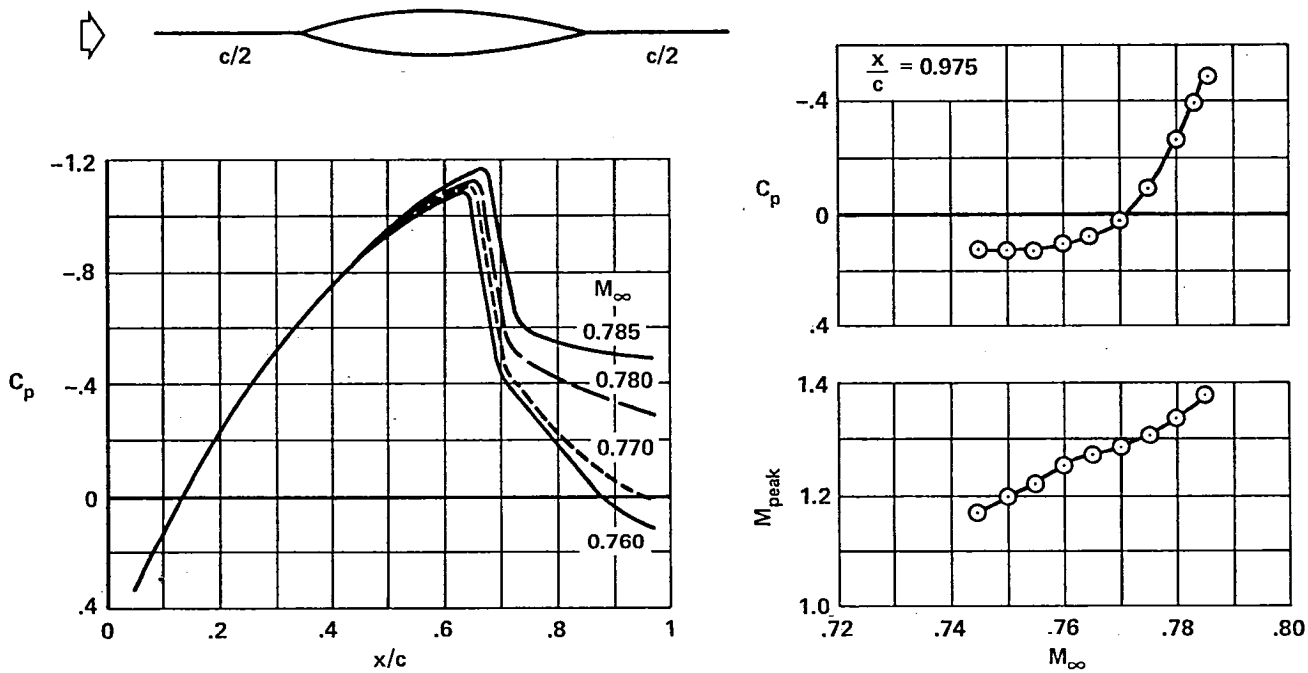

(d) Leading-edge and trailing-edge plates.

Figure 38.- Continued.

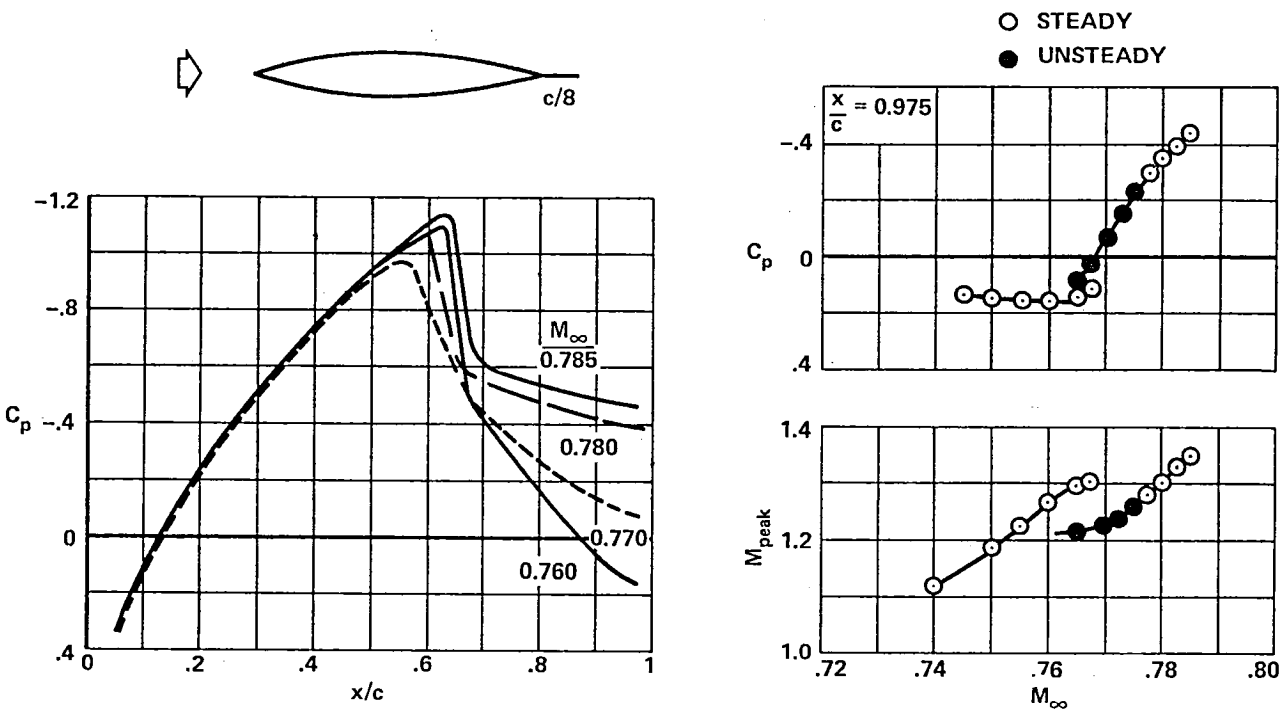

(e) Short trailing-edge plate.

Figure 38.- Concluded.

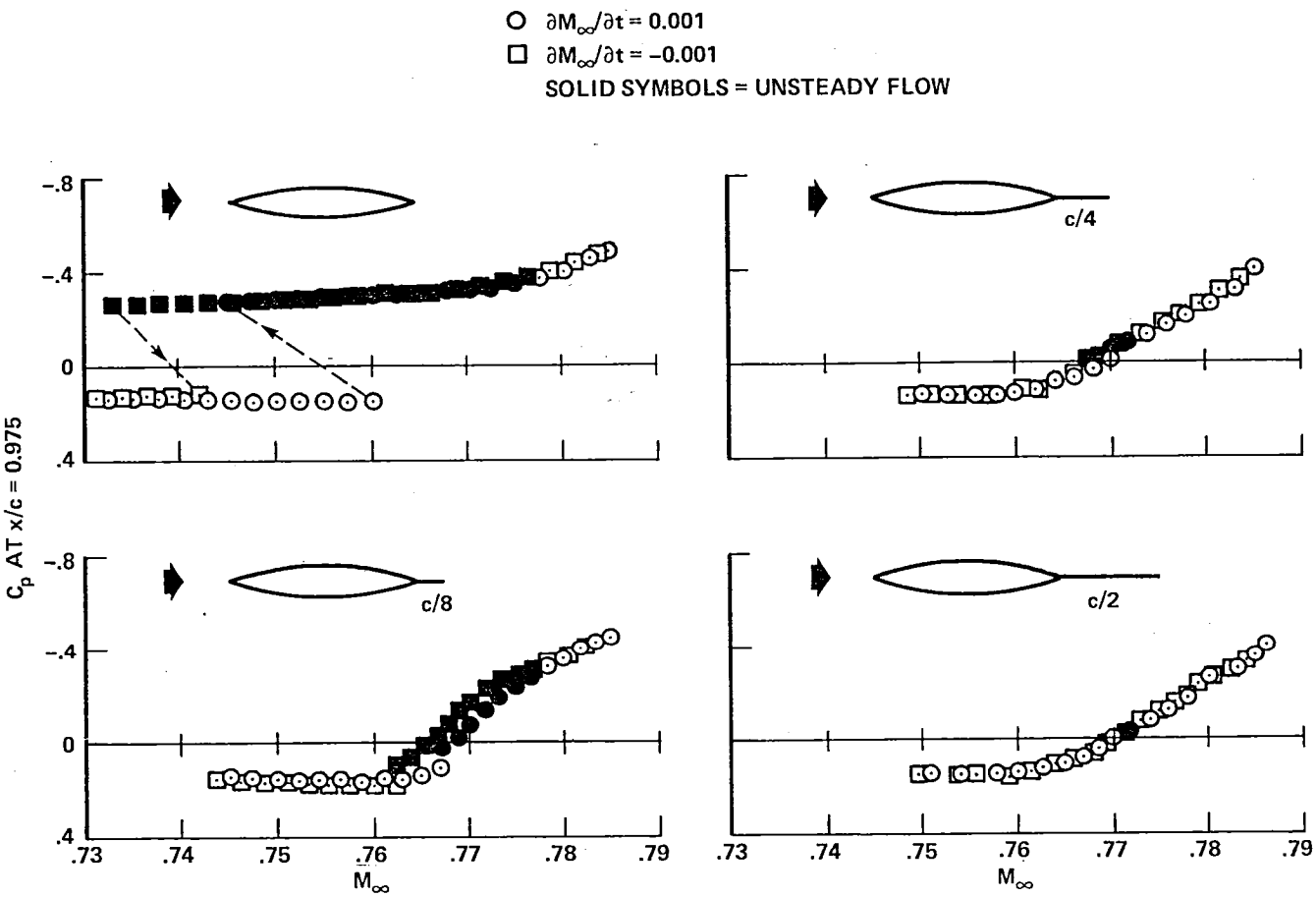

Figure 39.- Variation of airfoil pressure coefficient at x/c = 0.975 with Mach number for various splitter plates.

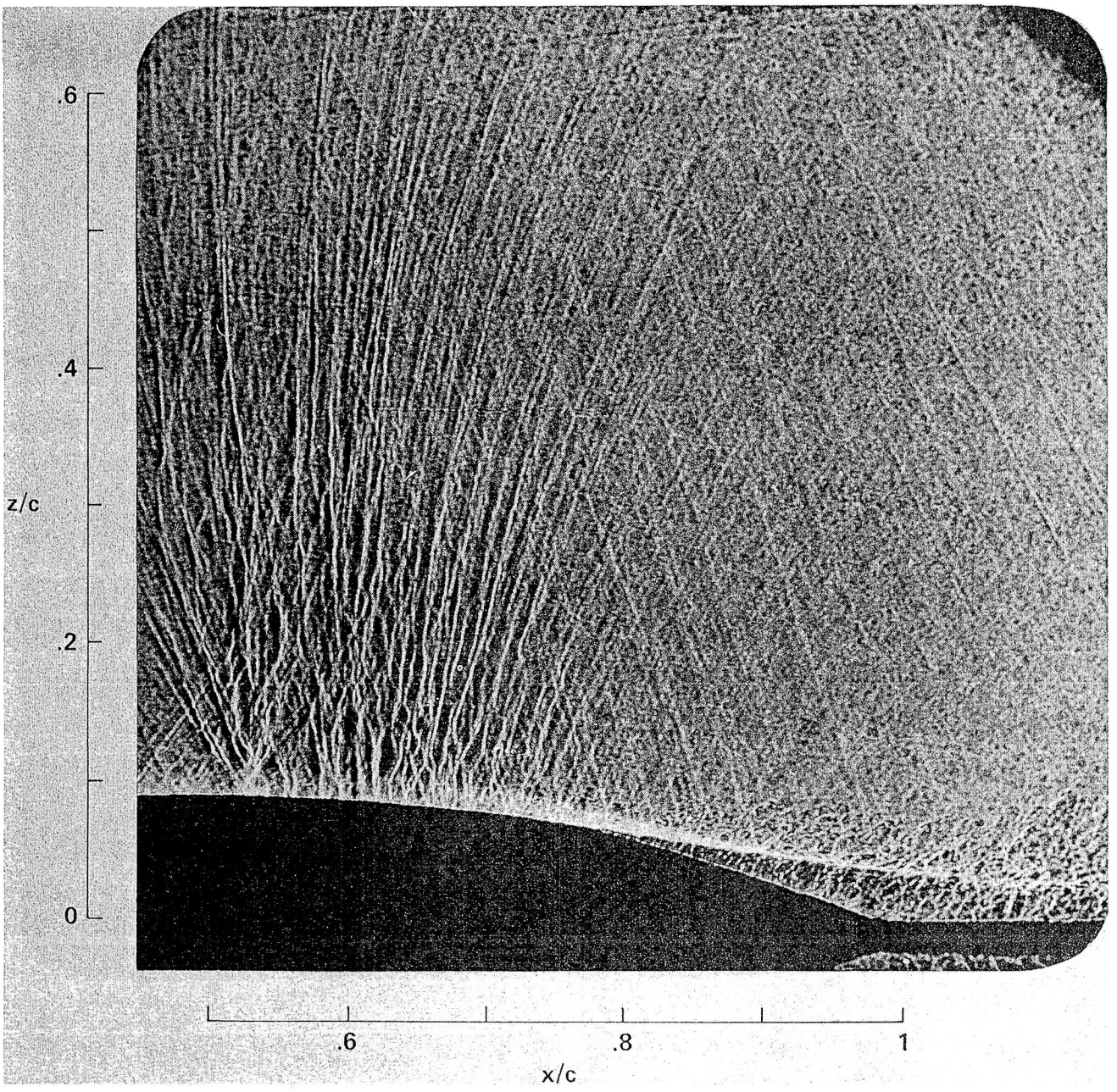

(a) $M_\infty = 0.750$.

Figure 40.- Flow-field shadowgraphs of airfoil with trailing-edge plate of length c/2; $Re_{c,\infty} = 11 \times 10^6$.

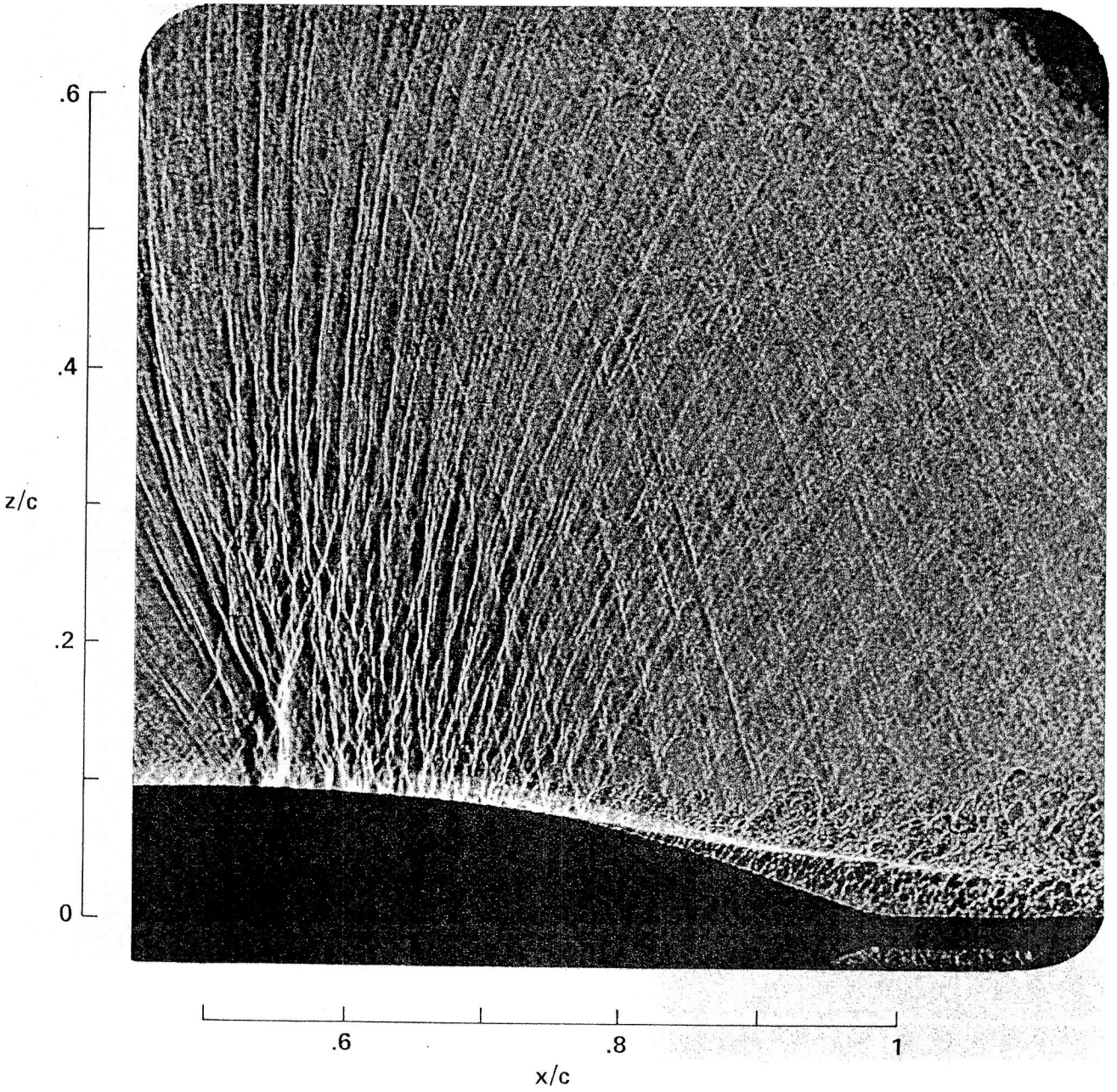

(b) $M_\infty = 0.755$.

Figure 40.- Continued.

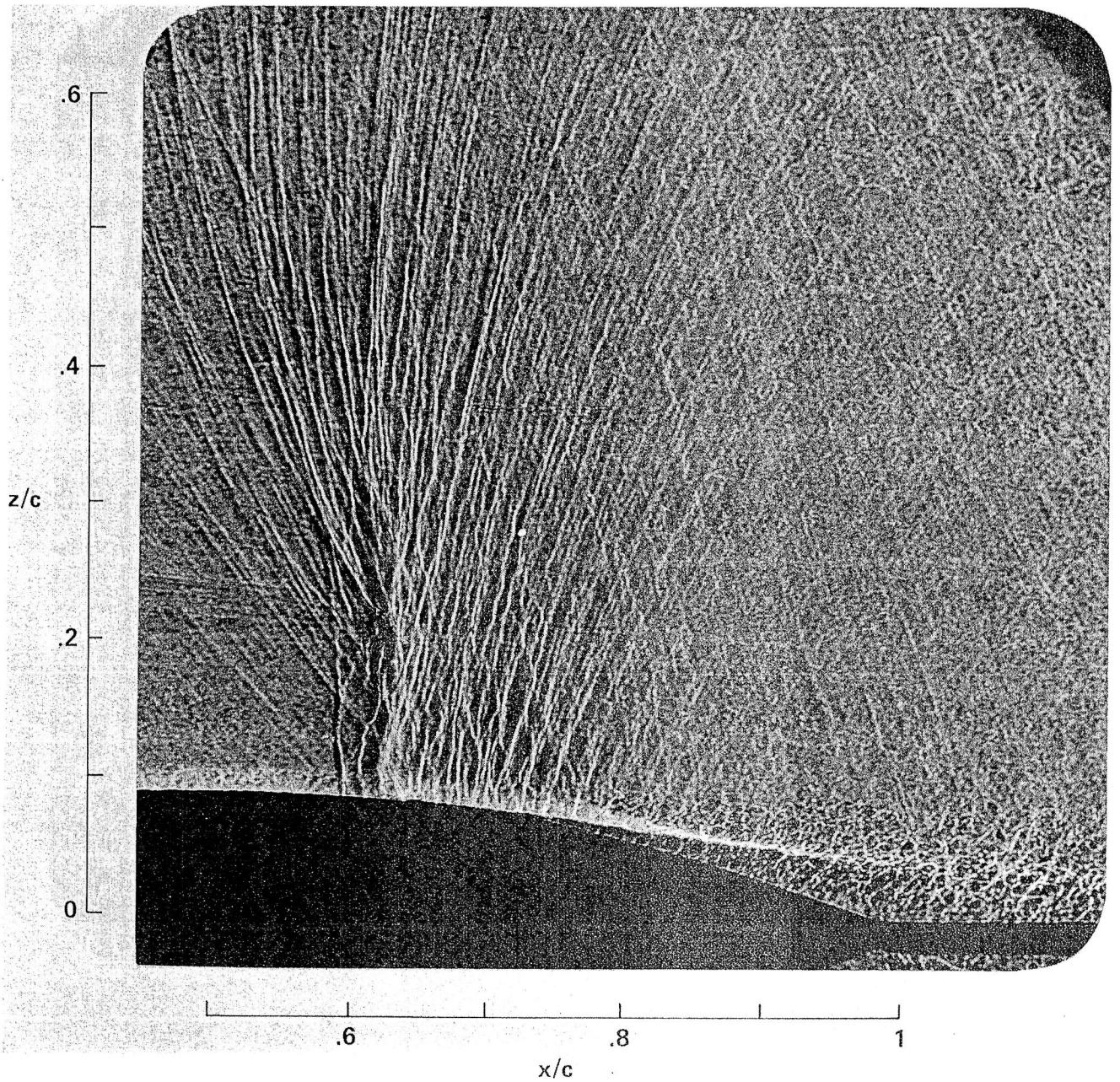

(c) $M_\infty = 0.765$.

Figure 40.- Continued.

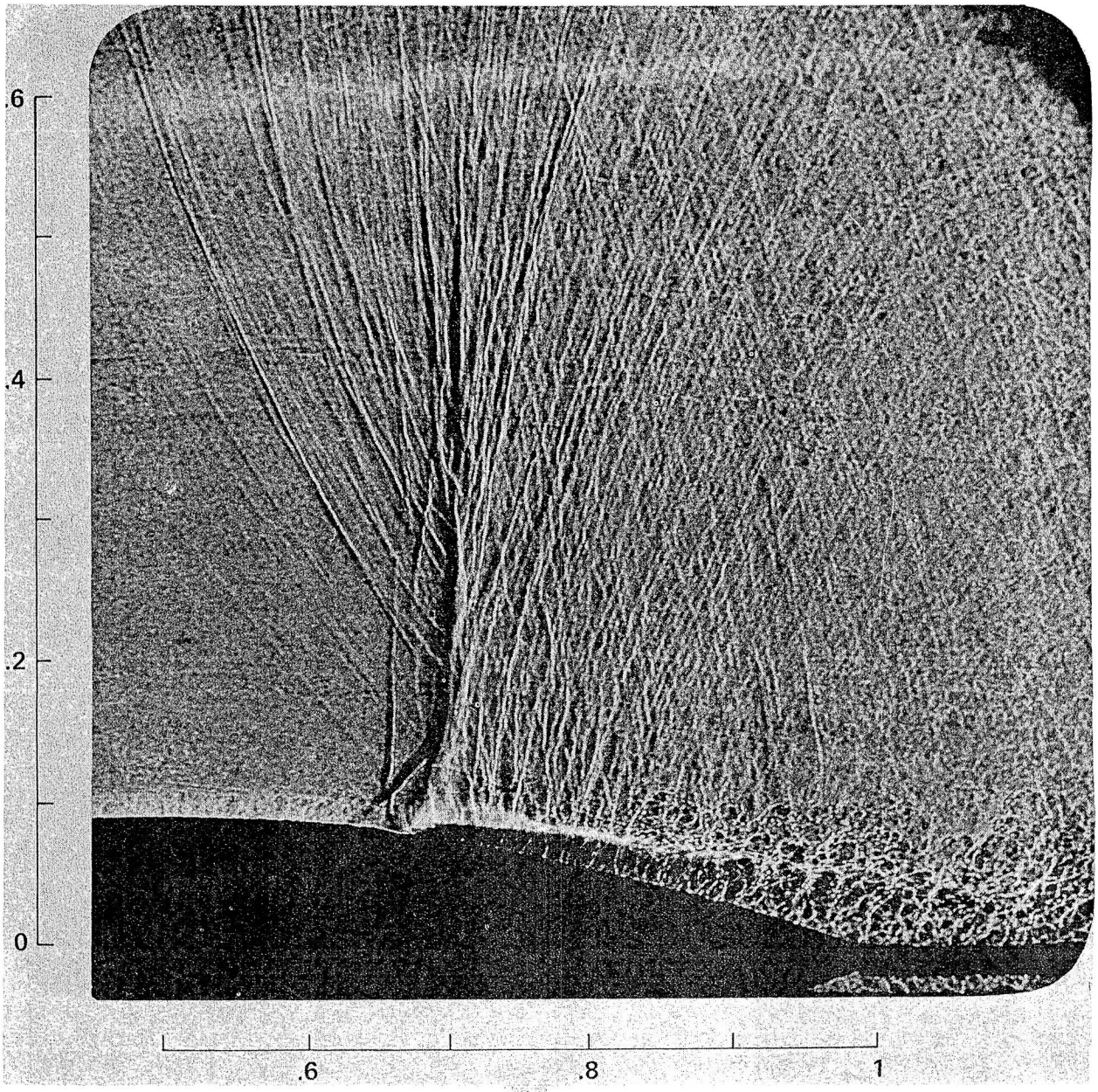

(d) $M_\infty = 0.775$.

Figure 40.- Continued.

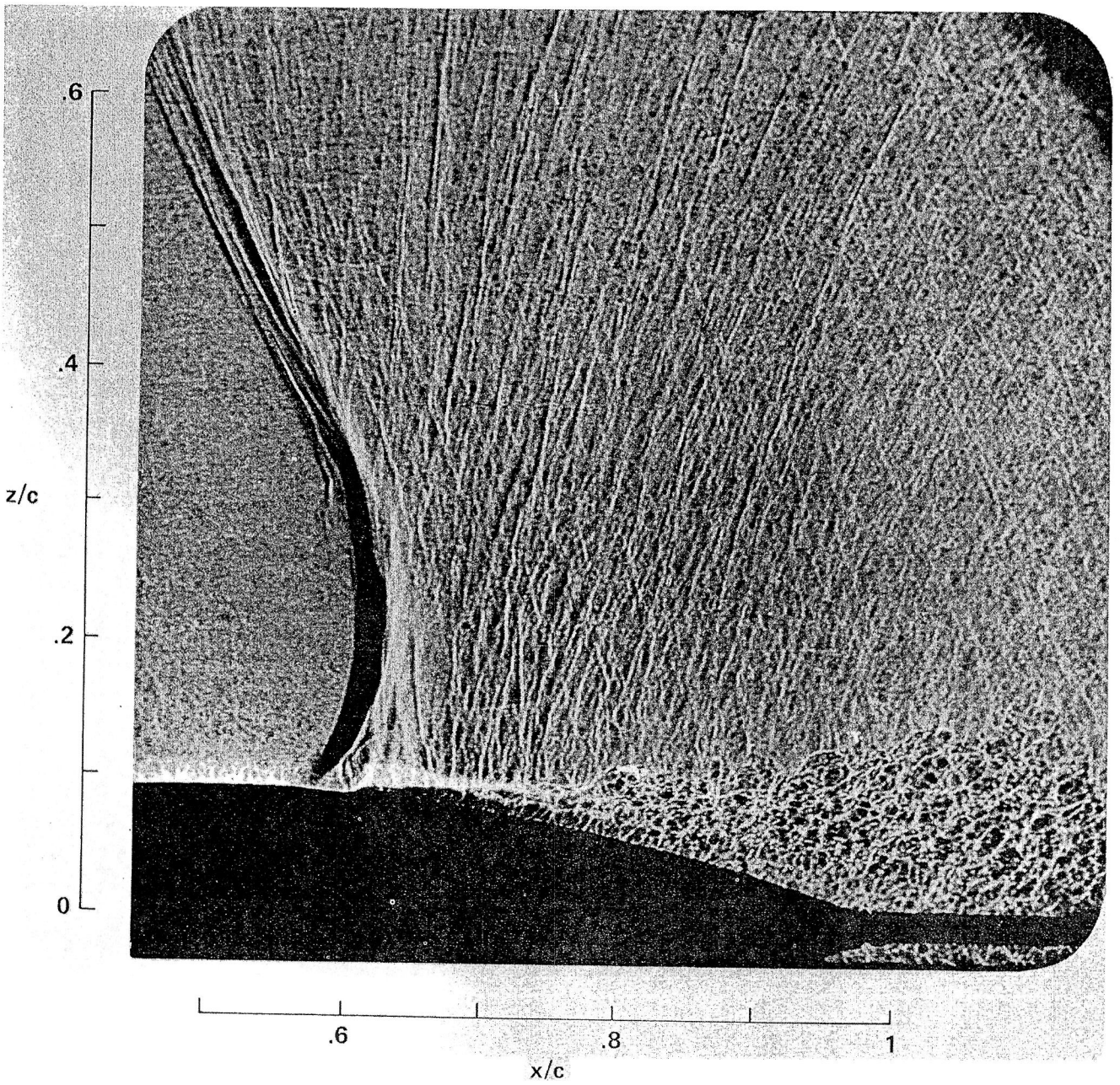

(e) $M_\infty = 0.780$.

Figure 40.- Continued.

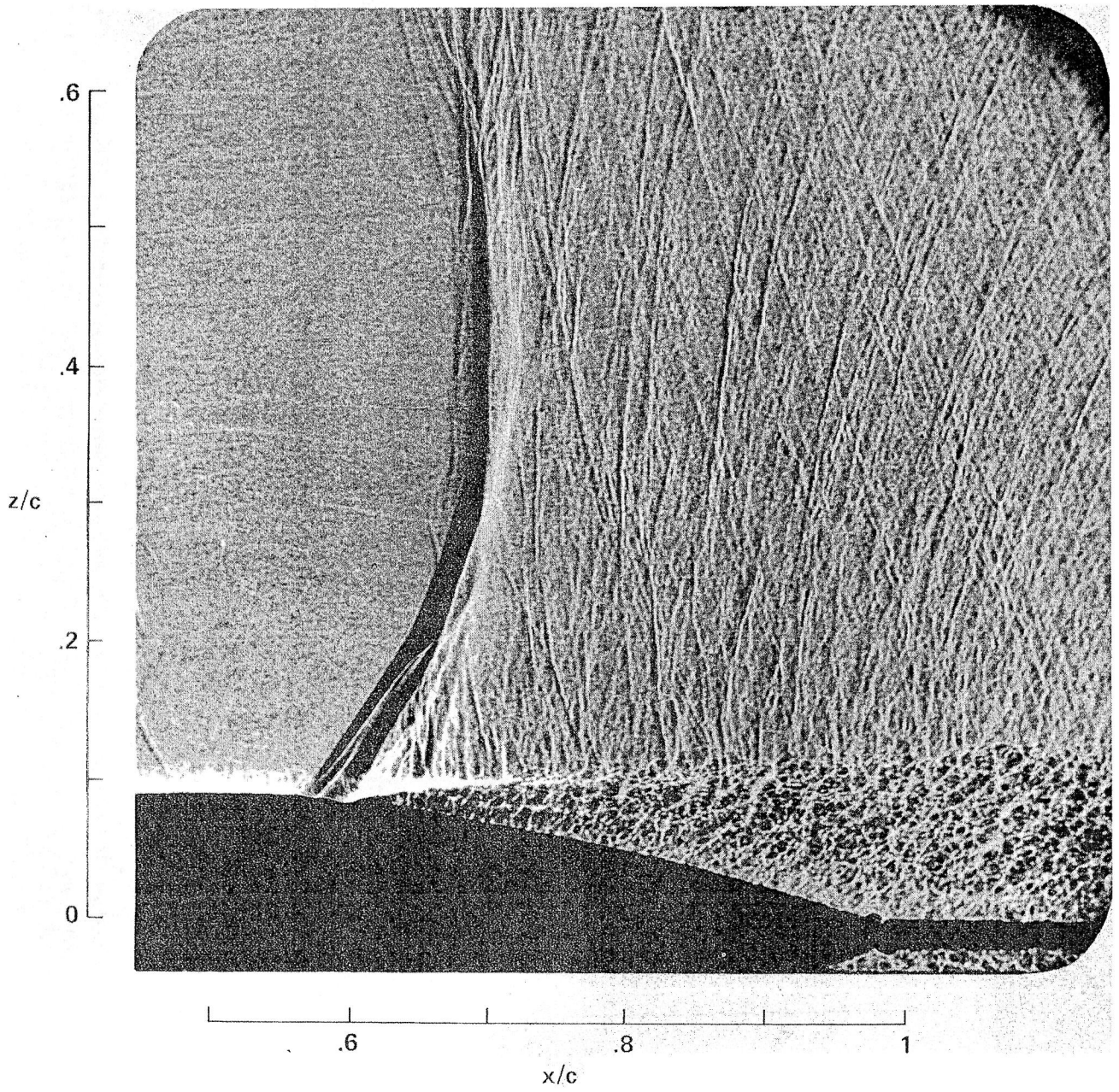

(f) $M_\infty = 0.785$.

Figure 40.- Concluded.

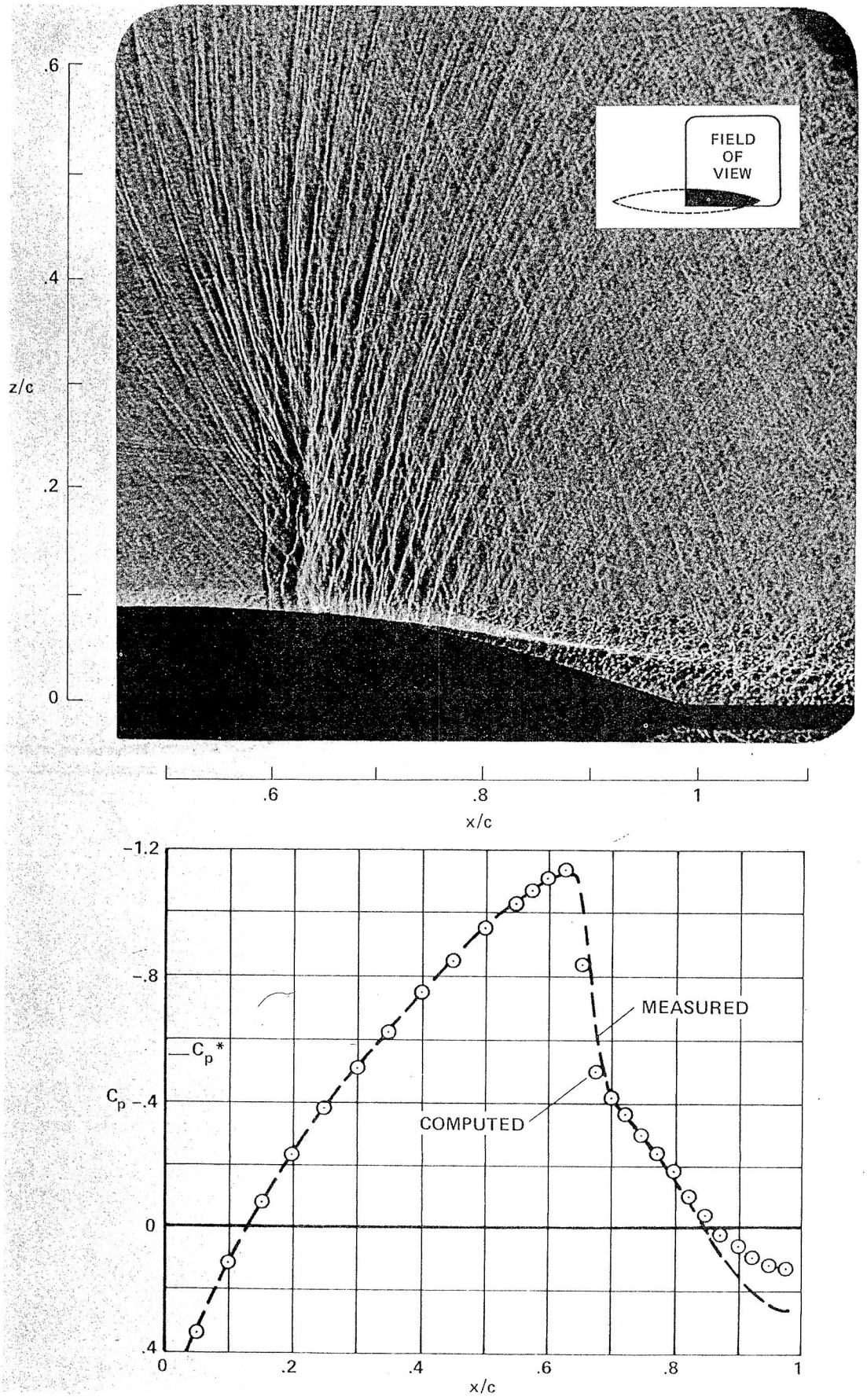

Figure 41.- Comparison of computation and experiment for airfoil with trailing-edge plate; $M_\infty = 0.76$, $Re_{c,\infty} = 10^7$.

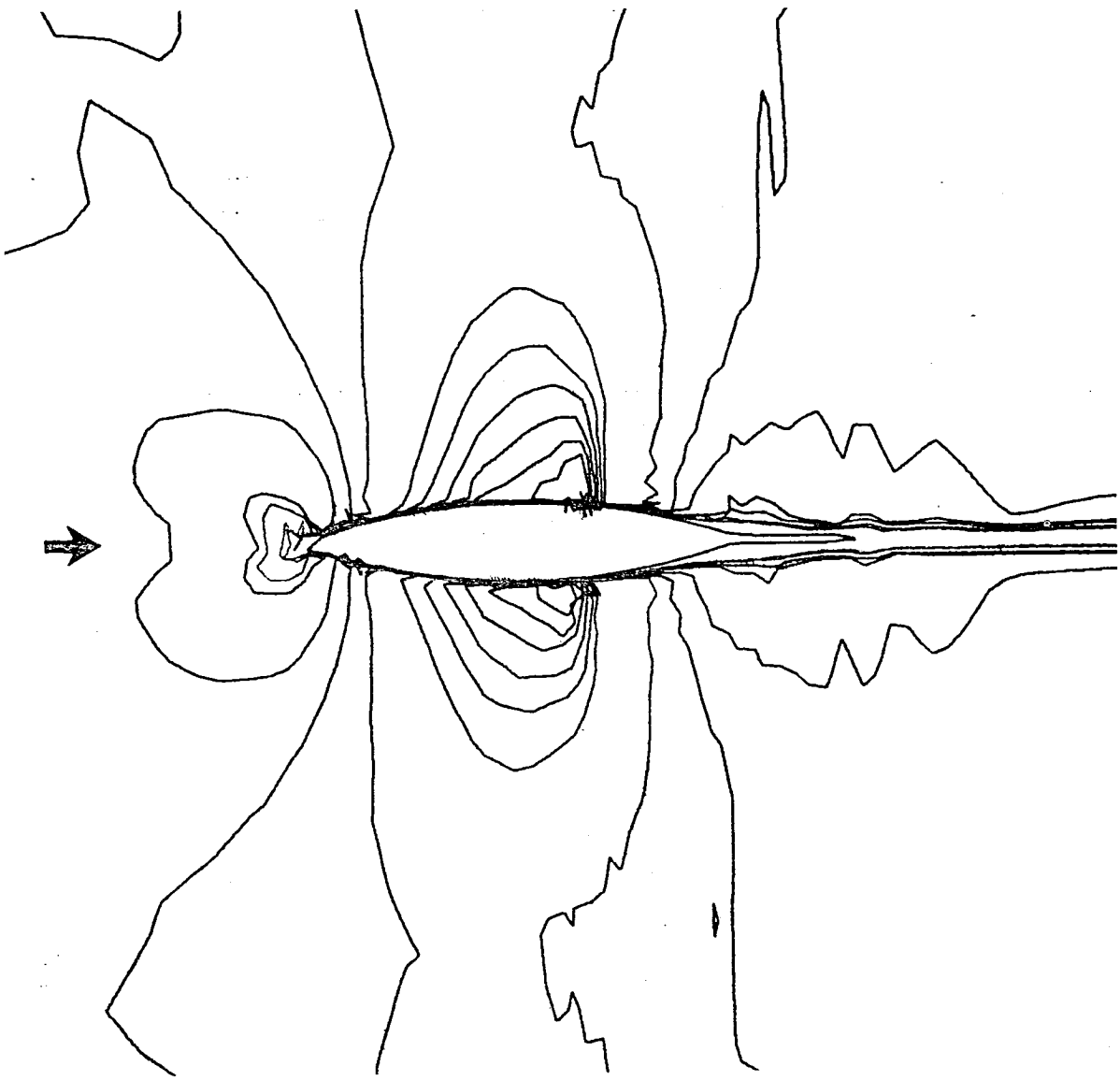

Figure 42.- Computed Mach contours; $M_\infty = 0.76$, $Re_{c,\infty} = 10^7$.

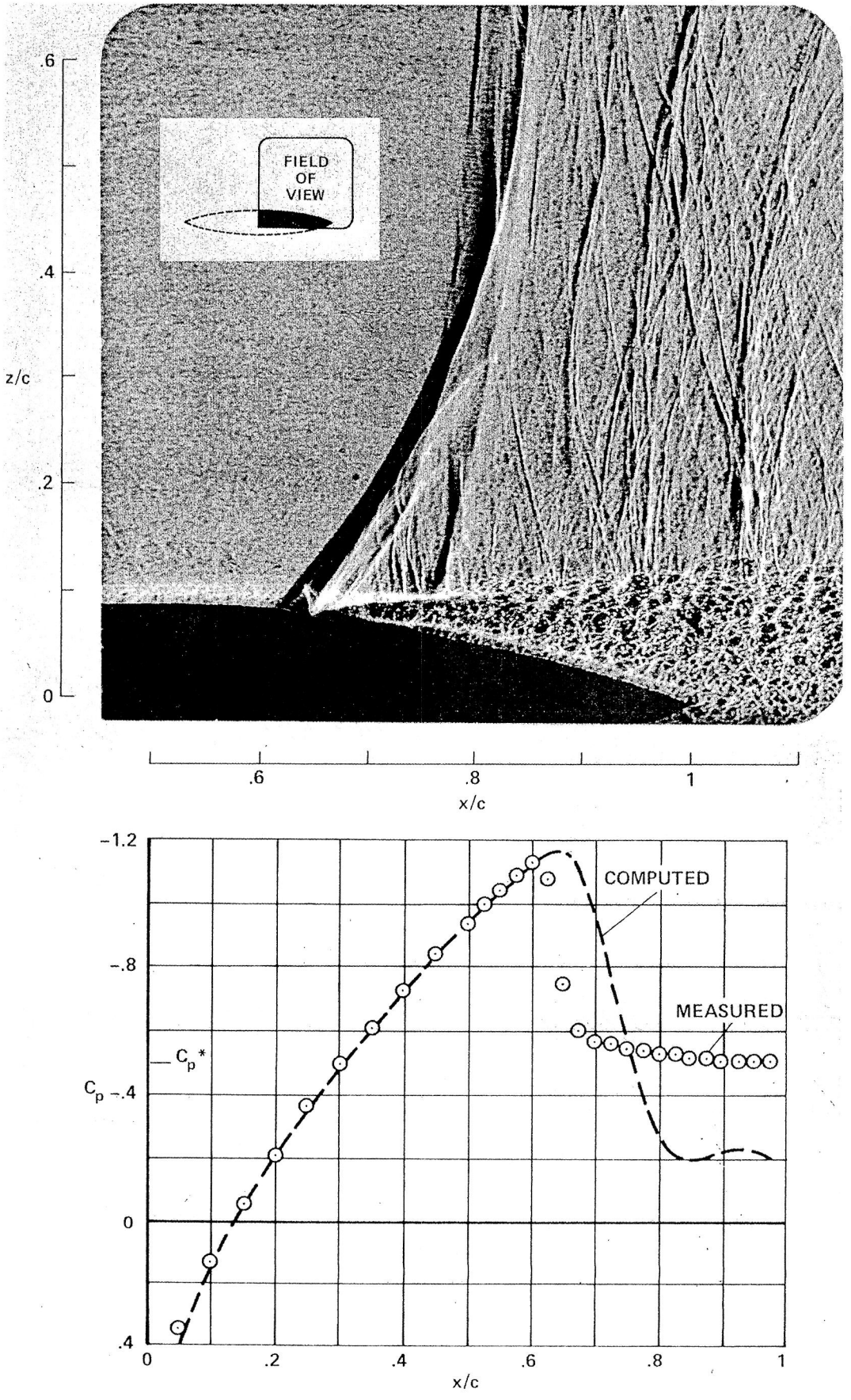

Figure 43.- Comparison of computation and experiment; $M_\infty = 0.78$, $Re_{c,\infty} = 10^7$.

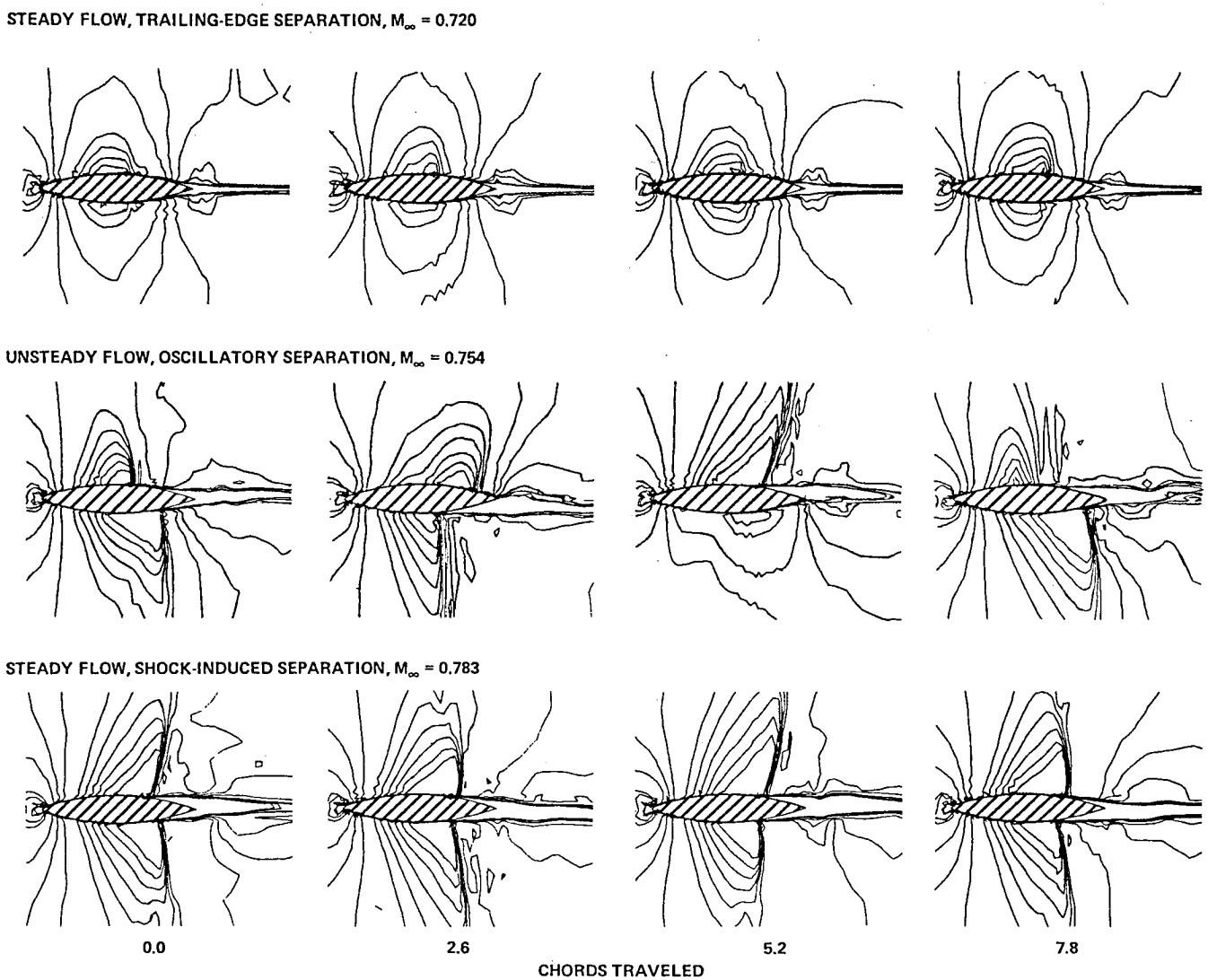

Figure 44.- Computed Mach contours; M_∞ = 0.72, 0.75, and 0.78, $Re_{c,\infty} = 10^7$ (from ref. 6).

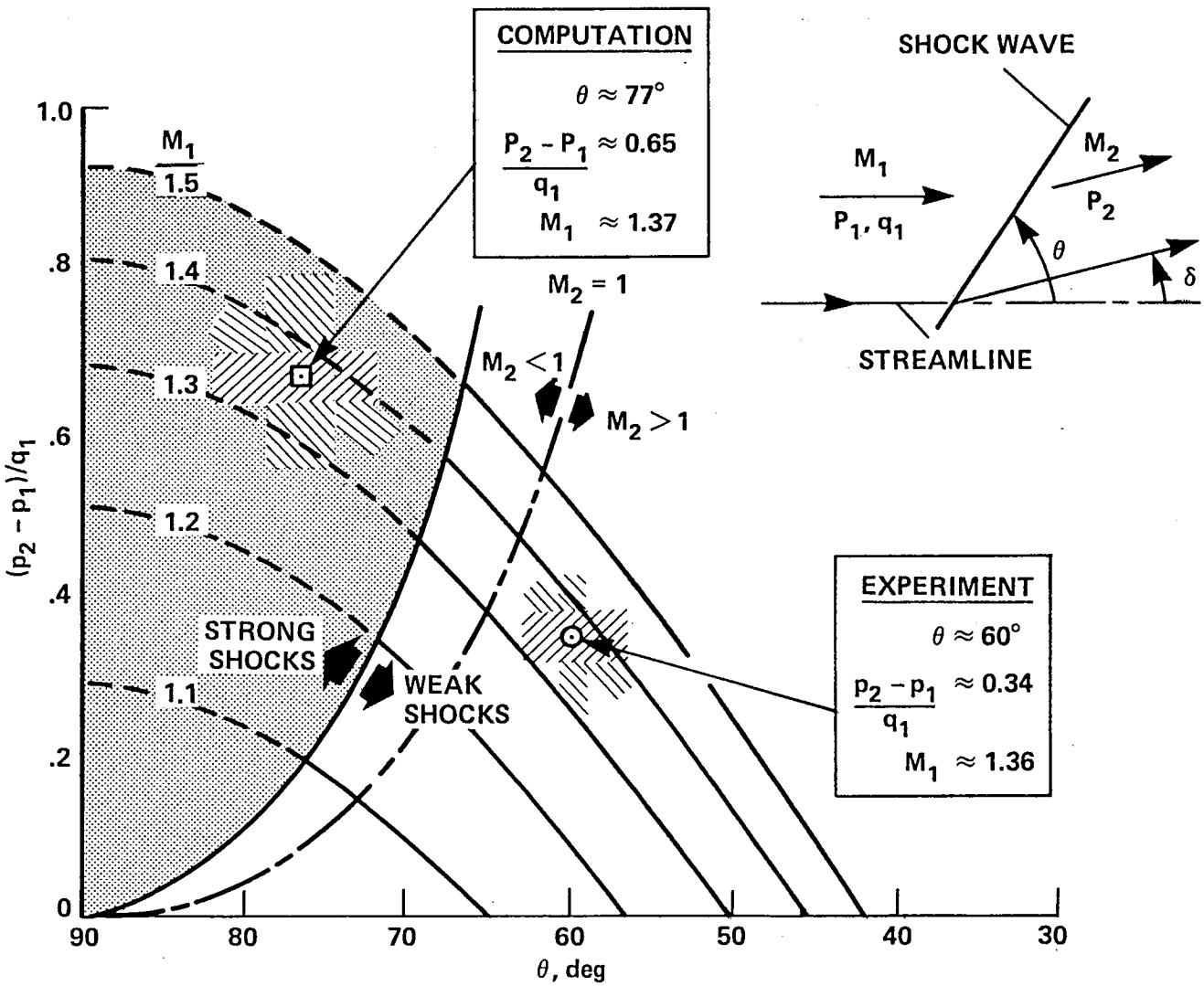

Figure 45.- Oblique shock solutions, $(p_2 - p_1)/q_1$ vs θ for given M_1, and overlays of computed and experimental values for $M_\infty = 0.785$ and $Re_{c,\infty} = 11 \times 10^6$.

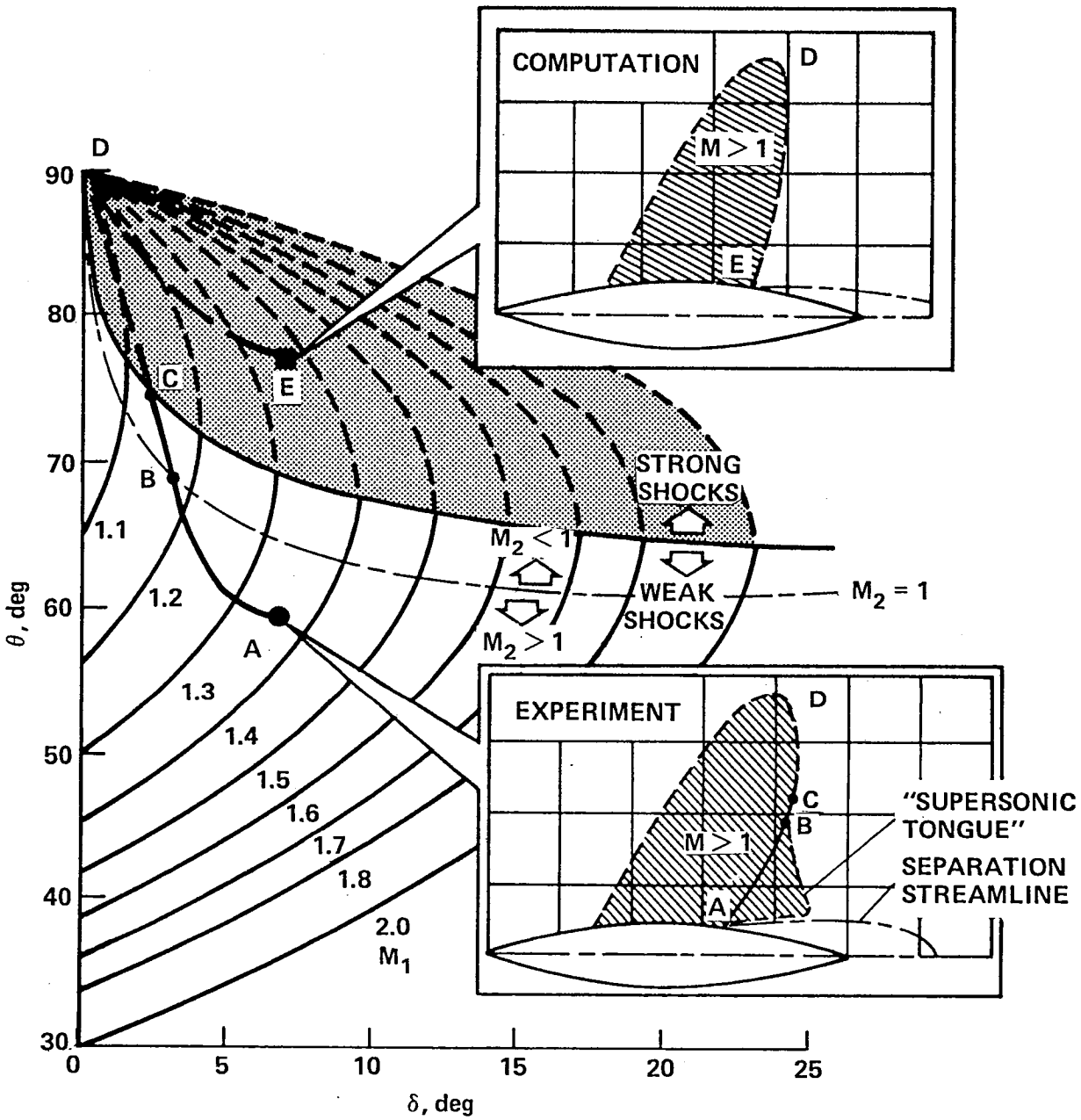

Figure 46.- Oblique shock solutions, θ vs δ for given M_1, and overlays of computed and measured values for $M_\infty = 0.785$ and $Re_{c,\infty} = 11 \times 10^6$.

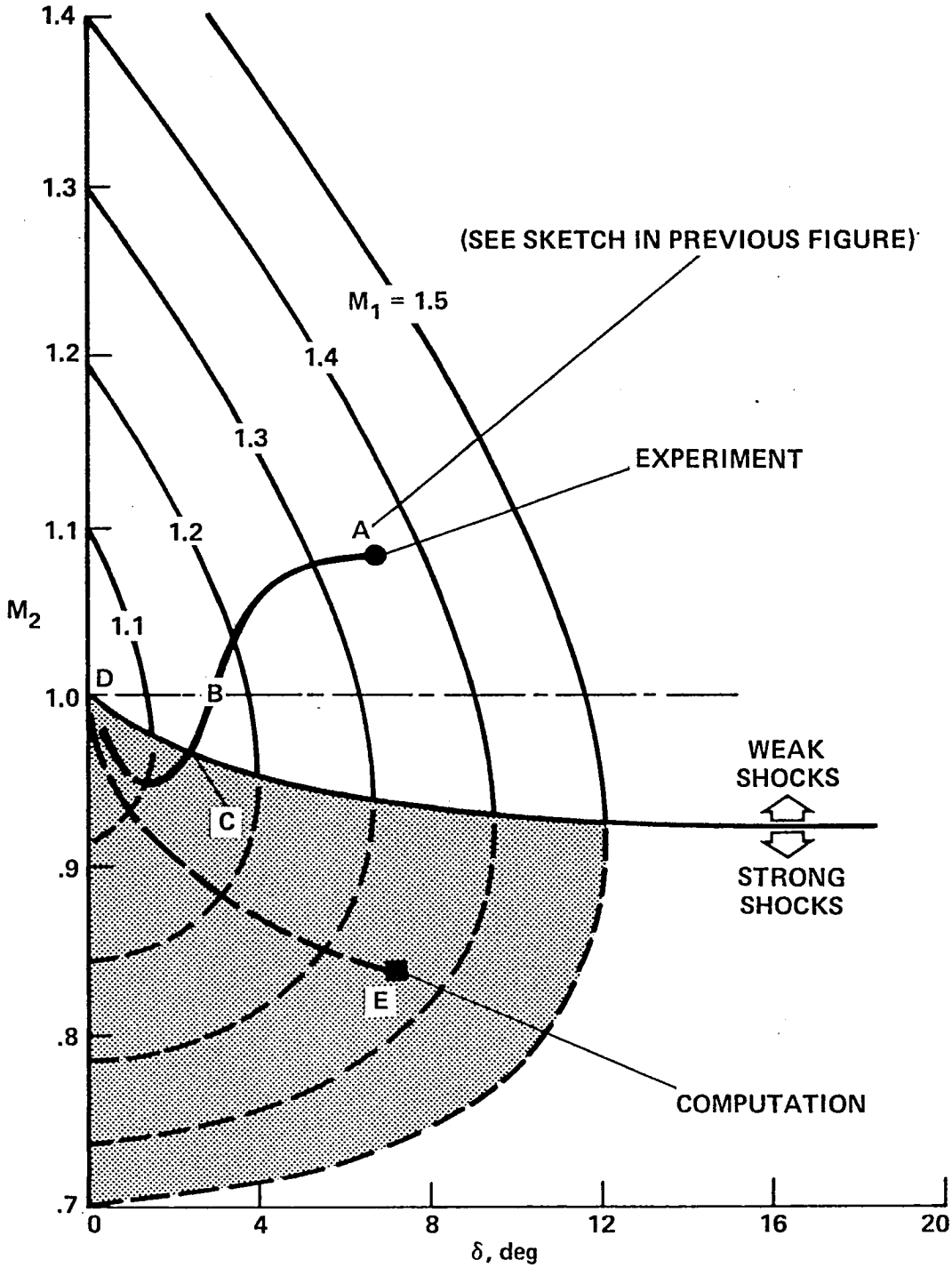

Figure 47.- Oblique shock solutions, M_2 vs δ for given M_1 and comparison of computation with experiment, $M_\infty = 0.785$ and $Re_{c,\infty} = 11 \times 10^6$.

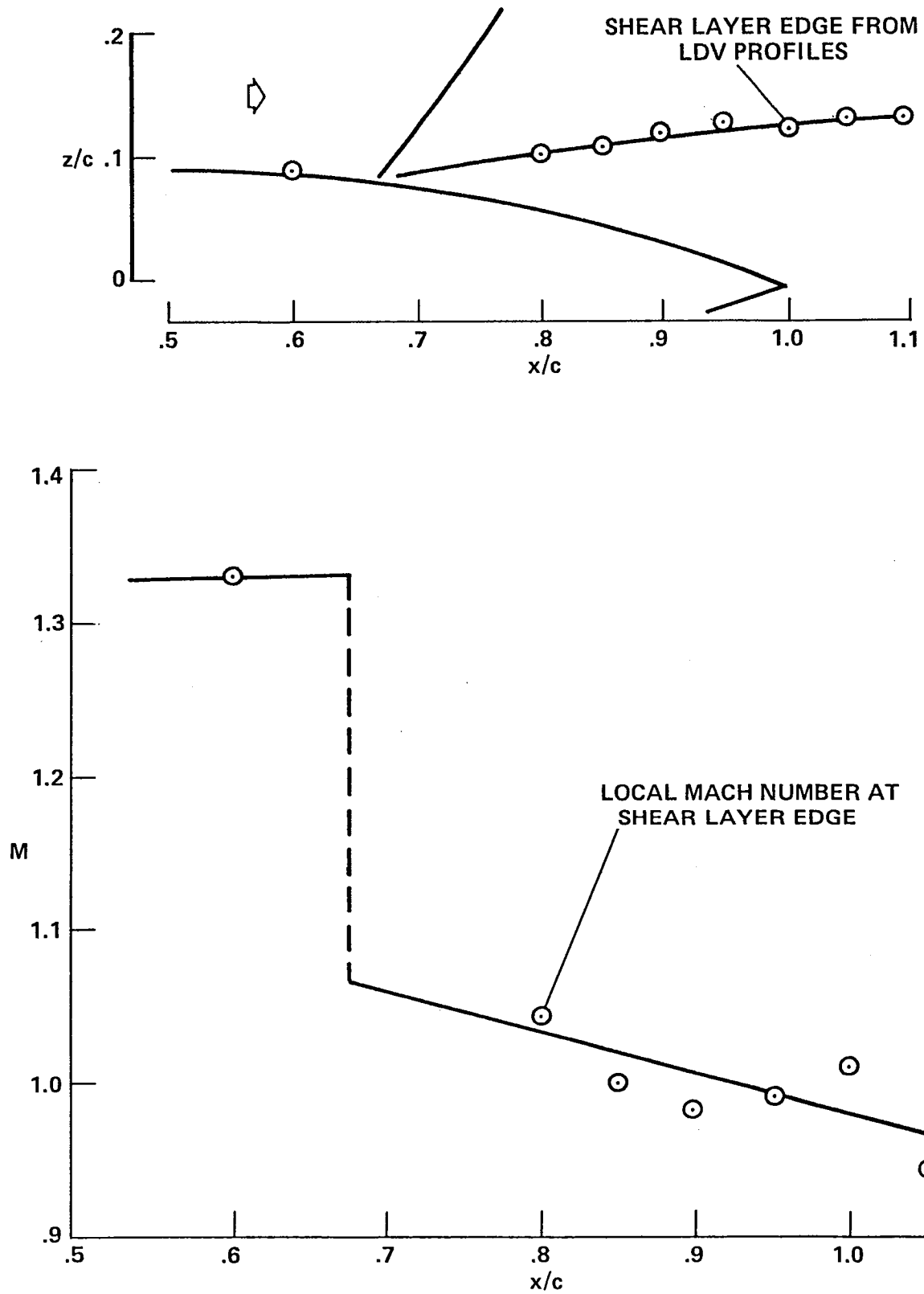

Figure 48.- Shear-layer edge and local Mach numbers (from ref. 8).

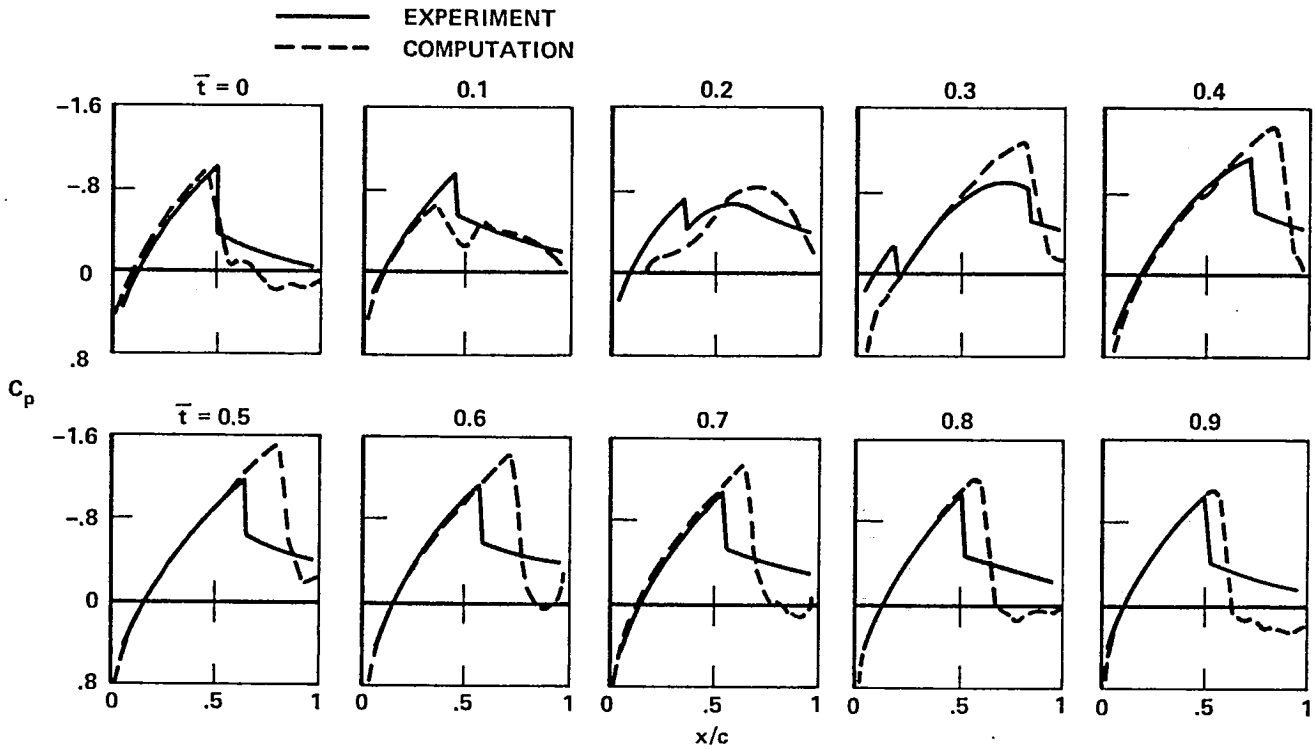

Figure 49.- Comparisons of numerical solutions with experiment for unsteady flow; $M_\infty = 0.76$, $Re_{c,\infty} = 11 \times 10^6$.

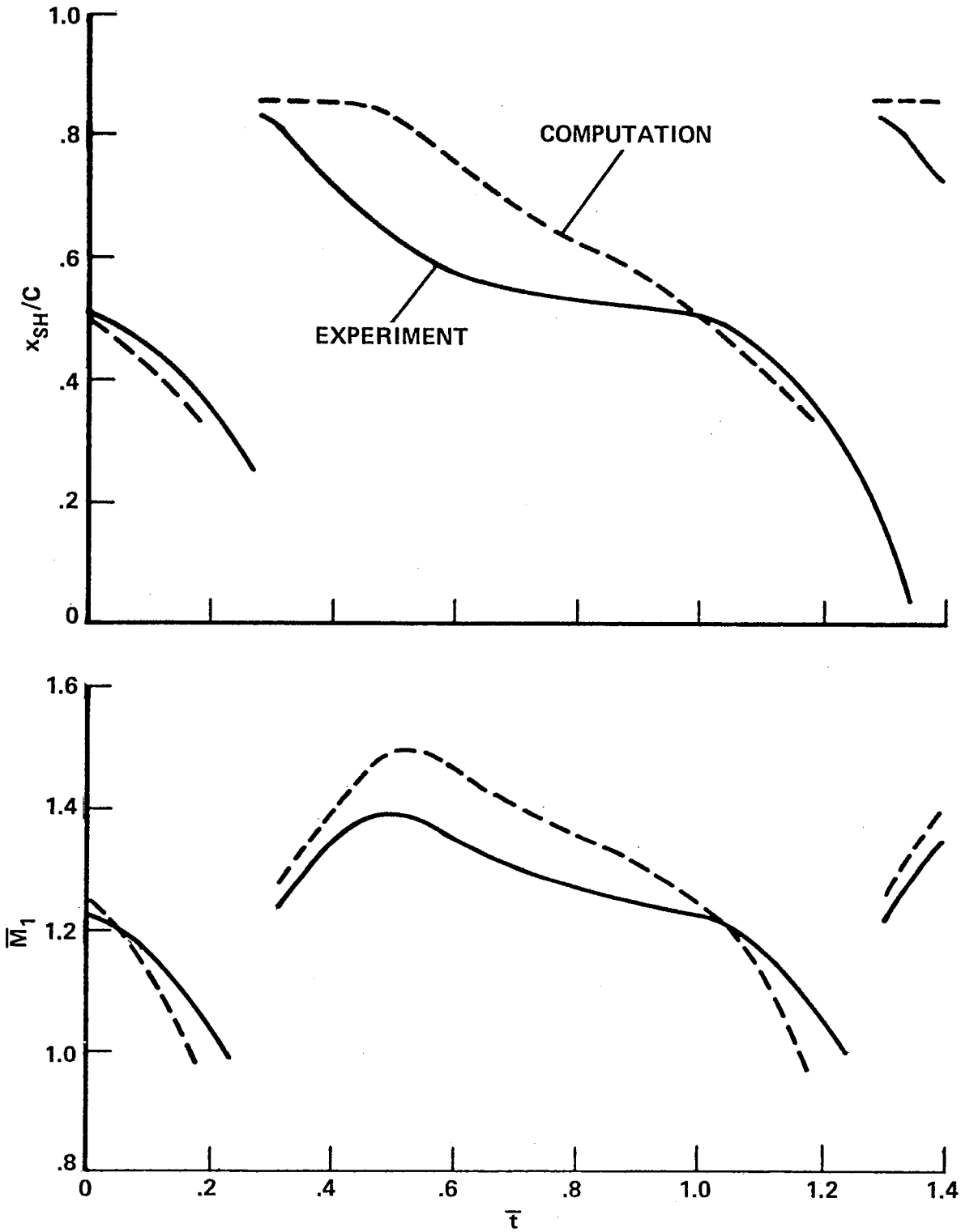

Figure 50.- Comparisons of computed and measured shock position and Mach number at the shear layer edge for unsteady flow; $M_\infty = 0.76$, $Re_{c,\infty} = 11 \times 10^6$.

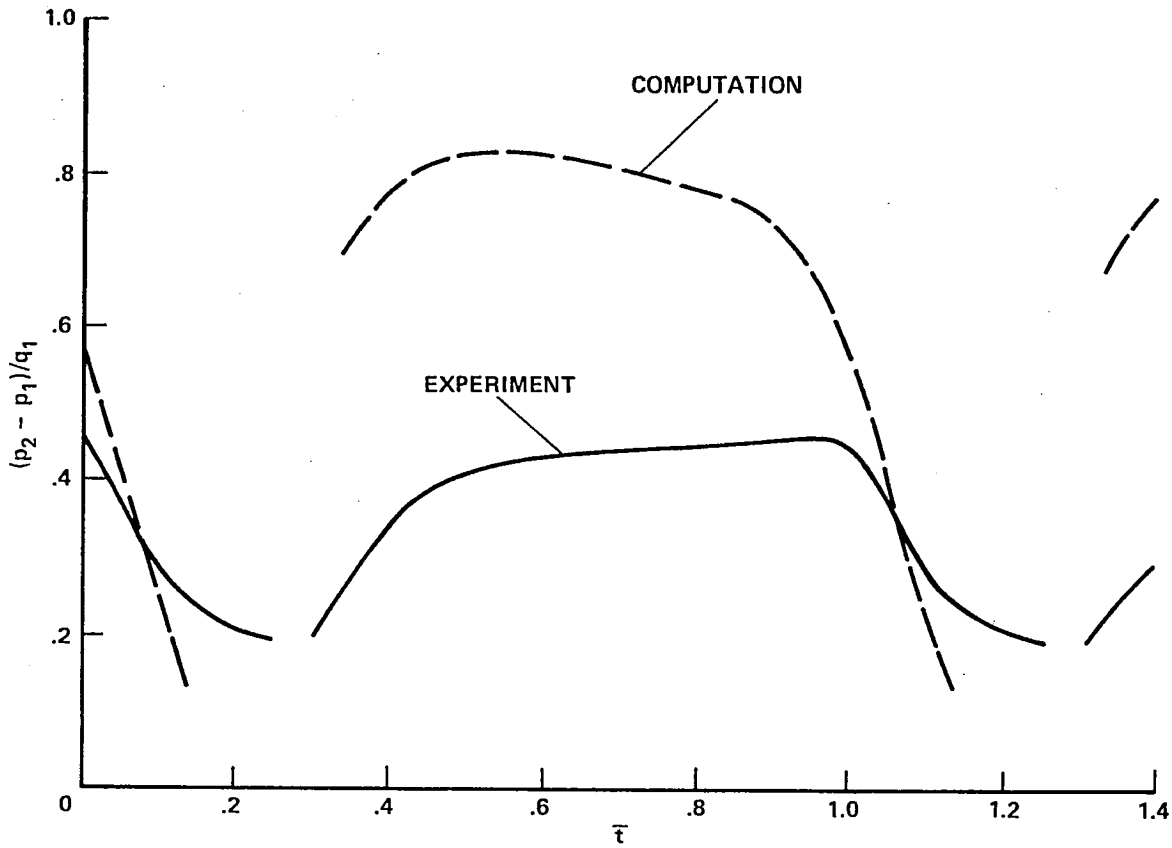

Figure 51.- Comparison of computed and measured shock-wave pressure jump at the shear layer edge for unsteady flow; $M_\infty = 0.76$, $Re_{c,\infty} = 11 \times 10^6$.

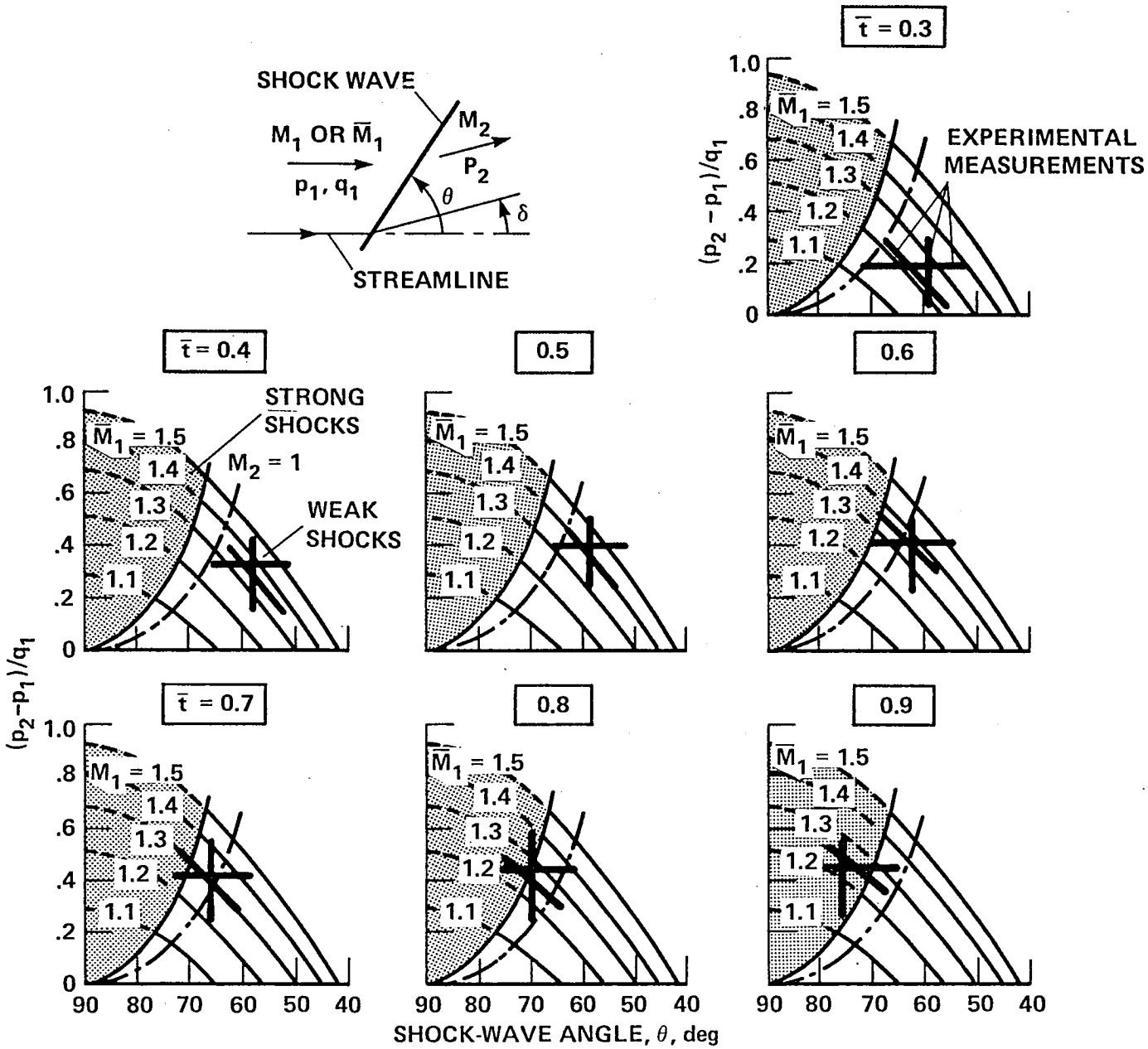

Figure 52.- Oblique shock relationships with overlay of experimental measurements at the shear-layer edge in unsteady flow; $M_\infty = 0.76$, $Re_{c,\infty} = 11 \times 10^6$.

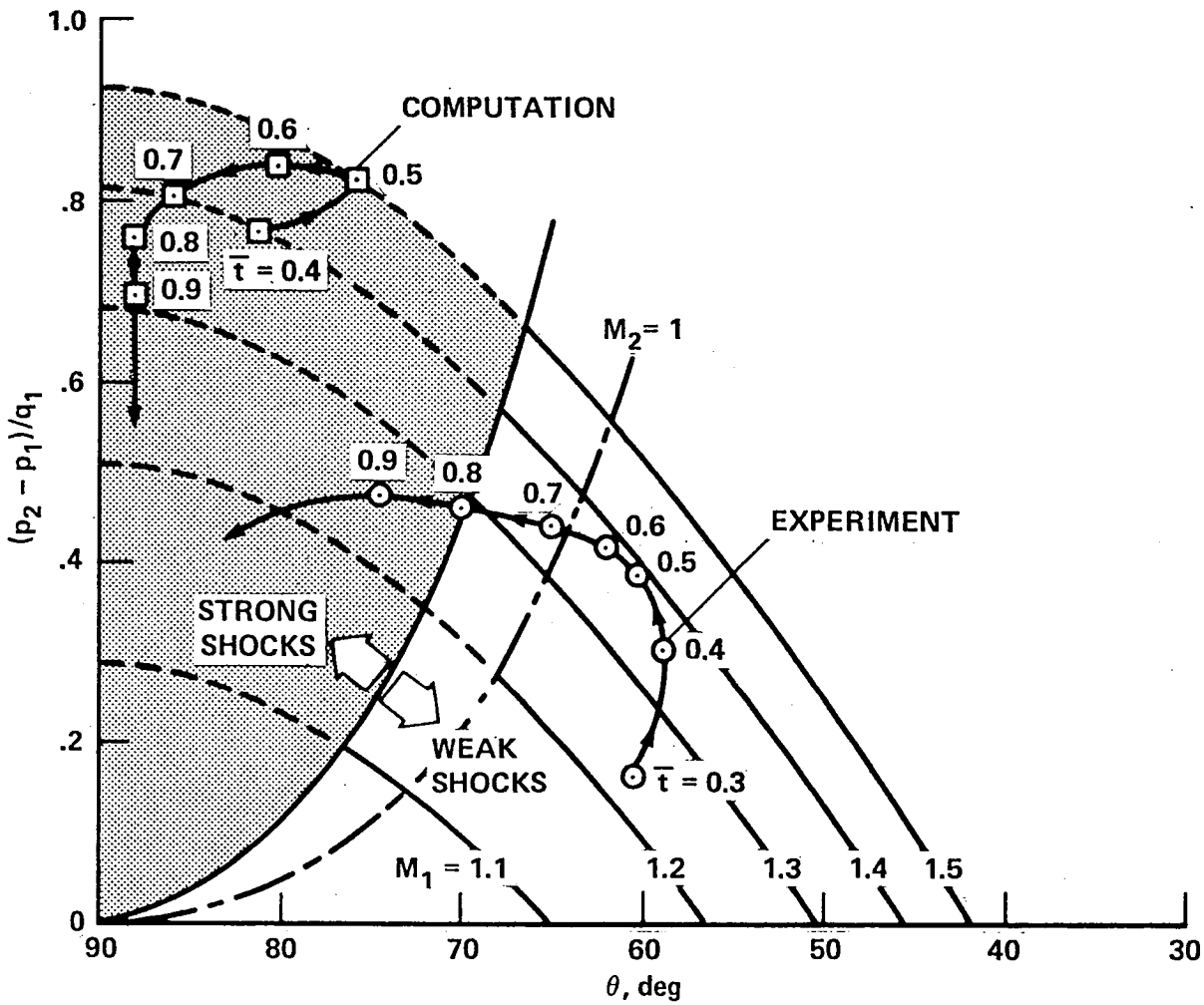

Figure 53.- Oblique shock relationships and comparison of computed and experimental measurements at the shear-layer edge in unsteady flow; $M_\infty = 0.76$, $Re_{c,\infty} = 11 \times 10^6$.

1. Report No.	2. Government Accession No.	3. Recipient's Catalog No.
NASA TM-78549		

4. Title and Subtitle	5. Report Date
SUPERCRITICAL FLOW ABOUT A THICK CIRCULAR-ARC AIRFOIL	6. Performing Organization Code

7. Author(s)	8. Performing Organization Report No.
John B. McDevitt	A-7693

9. Performing Organization Name and Address	10. Work Unit No.
NASA Ames Research Center Moffett Field, Calif. 94035	505-06-11
	11. Contract or Grant No.

12. Sponsoring Agency Name and Address	13. Type of Report and Period Covered
National Aeronautics and Space Administration Washington, D.C. 20546	Technical Memorandum
	14. Sponsoring Agency Code

15. Supplementary Notes

16. Abstract

The supercritical flow about a biconvex circular-arc airfoil is being thoroughly documented at Ames Research Center in order to provide experimental test cases suitable for guiding and evaluating current and future computer codes. This paper is a continuation of an earlier study and extends the original test program to include effects of angle of attack, effects of leading and trailing-edge splitter plates, additional unsteady pressure fluctuation (buffeting) measurements and flow-field shadowgraphs, and application of an oil-film technique to display separated-wake streamlines. Detailed comparisons of computed and measured pressure distributions for steady and unsteady flows, using a recent computer code representative of current methodology, are included. It was found that the numerical solutions are often fundamentally incorrect in that only "strong" (shock-polar terminology) shocks are captured, whereas experimentally, both strong and weak shock waves appear.

17. Key Words (Suggested by Author(s))		18. Distribution Statement
Fluid mechanics	Supercritical flow	Unlimited
Numerical methods	Separated flow	
Airfoils	Unsteady flow	STAR Category - 02

19. Security Classif. (of this report)	20. Security Classif. (of this page)	21. No. of Pages	22. Price*
Unclassified	Unclassified	83	$5.00

*For sale by the National Technical Information Service, Springfield, Virginia 22161